Microfabrication of Silicon Tips for Scanning Probe Microscopy

by

Mi Yeon Song

A thesis submitted to

The University of Birmingham

for the degree of

DOCTOR OF PHILOSOPHY

Nanoscale Physics Research Laboratory

School of Physics & Astronomy

The University of Birmingham

June 2009

Abstract

This thesis investigates the microfabrication of silicon tips for Scanning Probe Microscopy (SPM). One of the potential benefits of microfabricated silicon tips over those formed by traditional methods, such as electrochemical etching, is that the microfabricated silicon tip dimensions can be finely controlled during tip creation; multilayered structures can be fabricated. Here, three different types of silicon tip are fabricated and the use of these tips is successfully demonstrated in Scanning Tunnelling Microscopy (STM) and Scanning Probe Energy Loss Spectroscopy (SPELS).

First, a microfabrication process was developed to produce silicon tips over 100 μm height with a sharp apex of ~10–20 nm. To prevent inadvertent contact between the substrate bearing the tip and the sample being probed, the tip is elevated on a mesa structure. The fabrication of the sidewalls angle of the mesa structure was also investigated to allow additional metallization. The performance of the silicon tips was evaluated in STM and atomic resolution STM images of graphite are successfully obtained.

Subsequently, an Au cathode co-axial silicon tip was developed for SPELS. SPELS uses an STM tip in field emission mode and then analyses the energy of electrons backscattered from the substrate. However, the electric field applied between tip and substrate to facilitate field emission distorts the trajectories of the backscattered electrons. To reduce this effect, a screened microfabricated Au cathode co-axial silicon tip was designed; the tip consists of a multilayer Si/Au/HfO_2/Au structure. The outermost Au layer is grounded during operation and shields backscattered electrons from the electric field applied between tip and surface. The inner Au layer is exposed to a vacuum. SPELS spectra of graphite taken using these Au cathode co-axial silicon tips were successfully obtained for the first time and the potential to develop angular resolved SPELS was demonstrated.

Third, a multilayered silicon tip was fabricated for local photoemission measurement with the Scanning Probe Electron AnalyseR (SPEAR). This approach is a combination of STM with an ultraviolet light source and it can in principle obtain chemical information as well as topographic information from surfaces, like SPELS. The designed structure is a multilayered silicon tip consisting of Si/SiO_2/Au/SiO_2/Au; the three conducting layers act as an electron collector, retarding field analyser, and grounded shield layer, respectively.

Acknowledgments

I would like to thank my supervisor Prof. Richard E. Palmer for giving me a big challenging project. His constant guidance, his bottomless well of knowledge, his patience makes me to complete my project. I especially appreciate to him for all correspondence about my queries at all hours and I've learned a lot from him. I also thank my co-supervisor Dr. Alex P.G. Robinson for supporting me all his efforts to carry on this project. I learn a lot of techniques in a clean room. I enjoy discussing any issues of project and others with him.

I thank to James Lawton for helping and discussing all work in G12. I may not finish my work without his help. He spent plenty of time to support SPELS and I appreciate his all assistance. I also would like to thank Jinlong and Adriano for all discussion while I am working in G12.

I thank all our cleanroom members, Francis, Jed, Hasnah, Andrease. It is not easy to work by myself all day in a cleanroom and they make me help physically and mentally. I also thank Dr. Jason and Dr. Carl in the school of mechanical engineering.

I would like to thank all members of NPRL for their supporting and friendship since I came to UK. I especially thank my unique female friends, Emma and Nathalie and I am very glad to spend time with them during my PhD.

I would like to thank my family and I cannot finish my PhD without their supporting. I dedicate this thesis to my parents.

Contents

Acronyms

AES	Auger Electron Spectroscopy
AFM	Atomic Force Microscopy
CAD	Computer Aided Design
CHA	Concentric Hemispherical Analyser
CNT	Carbon Nanotube
DRIE	Deep Reactive Ion Etching
EBL	Electron Beam Lithography
ECR	Electron Cyclotron Resonance
EDX	Energy Dispersive X-ray
EELS	Electron Energy Loss Spectroscopy
FED	Field Emission Display
FWHM	Full Width at Half Maximum
FE-STM	Field Emission Scanning Tunnelling Microscopy
LEED	Low Energy Electron Diffraction
MEMS	Micro-Electro-Mechanical Systems
PES	Photo Electron Spectroscopy
RF	Radio Frequency
RIE	Reactive Ion Etching
RFA	Retarding Field Analyser
SEE	Secondary Electron Emission
SEM	Scanning Electron Microscopy
SNOM	Scanning Near Field Optical Microscopy
SPEAR	Scanning Probe Electron AnalyseR
SPELS	Scanning Probe Energy Loss Spectroscopy
SPM	Scanning Probe Microscopy
STM	Scanning Tunnelling Microscopy
UHV	Ultra High Vacuum
UPS	Ultraviolet Photoelectron Spectroscopy
UV	Ultra Violet
TSP	Titanium Sublimation Pump

Chapter One

Introduction

In the twenty-first century, nanotechnology is developing quickly and scientists have already developed nano applications in fields such as battery-storage capacity [1]*, computer-chip miniaturization* [2]*, drug delivery* [3]*, and energy* [4]*. Nanotechnology deals with objects which have extremely small dimensions; one nanometre is a millionth of a millimetre and about one eighty thousandth of the width of a human hair. At this small scale the physics of our everyday world, gives way to the physics of the small- quantum mechanics. It is the exotic properties produced by quantum mechanics that nanotechnology and nanoscience try to tame and understand. Thus it is highly desirable to develop new scientific instruments able to observe and characterize this nano world.*

In the early 1980s, G. Binnig and H. Rohrer invented Scanning Tunnelling Microscopy (STM). They demonstrated that it is possible to characterize a surface in real-space with atomic-scale spatial resolution [5,6]. The invention of STM has accelerated our understanding of surfaces at an atomic scale and STM has proved to be a powerful instrument in many scientific areas including surface science, materials science, surface chemistry, electrochemistry, and biology [7,8]. The STM measures the tunnelling current between a sharp tip and a surface as the tip is scanned over the surface and it gives topographic information with an atomic resolution. STM has been also used to manipulate atoms on a surface; for instance Eigler *et al.* successfully demonstrated the positioning of 35 individual xenon atoms to write IBM on a nickel surface [9]. However, the Achilles' heel of STM is its lack of chemical sensitivity. An STM image shows the spatial locations of surface atoms, but does not tell us, except in a select few cases, what element the atoms are.

It is, therefore, desirable to invent new instruments that can combine the spatial resolution of STM with the chemical sensitivity of other surface science spectroscopy techniques. Electron Energy Loss Spectroscopy (EELS) has excellent spectroscopic capabilities and is widely used to investigate the excitation spectra and chemical composition of surfaces. EELS usually observes energy losses in a reflected electron beam related to the excitation of surface plasmons and interband transitions. However, EELS generally has poor spatial resolution. Therefore, a technique that combines the spatial resolution of STM with the electronic spectroscopy of EELS would be a useful tool for surface analysis.

The Nanoscale Physics Research Laboratory has developed this type of SPM instrument, which we call Scanning Probe Energy Loss Spectroscopy (SPELS). SPELS is a hybrid instrument which combines an STM with an electron energy analyser to

obtain a topographic image as well as localised electron energy loss spectroscopy measurements. SPELS uses an STM tip in field emission mode as a local electron source and the field emitted electrons from the tip are elastically and inelastically scattered from a surface. The backscattered electrons are collected by a hemispherical analyser so that the spectral information can be obtained. SPELS has successfully obtained energy loss spectra from different surfaces, for example graphite, silicon, gold, and silver [10-14] and the local secondary-electron emission spectrum from graphite has also been studied [15]. However, the negative bias applied to the tip to generate the field emission current distorts the trajectories of the backscattered electrons so that electrons are suppressed back into the surface. Additionally the applied field can also eliminate the angular properties of backscattered electrons in SPELS. The main aim of the work in this thesis is to develop new types of tips for SPELS to solve these problems.

As a starting point, co-axial structures based on chemically etched tungsten tips were made using a number of methods, for example a glass coated tungsten tip and tungsten tip with a shield painted on by hand. If the co-axial structure tip has an outer grounded layer, the electric field should be macroscopically attenuated and therefore greatly less affect the electron trajectories. However, none of them were very successful in shielding the electric field. Starting it forward route to fabricate a fine and well-controlled co-axial structure based on a tungsten tip so a new type of co-axial tip was developed. We used well developed microfabrication techniques, which are widely used in the semiconductor industry, to build finely controlled microfabricated co-axial silicon tips. These microfabricated silicon tips consisted of an inner gold (Au) coated silicon tip acting as a STM probe as well as the electron source. This was coated in an insulating hafnium dioxide (HfO_2) layer and a conducting Au outer layer to form the grounded

shield. Having prepared such a multilayer structure the outer metal layer and the oxide layer were etched away at the near apex of the tip.

Building on these microfabrication techniques opens up new possibilities for combination STM with surface science spectroscopic techniques. In this thesis I use these microfabrication techniques to build and design a prototype tip for another new scanning probe analyser that combines STM with Ultraviolet (UV) Photoelectron Spectroscopy (UPS), which we call the Scanning Probe Electron AnalyseR (SPEAR). SPEAR can detect excited electrons which are generated by UV light, giving spatially resolved chemical information. A SPEAR tip is essentially a miniature retarding field analyser. It has an electron collector, a retarding field analyser, and a grounded layer. These three conducting layers are separated by insulator, and thus there are five layers in total for the SPEAR tip as opposed to three for a SPELS tip. In this thesis, the silicon tip structures were designed and developed using microfabrication techniques and the microfabricated silicon tips as SPM probes was investigated.

The organization of this thesis is as follows: Chapter Two introduces applications of silicon tips and the operational concepts of SPELS are described together with related techniques. The concept of SPEAR is also briefly introduced. Chapter Three reviews microfabrication techniques including electron beam lithography, dry etching, and thin film deposition, which are required techniques to fabricate the tips, and describes the preparation of samples for analysis and operation of the Ultra High Vacuum (UHV) SPELS system. The experimental results are divided into two parts: microfabrication of silicon tips for SPM is described in Chapter Four and the application of the tips is described in Chapter Five. In Chapter Four, the design and fabrication of three different tip structures, for STM, SPELS, and SPEAR respectively is described. In Chapter Five, microfabricated silicon tips were used to obtain a atomic

resolution STM image of graphite and STM images of nano clusters on a graphite surface. An Au cathode co-axial silicon tip was used to measure the SPELS spectra of graphite-the first time this has been achieve with a co-axial tip. The co-axial tip SPELS spectra of graphite are compared with spectra of graphite taken with a normal tungsten tip. Finally, in Chapter Six the conclusions of this work are drawn and future work for the improvement of microfabricated silicon tips as well as the SPELS instrument are suggested.

Chapter Two

Background

In this chapter, microfabrication of silicon tips and scanning probe microscopy, the two main sets of techniques involved in this work, are both reviewed. First, applications of silicon tips are presented, especially field emitter silicon tips. The second part of the Chapter discusses scanning probe microscopy techniques, especially scanning probe energy loss spectroscopy (SPELS). To understand SPELS, the techniques of STM and EELS are introduced. A status report on a home-grown SPELS instrument and some related developments are also presented. The third part of the Chapter introduces briefly scanning probe electron analyser (SPEAR).

2.1 Microfabrication of Silicon Tips

Microfabrication processes are widely used in the semiconductor industry to make small devices from micrometer to nanometre size. Microfabricated devices are most of them usually formed on silicon substrates. In this study, microfabricated silicon tips are used as a field emitter and electron beam lithography, dry etching, thin film metal deposition, and thermal oxidation techniques are mainly used to produce silicon tips.

2.1.1 Applications of Silicon Tips

Microfabricated silicon tips have many applications. The dimensions of a microfabricated silicon tip can be carefully controlled and it is also possible to fabricate tips in batches, precisely control the tip radius and height of the tip, modify the tip surfaces, and produce various structures such as vertical and horizontal wedge emitters.

The silicon tip is most widely used as an atomic force microscopy (AFM) probe. AFM probes consist of a tip on a flexible cantilever, typically fabricated from a single substrate. Such silicon tips are widely available commercial, and can incorporate special features such as additional coating layers for making measurements of things as diverse as conductivity to chemical bond strength [16].

Microfabricated silicon tips have been applied as SPM probes in STM [17], scanning near field microwave microscopy [18,19], and scanning near field optical microscopy (SNOM) [20-22]. For example, Bale *et al.* suggested multiprobe scanning tunnelling microscopy [17]. In this scheme, three microfabricated silicon tips in an array, and with independent electrical connection, could be used to make STM measurements of several areas of a sample simultaneously.

Whilst etched or cut metal tips are most widely used as the probe in STM, microfabricated silicon has the advantage that much better control of the tip geometry

can be achieved. Silicon tips have been developed with the various structures for SPM. For instance a SNOM silicon tip with a co-axial structure which consists of two components, a sharp apex as an AFM probe and a circular metallic aperture around the tip has been fabricated, as shown in Figure 2.1 [22]. The aim of this work is the integration of a SNOM with an AFM cantilever and the co-axial structure of the silicon tip has shown to improve transmission efficiency when compared with optical fibres.

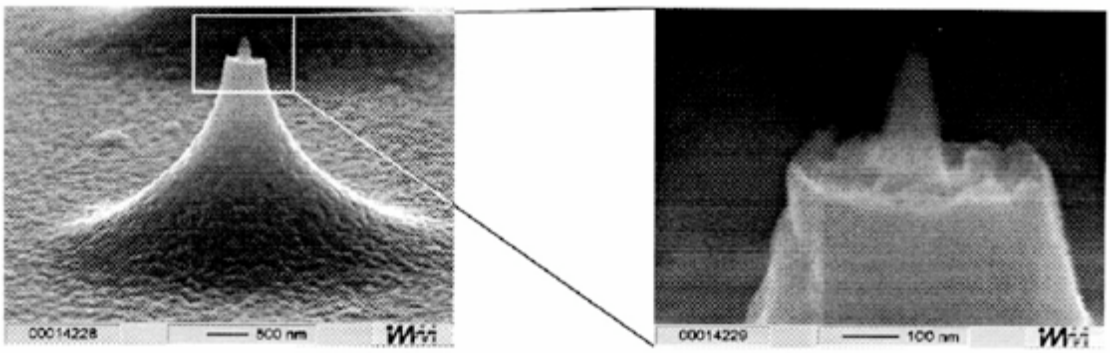

Figure 2.1: Microfabricated co-axial silicon tip for SNOM. The aperture is formed by aluminium coating and the tip is coated with Si_3N_4. From [22]

Well-defined silicon tip arrays over a large area have been suggested for micro fluidics and tissue engineering due to the property of modifying surface wetting characteristics [23]. Silicon tips have been also developed for various other applications, such as drug delivery [24], miniature electron beam columns [25], and vacuum-sealed magnetic sensors [26].

2.1.2 Field Emitted Silicon Tips

In this study, microfabricated silicon tips are mainly used as a field emitter. Recent application of silicon tips is in field emission displays (FED). FED uses an array of field emitting tips, as shown in Figure 2.2 [27]. It has three layered structure, for example a

silicon tip or a metal coated silicon tip, an insulating layer and a gate (or grounded) layer (Figure 2.2(a)). Tips are used as electron sources to energise a phosphor-coating layer and cause light emission. However, these types of three layered tips can be used as field emitters but cannot be applied as an STM probe. In our experiment, we produce silicon tips integrated with insulating layer and grounded layer.

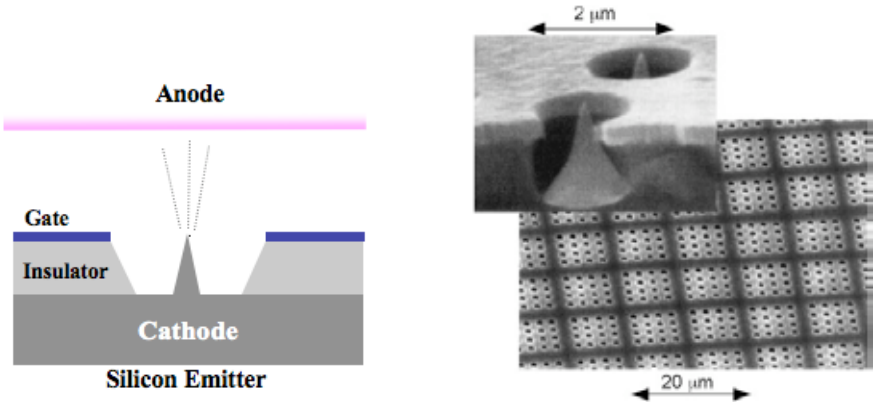

(a) (b)

Figure 2.2: (a) Schematic diagram and (b) array of field emitting silicon tips and inset a single tip. From [27]

The field emission silicon tips needs a high field emission current at low bias to apply for field emitters. Field emission currents are usually determined by surface properties of the emitting material. For example, silicon surface is easily oxidized even though UHV environments. Silicon dioxide layer can cause an unstable field emission current. To improve the field emission properties, the emitter materials must have a low work function, a high melting point and chemical inertness. A surface coating on the silicon tips is one of solutions to improve field emission properties. For example, diamond [28,29], diamond-like carbon [30], boron nitride [31], and metals [32, 33] have all been need to improve silicon field emitters. In our case, we choose the Au as an emitting layer. Au layer is easy to produce onto the silicon tips and Au is also very inert

material. Many groups have reported on the field emission properties of Au field emission layers. Ishikawa *et al.* evaluated various emitters, for example, Cu, Ag, Au, Al, Ge, Cr, Mo Ni, Pt and the Au showed excellent stability among those metals [34]. Au nanowires are also studied for their field emission properties [35, 36].

2.2 Scanning Tunnelling Microscopy (STM)

Scanning tunnelling microscopy (STM) allows the investigation of a surface down to the atomic scale and it is a powerful instrument for surface characterization. The first tunnelling instrument, known as a "topografiner", was developed in 1972 by Young *et al.* [37, 38]. The tunnelling instrument consists of a metallic tip, piezoelectric scanner, and feedback loop. The topografiner obtained surface microtopography images by scanning the tip over a surface and measuring the electron tunnelling between the two. The current-voltage dependence of the tip versus distance between tip and surface in a metal-vacuum-metal tunnel junctions in exponential allowing the distance to be determined with great accuracy.

The topografiner was not capable of atomic resolution but was shortly followed by the development of the STM by Binnig and Rohrer in 1982, for which they were awarded the Nobel Prize in 1986 [5,6]. The importance of this technique was proved when the silicon (111)-(7×7) reconstruction was imaged in a real space for the first time [40]. This exciting work was used to decide between the various proposed models of the silicon surface. In 1990, Eigler *et al.* manipulated atoms using a low temperature (4K) STM. He moved xenon atoms on a nickel surface using an STM tip and spelled out IBM's initials with 35 individual xenon atoms [9]. This was the first example of atomic manipulation in STM and is shown in Figure 2.3.

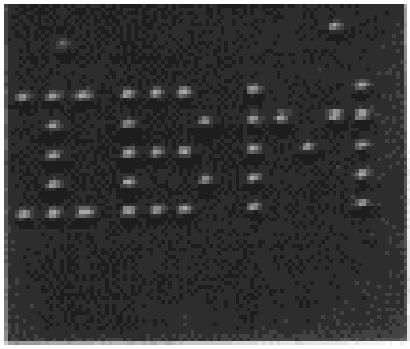

Figure 2.3: IBM's initials spelled using Xe atoms; STM image. From [9]

A typical STM consists of a very sharp metal tip, a piezoelectric scanning unit used to control the vertical and lateral movement of the tip, a coarse positioning unit which brings the tip-sample separation to within the tunnelling range, a vibration isolation stage, and a set of electronics for detecting small tunnelling currents, controlling the piezo-tube scanner via a feedback system and driving the "coarse" positioning. The basic principle of STM is shown in Figure 2.4.

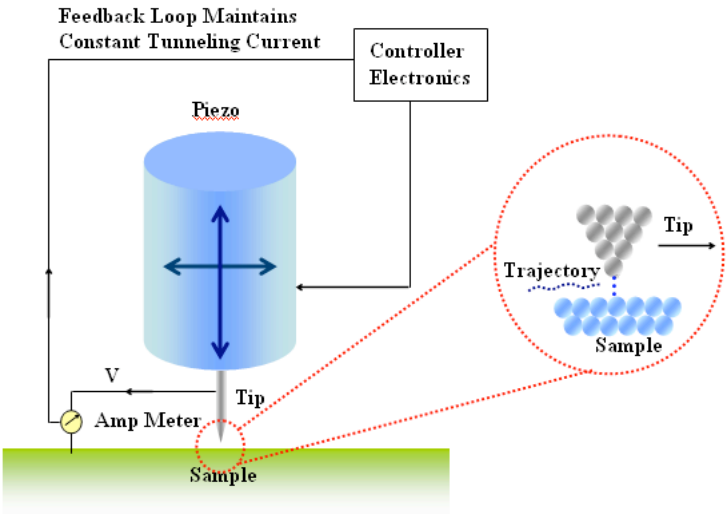

Figure 2.4: Basic principle of STM. The STM tip scans the conducting sample measuring a tunnelling current.

The tip is mechanically connected to the scanner, an XYZ positioning device, which is made of piezoelectric materials. Piezoelectric materials expand when an electric field is applied and are usually made of ceramics such as lead oxide, zirconate oxide, titanium oxide, and so forth. The tip is then scanned over the conducting substrate. The tip can be controlled with atomic scale resolution by applying a voltage to the piezotube. The STM system has to be mounted on an isolated stage to avoid noise and vibration.

STM has two different modes: constant current mode and constant height mode, as shown in Figure 2.5.

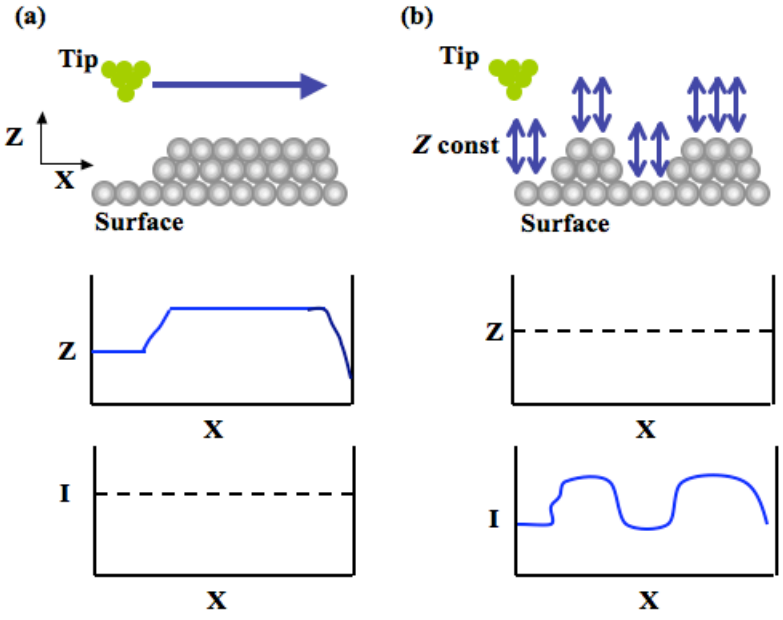

Figure 2.5: Modes of operation of the STM: (a) constant current mode; (b) constant height mode. After [39]

Constant current mode is the more common method in STM and is shown in Figure 2.5(a). The feedback circuit measures the tunnelling current *I* and adjusts the *Z* position by applying a bias voltage to the piezotube in order to maintain constant current. The STM tip is scanned in the X direction and the electron tunnelling current is collected as a function of the X and Y position, with a constant current *I* over the surface. The output

is an image of the Z position of the tip plotted against X and Y. Constant height mode, is shown in Figure 2.5(b). The tip is scanned over the surface with a constant height *Z* relative to the surface. The tip is moved up and down in the *Z* direction while the tunnelling current is measured.

When a sharp tip is brought close (a few Å) to a conductive surface, the wave functions of the electrons from the tip and the surface overlap. By applying a voltage between the tip and the surface, a tunnelling current is established through the vacuum barrier. This phenomenon is known as "electron tunnelling", which is the basic principle on which STM was designed.

In vacuum tunnelling, the vacuum acts as a potential barrier that the electrons in the tip and surface cannot overcome. Classically electrons cannot pass across this barrier if their energy is less than the barrier height. A schematic diagram of this barrier is shown in Figure 2.6.

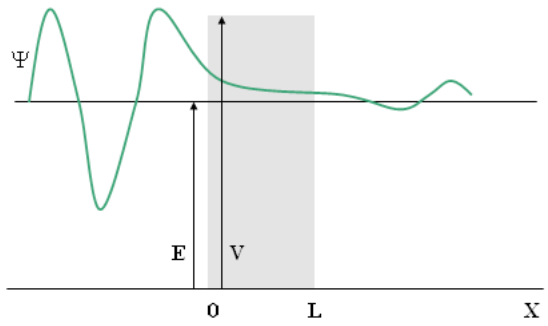

Figure 2.6: One-dimensional tunnelling diagram. An electron has a probability of tunnelling through a barrier.

However, quantum mechanics allows electrons to pass through a classically forbidden barrier if the distance between tip and surface is small. This is known as "tunnelling". The quantum mechanical description of electron tunnelling in one dimension can be

derived by application of the time independent Schrödinger equation. The Schrödinger equation can be written as [40],

$$-\frac{\hbar^2}{2m}\frac{d^2\Psi}{dx^2} = (E-V)\Psi \tag{2.1}$$

The Schrödinger equation can be used to calculate the probability of tunnelling for an electron of mass *m* incident upon the potential barrier (x < 0, V = 0) [40].

$$\Psi = Ae^{ikx} + Be^{-ikx},\ k\hbar = \sqrt{2mE} \tag{2.2}$$

Considering the Schrödinger equation for the vacuum region representing the barrier $0 \le x \le L$, with E < V, the general solution is given by [40],

$$\Psi = Ce^{kx} + De^{-kx},\ k\hbar = \sqrt{2m(V-E)} \tag{2.3}$$

On the right side of the barrier (x > L), with V = 0, the wave functions are [40]

$$\Psi = A'e^{ikx} + B'e^{-ikx},\ k\hbar = \sqrt{2mE} \tag{2.4}$$

The electron's wave functions have to be continuous at the edges of the barrier (x = 0 and x = L). This gives

$$\text{A} + \text{B} = \text{C} + \text{D},\ Ce^{kL} + De^{-kL} = A'e^{ikL} + B'e^{-ikL} \tag{2.5}$$

The first derivatives ($d\Psi / dx$) must also be continuous

$$ikA - ikB = kC - kD\,,\ kCe^{kL} - kDe^{-kL} = ikA'e^{ikL} - ikB'e^{-ikL} \tag{2.6}$$

If the electrons are incident on the barrier from the left (x < L), there can be no electrons travelling to the left on the right of the barrier (x > L). Therefore, it can be assumed that B′ = 0.

In the x < 0 region, the probability that the electron is travelling in the position x direction is proportional to $|A|^2$. In the x > L region, the probability that the electron is again travelling in the positive x direction is proportional to $|A'|^2$. Thus, the transmission probability can be represented by $T = \frac{|A'|^2}{|A|^2}$ [40].

$$T = \left\{1 + \frac{(e^{kL} - e^{-kL})^2}{16\frac{E}{V}(1 - \frac{E}{V})}\right\}^{-1} \tag{2.7}$$

This can be simplified to

$$T \approx 16\frac{E}{V}(1 - \frac{E}{V})e^{-2kL} \tag{2.8}$$

The tunnelling probability decreases exponentially with the thickness of the barrier (L). For example, if the distance between tip and sample is changed by 1Å, the tunnelling current will increase by nearly an order of magnitude. Therefore, STM allows very

accurate measurement of the separation, but also requires very precise control of the position of the tip, and vibration of the STM stage should be minimized.

Figure 2.7 illustrates an energy level diagram of the sample-vacuum-tip. The tunnelling between sample and tip occurs from occupied states below the Fermi level, E_F, to unoccupied states above E_F. The occupied and unoccupied distributions of states are displaced by eV_T, where V_T is the tunnelling voltage. For example, if the sample has a positive voltage, the electrons will tunnel from occupied states in the tip to an empty state in the sample. If the sample has a negative voltage, the electrons tunnel from the occupied states in the sample to empty states of the tip.

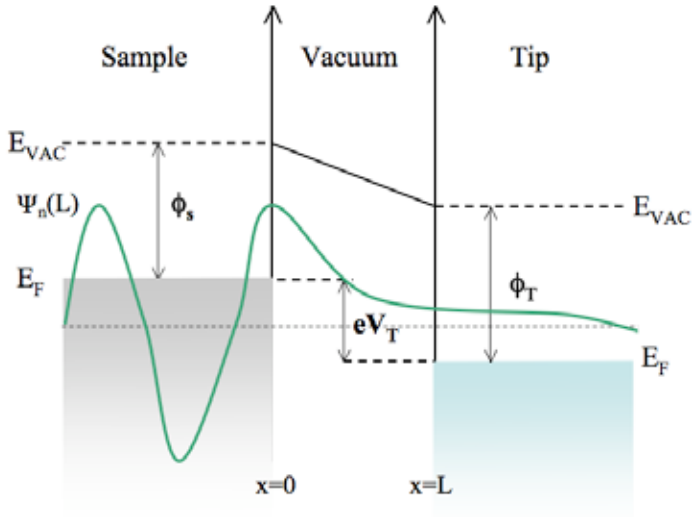

Figure 2.7: Energy level diagram of a tunnel barrier between sample and tip in an STM with work function ϕ and tunnel voltage V_T.

2.3 Electron Energy Loss Spectroscopy (EELS)

Electron energy loss spectroscopy (EELS) is together with STM for major element of SPELS. The EELS instrument consists of an electron source, a monochromator, analyser, and Channeltron. The electrons are tuned in the monochromator so the

incident beams are well defined in the EELS system. A schematic diagram of the EELS apparatus is shown in Figure 2.9 [41]. Electrons are incident on the sample at an angle defined by the monochromator rotation. The monochromator can rotate from 0^o to 90^o with a fixed analyser or the angular can rotate which the monochromator remains fixed. The electrons reflected from surface are then collected by the analyser which is effectively a variable energy filter. Electrons with the appropriate energy can travel through the analyser to be detected by the Channeltron. By varying the energy that the analyser with pass or spectrum of energy loss can be measured. The angularly resolved measurement can provide k-space information.

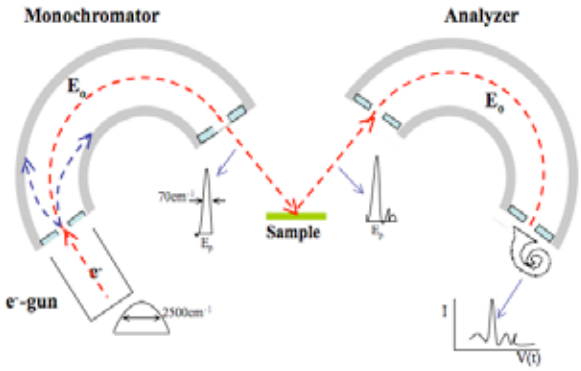

Figure 2.9: Schematic diagram of an EELS instrument. An electron beam is formed by the electron gun and incident to the sample. The scattered electrons are detected by an analyser. The broken line represents a typical electron trajectory. After [41]

EELS enables measurements of the vibrations of adsorbed species on a surface and of the electronic structures of materials. A monochromatic electron beam is incident on a surface and the energy of the reflected electrons is measured, either as a function of the reflection angle, or at a fixed reflection angle. When the incident electron energy is equal to the reflected electron energy, the electrons have interacted elastically with the sample leading to an energy loss spectrum. When the incident electron interacts with the

surface, the momentum of the reflected electrons can change (loss of energy) due to surface excitations. This energy loss feature can be written

$$\Delta E_{loss} = E_i - E_s \qquad (2.9)$$

where E_i and E_s are the incident and scattered electron energies, respectively. ΔE_{loss} provides information about the surface, for example molecular vibrations or electronic excitations. Figure 2.9 represents the scattering geometry of the electron from a surface excitation in an EELS system [42]. The electron beam with a wave vector k_i is incident on the surface and is scattered with a wave vector k_s. θ_i and θ_s are the angle of the incident and of the scattered electrons respectively, and α indicates the angular acceptance of the detector. The wave vector q_{ll} (in $Å^{-1}$) is the related parallel momentum transferred and is determined from E_{loss}, θ_i, and θ_s.

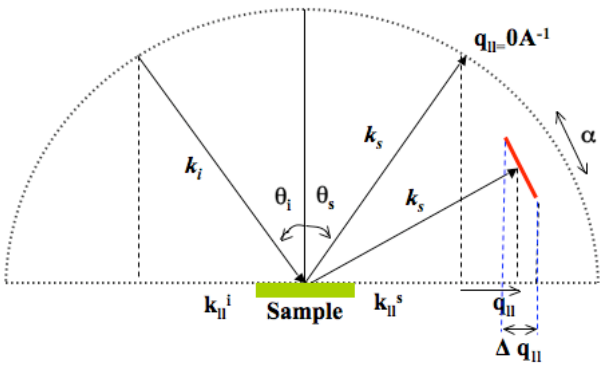

Figure 2.9: Scattering geometry of an electron from a surface excitation. After [42]

Conservation of energy and momentum for incident and scattered electrons can then be used to extract the dispersion of the surface plasmon. There is no conservation of perpendicular momentum. Energy and momentum can be represented as follows,

$$E_i = E_s + E_{loss} \tag{2.10}$$

$$k_{ll}^{\,i} = k_{ll}^{\,s} + q_{ll} \tag{2.11}$$

from Equation (2.11)

$$q_{ll} = k_i \sin\theta_i - k_s \sin\theta_s \tag{2.12}$$

The energy is given by

$$E = \frac{\hbar^2 k^2}{2m},\ k = \frac{\sqrt{2mE}}{\hbar} \tag{2.13}$$

When Equation (2.13) is applied to Equation (2.12), q_{ll} can be then expressed as

$$q_{ll} = \frac{\sqrt{2mE_i}}{\hbar}(\sin\theta_i - \sqrt{1 - E_{loss}/E_i}\,\sin\theta_s) \tag{2.14}$$

E_i, θ_i, and θ_s are known from the experimental parameters and E_{loss} is found from an individual peak in an electron energy loss spectrum. In order to measure the energy loss, a deconvolution of various energy losses is needed, especially at low excitation energy where overlapping of the peaks prevents one from measuring the energy loss directly. The finite angular acceptance of the detector α translates into a finite integration over momentum space (Δq_{ll}), as illustrated in Figure 2.9, and can be written as [42]

$$\Delta q_{ll} = \frac{\sqrt{2mE_i}}{\hbar}(\cos\theta_i + \sqrt{1 - E_{loss}/E_i}\,\cos\theta_s)\alpha \tag{2.15}$$

Electron energy loss spectra were also obtained using SPELS in a similar means to EELS. In the current SPELS system, the primary difference is that the hemispherical analyser is fixed parallel to the sample and perpendicular to the electron beam. However, in SPELS the STM tip is used as the electron source and can approach the surface to within the nm range. It can theoretically provide lateral spatial resolution of 1–10 nm [10], and a resolution of 50 nm has been demonstrated to date [11].

Inelastic Electron Scattering

There are two main inelastic scattering mechanisms for the interaction between the electrons and a metal surface, which are dipole scattering and impact scattering [42].

Dipole scattering is a long-range dipole interaction between the electron's electric field and surface charges. Figure 2.10 illustrates dipole scattering.

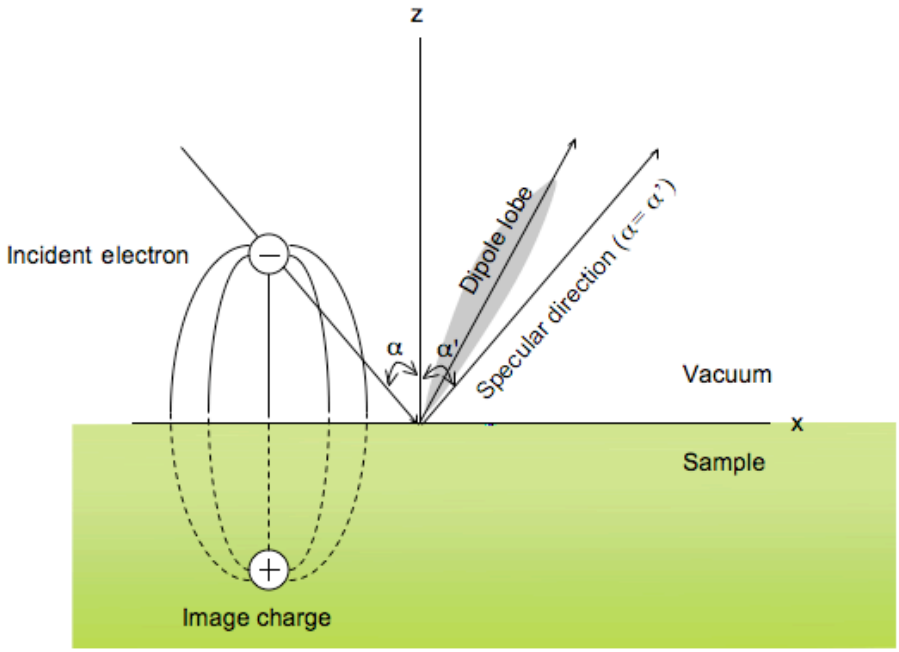

Figure 2.10: Dipole scattering of an incident electron. The incident electron creates the electric field and induces an image charge in the metal surface. Dipole scattering occurs predominantly in forward scattering.

The incident electron creates an electric field perpendicular to the surface and a dipole is formed between the incident electron and its image charge in the surface. The electron is able to scatter inelastically because of its interaction with long-range dipole electric fields arising from the charge fluctuations in vibronic as well as electronic transitions on the surface. The cross section of dipole scattering is strongly peaked in the specular direction which means that the angle of incident electrons equals to the angle of reflected electrons so dipole scattering occurs predominantly in forward scattering. The scattered intensity is thus strongest at angles closer to the specular direction and it is known as the "dipole lobe". However, only those transitions with an electric dipole moment parallel to the electric field lines of the incident electron can contribute to the scattering process. This means that surface excitations in the perpendicular direction can couple with the incident electron. Dipole scattering leads to inelastic processes away from the surface either before or after elastic scattering at the surface [41].

Impact scattering is caused by the short-range interaction between the incident electron, acting as a particle, and the surface. The electrons are scattered on the surface region, occurring at a very small distance and exchanging momentum. Impact scattering is dominant at high impact energies with a broad angular distribution and is the same interaction responsible for the backscattering of electrons in elastic scattering.

Surface Plasmon

In a SPELS spectrum, the primary feature of interest will be peaks associated with interactions of the electron with plasmons, which are propagating the collective oscillation of the electron gas surrounding the atomic lattice ion of a metal. In SPELS, the incident electron energy is in the range of 50~200 eV and the inelastic mean free path of the electrons is less than 5 nm [43]. Therefore, surface plasmons are dominant in

SPELS spectra. The surface plasmon is a collective oscillation of surface electrons in the sample, which decays exponentially perpendicular to the surface and travels parallel to the surface, as shown in Figure 2.11.

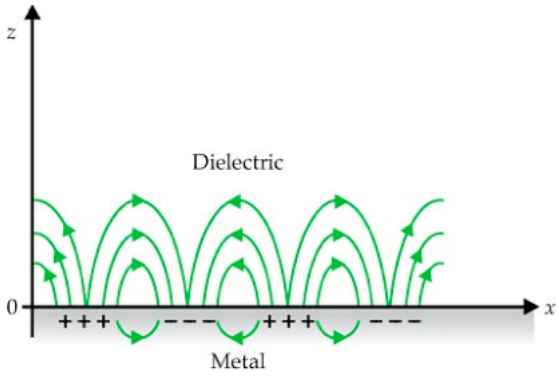

Figure 2.11: Surface charge distribution and electric field lines of a surface plasmon. After [44]

Its electric field is associated with the potential Φ, which can be described by [42]

$$\Phi(x) = \Phi_o e^{iq_{II}x_{II}} e^{-q_{II}|z|} \tag{2.16}$$

where x_{II} is the position vector in the surface plane, q_{II} is the momentum of the surface plasmon parallel to the surface, and z is the distance perpendicular to the surface. The surface plasmon potential is represented by the oscillatory term in the surface plane and it decays exponentially away from the surface. Since the surface plasmon occurs on the surface, the plasma oscillations are very sensitive to any change of the surface, such as the adsorption of molecules to the metal surface.

The condition for existence of the electric field (E_z) can be derived by differentiating Equation (2.16) with respect to the z direction [42]:

$$\text{Above surface: } E_z\,(z = 0^+) = \Phi_o q_{II} e^{iq_{II}x_{II}} \tag{2.17}$$

$$\text{Below surface: } E_z\,(z = 0^-) = -\Phi_o q_{II} e^{iq_{II}x_{II}} \tag{2.18}$$

The E_z is thus discontinuous across the surface. The z component of the electric displacement vector $D_z = \varepsilon(\omega)E_z$ has to be continuous to generate surface plasmons, so Equations (2.26) and (2.27) can be represented by

$$\varepsilon(\omega)\, E_z\,(z = 0^-) = E_z\,(z = 0^+) \tag{2.19}$$

The $\varepsilon(\omega)$ is a dielectric function. When $\varepsilon(\omega)$ is –1, the parallel component of the electric field varies continuously near the surface and can detect the surface plasmon. The dielectric function $\varepsilon(\omega)$ is [42]

$$\varepsilon(\omega) = 1 - \frac{\omega_p^2}{\omega^2} \tag{2.20}$$

where $\omega_p = \sqrt{\frac{ne^2}{m\varepsilon_o}}$, n, e, m and ε_o are the plasma frequency, electron concentration, electron charge, electron mass and the permittivity constant of vacuum respectively. Applying the condition for a surface plasmon, $\varepsilon(\omega) = -1$, to Equation (2.20), the surface plasmon can be represented by

$$\omega_{sp} = \frac{\omega_p}{\sqrt{2}} \tag{2.21}$$

Surface plasmon can be excited by either an electron beam or a light and it can be represented as function of momentum of the surface plasmon which called the surface dispersion curve. The surface dispersion curves of Ag single crystals are shown in Figure 2.12 [45]. Conventionally, the surface plasmon dispersion are obtained using an angle-resolved high resolution EELS (HREELS), in which the normal measurements range lies in higher k (>0.05 q_{II}(Å^{-1}), (Figure 2.12(a)) compared to optical measurements (~ 0.001 q_{II}(Å^{-1}) ,Figure 2.12(c)).

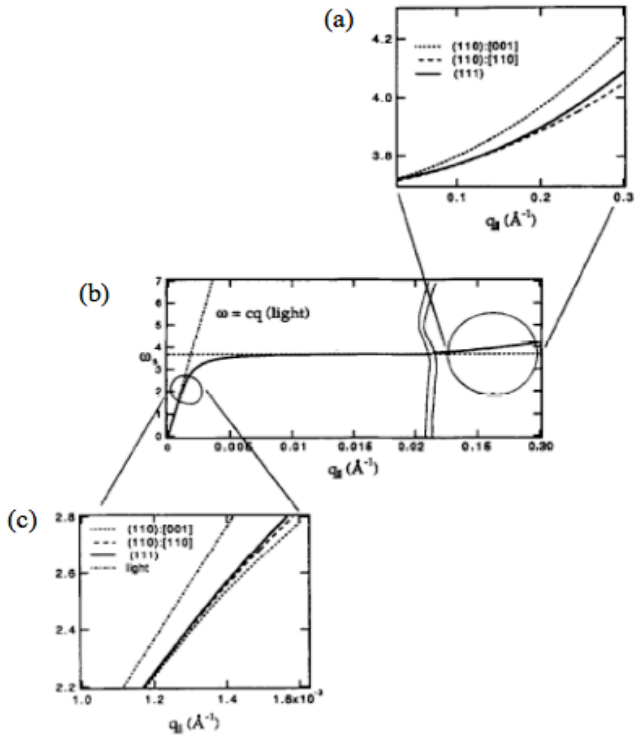

Figure 2.12: Surface plasmon dispersion for Ag single crystal. (a) high q_{II} ($Å^{-1}$) region, (b) overall surface plasmon dispersion curve and (c) high q_{II} ($Å^{-1}$) region. From [45]

In SPELS, an electron beam was employed to excite surface plasmon as in HREELS. However, surface plasmon measurements in SPELS cannot be resolved in k-space because the trajectories of electrons from STM are not collimated (see, Figure 2.17). In other words, the surface plasmon measurements in SPELS take an average value in its energy over a certain k range. Therefore, the surface dispersion curve cannot define in SPELS.

Electron Energy Spectrum

If the surface is bombarded by monochromatic electrons with energy E_p, a typical electron energy spectrum shows different features, as shown schematically in Figure 2.13. The peaks may be resolved depending on the instrument used. The typical features of an energy loss spectrum are represented, for example the secondary electron emission (SEE) peak, Auger peaks, plasmon peaks, and elastic peak.

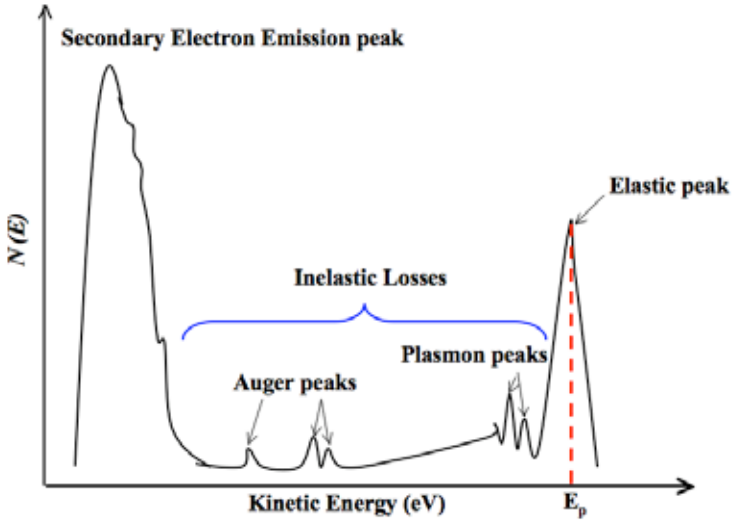

Figure 2.13: Schematic overview of a typical electron energy loss spectrum, showing the different groups of electrons backscattered from the surface.

The SEE peak is shown at low kinetic energies (< 50 eV). The phenomenon of SEE occurs in two steps. First, a internal secondary electron is produced by collisions between the incident electron beam and the solid. Second, a cascade process occurs in the solid generating further secondaries. The cascade results from multiple processes of electron beam interaction in the solid and these electrons diffuse through the solid until they either sink back into the conduction electron band or reach the surface with sufficient energy to emerge as secondary electrons [46]. These electrons generally undergo many scattering events so the energy and angular distribution of the secondary electron cascade retain little information about the initial event. The energy and angular distribution of the secondary electrons are almost independent of the incident electron energy and direction [46]. The cascade features are represented by the broad peak with fine structure shown in Figure 2.13 on the left of the plot. This broad peak is known as a "cascade maximum" [47] and the cascade maximum peak is not considered in this thesis. However, the fine structure of the SEE peak observed is due to the energy structure of the empty state in the solid, which determines SEE into the vacuum [48],

and it provides information about the electronic states of the solid in the k-space regions. For example, the SEE spectrum of graphite has been reported by many groups and found to reflect conduction band states, in agreement with band structure calculations [49, 50].

The Auger peak is a special type of SEE and it gives information on the weak fine structure [47]. The Auger process is a three-electron process. The incident energy excites core electrons above the Fermi level. The inner level is then left unfilled. This hole is filled by an electron from a higher energy level. When the electron falls from a higher energy level to a lower energy level, either the emission of an X-ray photon causes energy loss or alternatively the electron can transfer energy to another electron, which is known as an Auger electron. The Auger peaks represent one of the inelastic energy loss processes. Auger peaks are not discussed in this study.

Plasmon peaks are caused by excitation of interband transitions or by plasma vibration excitation [51]. An interband transition is the excitation of an electron from an occupied surface state to the Fermi level. Some of the electron's kinetic energy can be lost during this process. In EELS and SPELS analysis, the plasmon peak is of particular interest; this region is called the electron energy loss spectrum and plasmon peaks are generally in close proximity to the elastic peak.

The elastic peak has the highest kinetic energy and it represents a sharp peak with strong intensity. It is caused by elastically scattered electrons without any energy loss. The full width at half maximum (FWHM) of the elastic peak is determined by the energy resolution of the instrument. A narrow FWHM indicates higher energy resolution, and depends on the electron beam tuning conditions of an instrument.

In SPELS, the energy losses result from the excitation of surface and bulk plasmons and the generation of an interband transition. These features represent an elastic peak, plasmon peaks, and SEE peaks.

2.4 Field Emission

The properties of field emission are an important factor in SPELS. In order to obtain spectra a field emission current is generated from the STM tip. Field emission arises due to electrons tunnelling through the vacuum barrier at a high electric field, for example 10^7–10^8 V/cm. A schematic energy diagram of a one-dimensional field emission system is shown in Figure 2.14.

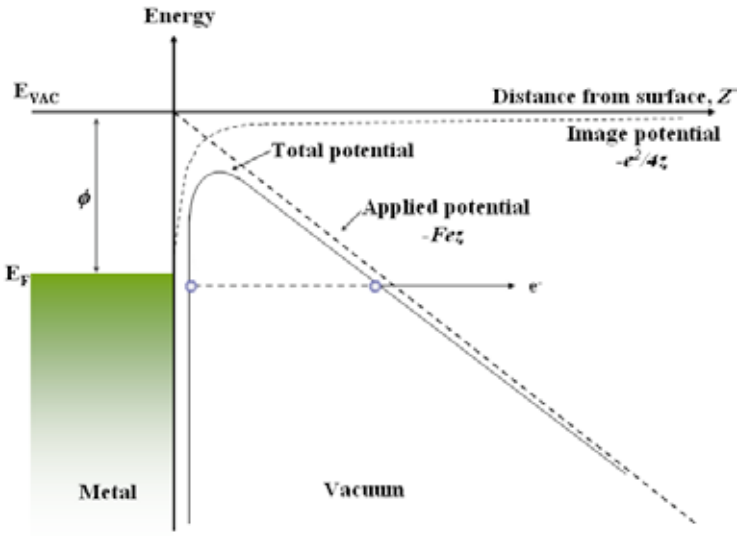

Figure 2.14: Energy diagram for an electron on a metal surface in the presence of an applied electric field *F*. After [51]

where E_F is the Fermi level and ϕ is the work function of the metal. The original barrier, which is an image potential ~ $-e^2/4z$ in this diagram, is deformed by the applied

potential –Fez. The total potential can be represented by combining the image potential and the applied potential. Therefore, the tunnelling barrier is given by

$$V(z) = -\frac{e^2}{4z} - Fez \tag{2.22}$$

The first term is due to the effect of the classical image charge and the second term is the deformation due to the electric field. A lower work function material and a sharper tip reduce the tunnelling barrier and have improved the field emission properties.

The field emission current was first theoretically determined by Fowler and Nordheim in 1928. They expressed the field emission properties of the metal via the Fowler–Nordheim equation [52, 53],

$$\frac{I}{V^2} = a\exp(-b\phi^{3/2}/V) \tag{2.23}$$

where I is the total field emission current and

$$a = 6.2\times10^{-6} A(\mu/\phi)^{1/2}(\mu+\phi)^{-1}(\alpha\kappa r)^{-2} \tag{2.24}$$

$$b = 6.8\times10^{-7}\alpha\kappa r \tag{2.25}$$

Equation (23) takes the natural logarithm on both sides, and then the equation can be written [53, 54]

$$\ln\frac{I}{V^2} = \ln(A6.2\times10^{-6}\frac{(\mu/\phi)^{1/2}}{\alpha^2(\mu+\phi)(kr)^2}) - 6.8\times10^7\frac{\phi^{3/2}\alpha kr}{V} \tag{2.26}$$

where I is the total field emission current in *amps*, V is the voltage in *volts*, ϕ is the work function of the tip in *eV*, A is the total emitting area in cm^2, α is the Nordheim image-correction term (~1), μ is the Fermi level in *eV*, r is the tip radius in *cm*, and k is the field reduction factor which is related to the tip shape. A plot of $ln\ (I/V^2)$ versus $1/V$ is therefore a straight line of slope $-6.8\times10^7\phi^{3/2}\alpha kr$. If the values of α, k, and ϕ are known, the tip radius can be calculated from the slope of a Fowler–Nordheim plot. The slope (S) of a Fowler–Nordheim plot can be simplified from Equation (2.26) [55, 56],

$$S = \left|\frac{d(\ln(I/V^2))}{d(1/V)}\right| = \frac{6.8\times10^{-7}\alpha}{\beta}\phi^{3/2} \tag{2.27}$$

$$\beta = \frac{1}{kr} \tag{2.28}$$

where β is the field enhancement factor in cm^{-1}. The accurate k value cannot be calculated from the Fowler–Nordheim plot so the field enhancement factor (β) was calculated in this study. A sharper tip can produce a higher field emission current and gives larger β. Good field emission properties of tips are important for taking SPELS spectra.

2.5 Scanning Probe Energy Loss Spectroscopy (SPELS)

The scanning probe energy loss spectroscope (SPELS) is a hybrid instrument which combines an STM with an electron energy analyser to achieve local EELS measurements, as shown in Figure 2.15.

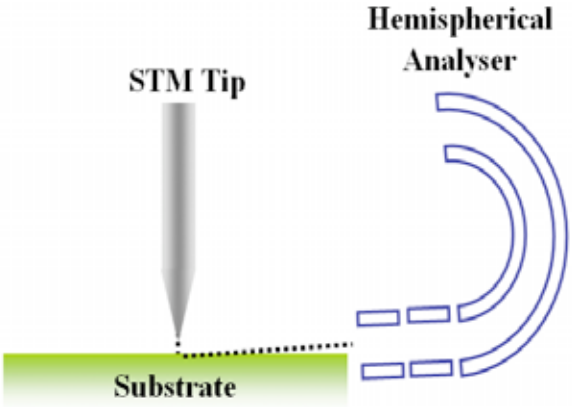

Figure 2.15: Schematic diagram of a Scanning Probe Energy Loss Spectroscopy (SPELS). Electrons are emitted from the STM tip and then scattered from the surface and collected by the analyser.

SPELS combines the spatial resolution of STM and the electronic spectroscopy of EELS for surface analysis. The principle is that a normal STM tip is first brought into proximity with a surface. The STM tip is then retracted above the vacuum level and operated in field emission mode. Negative bias, for example -200 V, is applied to the STM tip and the field emission current to the sample is measured. The energy of the electrons incident on the surface from the STM tip is detected using a hemispherical electron energy analyser revealing a local electron energy loss spectrum. However, the STM tip is located very close to the sample when operating in field emission mode. The trajectory of backscattered electrons reflected from the surface is strongly influenced by the electric field around the tip. If the kinetic energy of the backscattered electrons is greater than potential of the electric field, the backscattered electrons can escape the tip-

sample junction to reach the analyser. The potential energy diagram of the SPELS is illustrated in Figure 2.16.

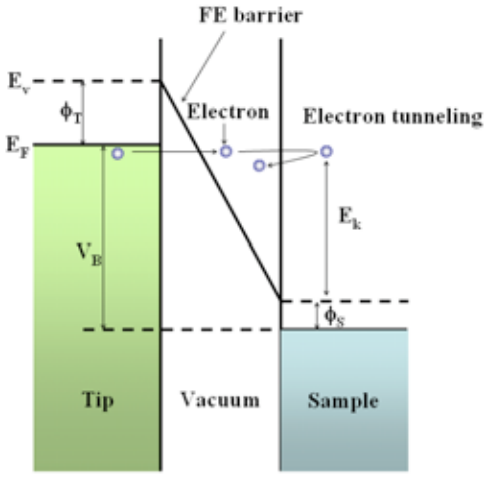

Figure 2.16: Schematic energy diagram of electrons for a SPELS. E_v, E_F, V_B, and E_k are vacuum level, Fermi level, the bias between a tip and a sample, and the kinetic energy of an electron near the sample surface, respectively. Φ_s and Φ_T are the work function of the sample and the tip respectively.

A negative voltage is applied to the tip and electrons are emitted toward the sample across the field emission barrier. Using a sharper tip reduces this barrier and electrons can be more easily emitted. The hemispherical analyser detects electron energies relative to the vacuum level. Therefore, $V_B = E_k + \Phi_s$, where V_B, E_k, and Φ_s are the bias between tip and sample, the kinetic energy of an electron near the sample surface, and work function of the sample, respectively. Some of the electrons can also be reflected to the vacuum region at the sample surface. The electron kinetic energy at the sample surface after elastic scattering is given by $(E_B - \Phi_s)$. For example, typical values of incident energy, E_B, and work function, Φ_s, can be 100 eV and 4.5 eV (for graphite), respectively; this corresponds to a kinetic energy of 94.5 eV.

Previous SPELS work

SPELS was designed at the Nanoscale Physics Research Laboratory (NPRL) approximately 10 years ago and various results have demonstrated the potential of SPELS. Festy *et al.* first reported the imaging of an Si (111) surface by using a backscattered electron signal from an STM operating in field emission mode [12]. In this work, the backscattered electrons were collected by a four-grid retarding field analyser and the analyser was mounted parallel to the sample [57]. The field emitted electron trajectories in SPELS were theoretically calculated by Palmer *et al.* [10]. Figure 2.17 shows the simulation of electron trajectories in SPELS. Figure 2.17(a) shows the electron trajectories from the tip arriving on the surface. The parameters used are a tip–surface distance of 100 nm, the tip bias voltage of –100 V, and the field emission current of 1.16 nA. The current density profile on the surface is shown in Figure 2.17(b).

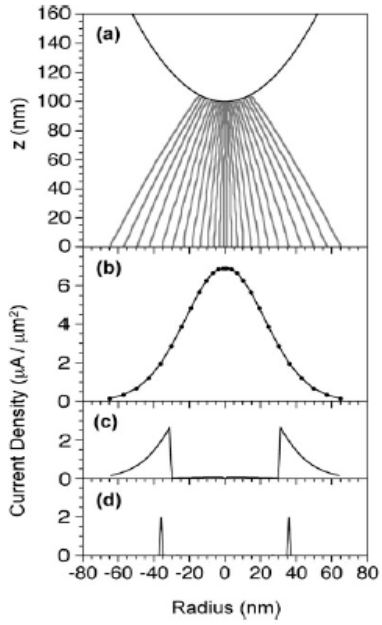

Figure 2.17: Simulations of electron trajectories in SPELS: (a) The trajectories of the field emission from the tip; (b) The current density profile; (c) Current density profile available to the analyser; (d) The current density profile at a particular analyser angle of 85° from the surface normal. From [10]

The width of the current density profile is 100 nm, which is of the same order as the tip–sample separation. The measured current density profile is shown in Figure 2.17(c). The current density profile is strongly suppressed underneath the axis of the tip so that the electrons reflected from the surface in this region are strongly influenced by the electric field. Figure 2.17(d) shows a plot of the sample current density corresponding to those electrons subsequently reflected and collected by the analyser at an angle of 85° with respect to the surface. The simulations suggest that a spatial resolution of 1–10 nm should be achieved in SPELS. Festy *et al.* also experimentally proved that SPELS achieves resolution below 50 nm [11]. Eves *et al.* reported angle resolved SPELS measurements [13]. Figure 2.18 shows the SPELS spectra of silicon and graphite.

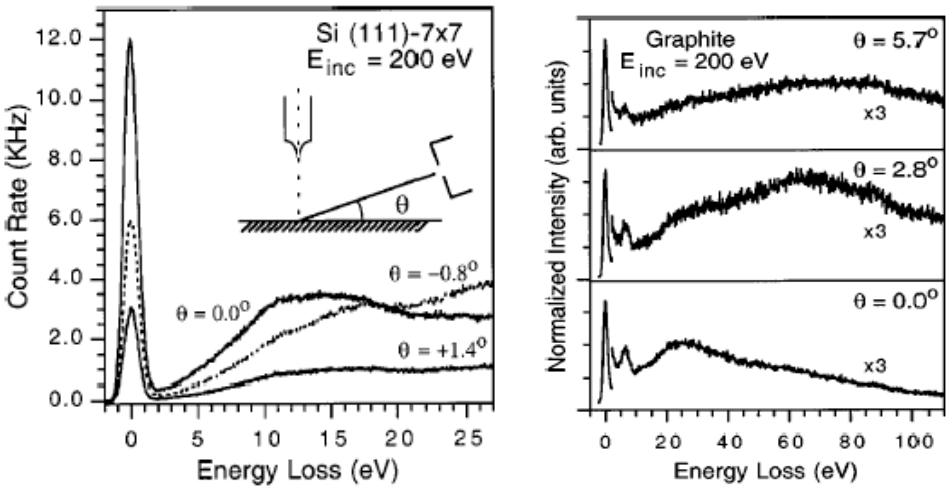

(a) (b)

Figure 2.18: Angle resolved scanning probe energy loss spectra of (a) Si (111)-7×7 and (b) graphite. Spectra taken from three different analyser angles. From [13]

Figure 2.18(a) shows a SPELS spectrum from the Si (111)-7×7 surface obtained at three different angles. It can be seen that the reflected signal is strongest parallel to the surface. The reason for this is that the backscattered electrons are suppressed by electric field caused by the tip. This suggests that the grazing angle is the optimum position for

the analyser. Figure 2.18(b) also shows the angle resolved SPELS spectra of graphite. Of interest is that the energy loss features at ~ 65 eV are only obtained at an angle of 5.7° from the surface. This effect was attributed to the long-range repulsive field due to the bias voltage on the tip.

SPELS spectra have also been obtained from a variety of surfaces. Pulisciano *et al.* reported surface plasmon excitation of Au and Ag films in SPELS [14]. This paper concerned the SPELS spectra of Au and Ag films as a function of incident energy. The surface plasmons of Ag and Au were observed at 3.6 eV and 2.7 eV respectively. When the tip bias voltage increased from –102 V to ~ –300 V, the surface plasmon showed different features. In the Ag case, the surface plasmon peak (3.6 eV) can be seen clearly. However, in the case of Au, the surface plasmon was completely suppressed above -300 V. This indicates that the Au plasmon at 2.7 eV is dominant at a field emission energy of -102 V, but the interband transitions become dominant at -300 V. Yin *et al.* reported local secondary-electron emission SPELS spectra of a graphite surface [15]. The unoccupied π band at 6 eV, and unoccupied σ bands at 2, 11.5, and 17.5 eV were observed in the low kinetic energy region. This corresponds to results seen with a conventional SEE spectrometer [58]. These results demonstrate that SPELS provides local electronic information through energy loss spectra and secondary-electron emission spectra.

2.5.1 Related Work

There have been many new instruments developed, based on the STM. Here different types of instruments which use a field emission current in an STM are introduced.

Mizuno *et al.* developed a prototype instrument which combined STM with a low-energy electron diffraction (LEED) [59–62]. The STM tip was used as a field emission

gun and detected electron scattering patterns. The diffraction of electrons can be used to determine surface structure using a LEED. They show the typical scattering patterns of Si substrate using a field emission current [61]. It has shown two bright regions, which consist of inelastically and elastically scattered electrons. However, the specific diffraction patterns of surface structure have not been obtained yet. This result shows the possibility that the STM-LEED can be used either to obtain an STM image or to determine the surface structure.

STM-Auger electron energy spectroscopy (AES) is another type of new instruments which also uses the field emission current from STM. Miyatake *et al.* developed a combined system of Auger electron analysis with elemental analysis of the surface [63, 64]. The STM was combined with a cylindrical mirror analyser. STM-AES instrument can thus obtain both topographic STM image and element analysis of surface. They are demonstrated a Si Auger electron successfully from a clean Si (111) surface using an STM-AES instrument.

Two further groups have developed a field emission STM which is very similar to that of SPELS. A field emission STM known as "FE-STM", combined with an energy analyser to perform surface electron spectroscopy, was developed by Tomitori *et al.* [65–68]. A cylindrical sector field energy analyser with an electron transfer lens was used to detect both plasmons and Auger electrons on a surface. The difference between FE-STM and SPELS is the experimental parameters. In their experiment, the distance between the tip and the sample is 0.5 mm and a several kilovolts of bias are applied to the tip. Using these experimental parameters it is difficult to obtain the spatial resolution information from the surface.

Recently Zhou *et al.* have also reported an instrument similar to SPELS [69]. They are focused on the energy dispersive multichannel electron energy analyser. It can

also detect electrons from the surface perpendicular to the incident electron beam in a wide azimuth angle range of 245°. This new type of analyser has improved the detection efficiency by two orders of magnitude compared with traditional electrostatic analysers. They have investigated obtaining the energy loss spectrum of graphite using this instrument. The count rate of elastic peak of graphite is improved about 50 times but they have not shown any interesting plasmon peaks of substrate.

An important part of field emitted STM is the STM tip itself. In order to field emit from an STM tip, a high negative bias on the tip is required. However, the tip then generates a strong electric field which has an effect on the trajectory of the scattered electrons. A suggested solution is to use an electric shield layer around the tip (Figure 2.19) [63, 66]. Two types of electric shields to reduce the field effect have been tried.

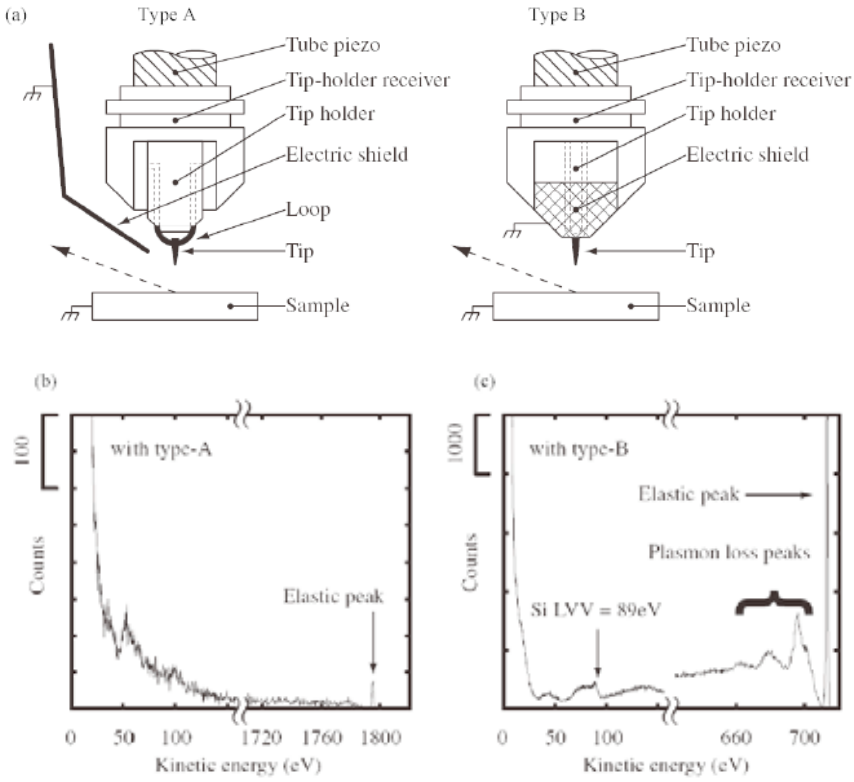

Figure 2.19: Different types of electric shields: (a) Schematic diagram of STM tips with electric shields, labelled Type A and Type B; (b) Energy spectra of Si (111) surface using Type A and (c) using Type B. From [66]

Type A uses an external metal shield and Type B uses Au plating and grounding of the tip holder body. The more efficient shielded tip holder, Type B, has detected surface bulk plasmons, and a Si Auger electron peak is clearly shown in Figure 2.19(c). However, Type B does not shield the sidewall of the tungsten tip, which projects several millimetres beyond the shield, and this can cause an adverse electric field. Even though they have successfully decreased the electric field effect, they still require a high negative voltage, few kilovolts, and the distance between tip and sample is still around 0.5 mm.

In this work, a specially designed silicon tip with an integrated shield was used to suppress electric field effects. The grounding layer was fabricated on the tip using microfabrication processes. The shield effect on the microfabricated STM tip will be discussed in Chapter Five.

2.6 Scanning Probe Electron AnalyseR (SPEAR)

Another way to obtain additional information in a STM is to combine STM measurements with local optical spectroscopy. Light sources are able to excite the core electrons so that specific excitation under STM can determine different chemical species on the surface, furthermore, valence band spectra also reveal electronic properties.

Walle *et al.* presented the first photoconductive STM measurements on a GaAs substrate [70]. They used a 150 W halogen lamp, or a 5 mW HeNe laser as a light source, and successfully measured the I-V characteristics of the GaAs substrate with and without illumination. The combination of a laser and an STM has been used to obtain additional information between the tunnelling junction and the surface. Later, the method was developed for various light sources combined with an STM [71]. Smith *et*

al. observed that optical excitation shows a resonance effect with an electronic absorption of an organic sample [72]. Laser-assisted STM, however, often suffer from thermal effects between tip and surface junction caused by the intense radiation [73]. In order to overcome thermal effects, different type of light sources have been studied. Saito *et al.* have demonstrated the elemental analysis of Ge nano-islands using STM with a synchrotron radiation hard-X-ray microbeam [74]. In this work, the tip current spectra were successfully obtained for Ge nano-islands on the Si (111) surface by changing photon energy across the Ge absorption edge with a spatial resolution of the order of 10 nm. Eguchi *et al.* also used STM with synchrotron radiation light to obtain element specific images from the photo-induced current with a spatial resolution of less than 20 nm [75]. In that study, the light beam spot diameter is large so that photoinduced current could be collected from substrate, but was therefore also collected from sidewall of the tip. A glass-coated tungsten tip was therefore developed to avoid induced current from the sidewall [76]. The photo-induced current using an insulator-coated tip was reduced by a factor of 40, showing that blocking of photo-induced electrons from the sidewall of the tip is important in photo-assisted STM.

In the Nanoscale Physics Research Laboratory, we are developing a new type of a photo-assisted STM analyser, which is called the 'Scanning Probe Electron AnalyserR (SPEAR)'. SPEAR combines photoelectron spectroscopy (PES) and STM.

PES is typically classified by the incident photon energy, for example, the ultraviolet regime (5 ~ 100 eV, UPS), the soft X-ray regime (100~1000 eV, SXPS) and the X-ray regime (> 1000 eV, XPS). The principle of the PES is that the illumination of a surface excites photoelectron which escape into the vacuum. These photoelectrons are then analyzed with respect to kinetic energy $E_{kinetic}$ and momentum p in an electrostatic analyser, as shown in Figure 2.20. The kinetic energy of the photoelectron is given by

$E_{kinetic} = \hbar\omega - \phi - E_B$, where $\hbar\omega$ is photoenergy, the work function, ϕ and binding energy, E_B. PES gives information about the distribution of electrons in the outermost valence or conduction band of the material.

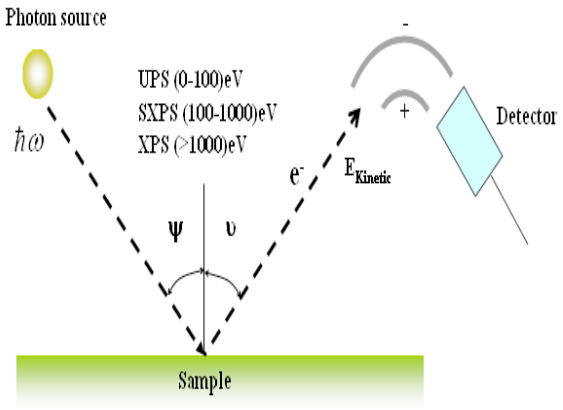

Figure 2.20: Schematic diagram of a photoelectron spectroscopy experiment. Photons are incident on the sample and emitted electrons are analysed by the detector. After [77]

In the SPEAR system, HeI ($\hbar\omega = 21.1eV$) UV lamp is used, similar to UPS. Ultra violet (UV) light excites photoelectrons between the tip and surface junction and the new designed STM tip collects the photoelectrons with a spatial resolution. The SPEAR is shown schematically in Figure 2.21.

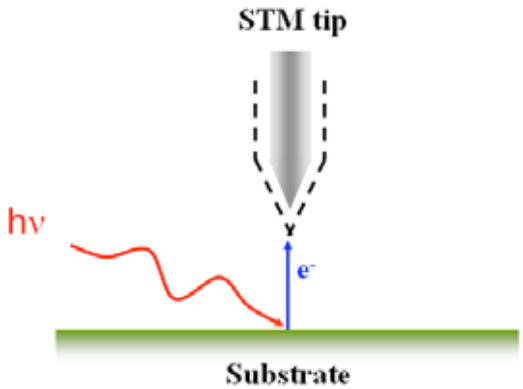

Figure 2.21: Diagram of a Scanning Probe Electron AnalyseR (SPEAR). The STM tip has a multilayered structure which is used as a retarding field analyser. The tip collects the photoelectron from the surface.

In general, a photoelectron spectrometer consists of three components which are an intense monochromatic light source, an energy analyser and an electron detector. In a SPEAR system, these components are combined into the specially designed STM tip, which acts as a retarding field analyser and electron collector.

The limit of the energy resolution in a SPEAR analyser depends on inelastic electron scattering of the photoelectrons in the tip layers. The multilayered silicon tip may be able to perform PES with an energy resolution of 1 eV combined with a spatial resolution between 10-50 nm [78]. The spatial resolution of the SPEAR tip will be limited by a combination of two effects, the tip radius and the geometry of the tip surface function which affects the area from which photoelectrons from the surface can be detected (around 10-50 nm diameter).

Chapter Three

Experimental Techniques

This chapter gives an overview of the microfabrication processes employed to make the tips and of the SPELS instrument itself. Techniques including electron beam lithography, dry etching, thermal oxidation, and thin film sputter deposition are introduced. The SPELS instrument consists of a Scanning Tunnelling Microscope (STM) head coupled to a hemispherical electron energy analyser, mounted within an Ultra High Vacuum (UHV) system. The operating methods for the UHV system and the SPELS are explained. The detailed parameters needed in order to obtain the SPELS spectra are also discussed.

3.1 Microfabrication Processes

3.1.1 Substrate Preparation

Tips were fabricated on a highly arsenic doped N-type silicon <100> substrate (0.0009–0.0004 Ω cm, double side polished wafer, 500 μm thick, Virginia Semiconductor, Inc). The wafer was cut into 1.5 × 1.5 cm size chips before the cleaning processes. All chemicals used were semiconductor grade to avoid any contamination from impurities. The chips were immersed ultrasonically in isopropanol (Riedel-de Haën) for 10 minutes and cleaned in flowing deionized water (Purite Nepune, 18.2 MΩ) to remove any dust particles. The wafers were then dipped into a 1:1 (volume) mixture of concentrated sulfuric acid (H_2SO_4 (95-98%), Fluka) and hydrogen peroxide (H_2O_2 (30%), Riedel-de Haën) for 10 minutes to remove organic contaminants. To remove natural silicon dioxide (SiO_2), the silicon was immersed in dilute hydrofluoric acid (HF, Aldrich) for 1 minutes. After rinsing in deionized water, the substrates were dried in a flow of dry nitrogen. This procedure leads to silicon substrates with a clean, hydrogen terminated surface.

3.1.2 Electron Beam Lithography

Scanning Electron Microscopy

The SEM was the main instrument used to image the microfabricated silicon tips in this thesis. SEM is commonly used to image surfaces with a resolution of a few nanometres. The basic elements of an SEM are shown schematically in Figure 3.1. The SEM consists of an electron gun, electron optics, specimen stage, detector, and vacuum system. The electrons are generated by the electron gun; a lanthanum boride (LaB_6) filament is used and generally operates over the range 1–30 kV accelerating voltage in our system. The electrons are emitted from an electron gun via field emission and these

electrons are focused onto a surface through a special lens system. There are two different lens systems in the microscope: the condenser lens and the objective lens. They control the collimation of the emitted electrons and the focusing of the electrons onto the surface respectively. When electrons are incident on the surface, electrons either secondary electrons or backscattered electrons can be detected. The secondary electron detector is mounted at the angle of around 45 degree (or more) to the beam whilst the backscattered electron detector is usually located at the end of the object lens in close to the sample. Detectors collect the electron and display the results on the screen.

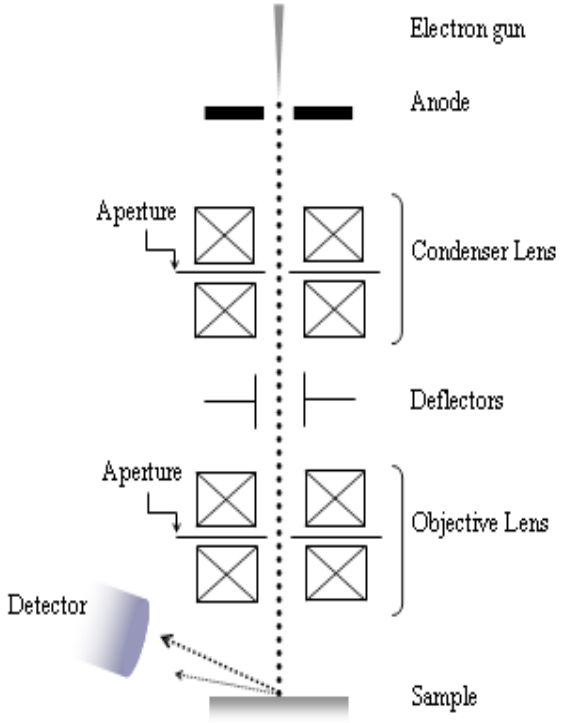

Figure 3.1: Basic elements of an SEM, showing electron gun, condenser, objective lenses, and detectors. Electrons are emitted from the electron gun. The electron beam is collimated and focused by the lens system, and backscattered or secondary electrons from the surface can be detected.

The advantage of SEM is that it can obtain a high resolution image of a sample without causing any damage. The electron–sample interactions can be used to form an image and to give both qualitative and quantitative information. However, a limited range of sample types can be imaged in SEM. Insulating materials accumulate charge on the surface and this causes image distortions by deflecting incident and reflected/emitted electrons unpredictably. In this work, an XL 30 SFEG from FEI was used. For imaging the electron beam energy was set to 5 kV.

Electron Beam Lithography (EBL)

Lithography is the process of transferring a pattern from a mask to a substrate. There are various types usually grouped by the radiation used, for example photolithography, electron beam lithography (EBL), X-ray lithography, ion-beam lithography, and so forth. Photolithography is widely used in industry as its speed enables mass production. Photolithography produces chemical changes in a light sensitive resist coated on the substrate by projecting a beam of light through a shadow coating mask onto the resist. Light of various wavelengths can be used - here we will focus on UV lithography. Typically, a mercury arc lamp will be used, giving light at for example 436 nm (*g*-line), 405 nm (*h*-line), or 365 nm (*i*-line). The resolution (R) of photolithography is dependent on the wavelength according to the following equation [79]:

$$R = \frac{k\lambda}{NA} \tag{3.1}$$

where λ is the exposure wavelength, NA is the numerical aperture of the optical system, and k is a process dependent constant. The resolution dependence of photolithography

on the exposure wavelength limits the minimum feature size. For a typical UV based photolithography system, the smallest achievable feature size might be as much as a micron, and then alternative techniques are required if greater resolution is needed. Electron beam lithography (EBL) is such an alternative lithography technique capable of much better resolution. The substrate to be patterned is coated with an electron sensitive materials known as a resist. The EBL uses an electron beam to chemically alter the electron resist in selected areas, and after exposure the resist is developed in a solvent that selectively removes either the exposed or unexposed resist areas. An EBL system consists of four parts: an electron gun or electron source, an electron optical system, a mechanical stage, and a controller system. The electron gun commonly uses a tungsten filament or lanthanum hexaboride tip and electrons are emitted by applying heating and/or high electric field to the filament or the tip respectively. The emitted electrons are collimated and focused in an electron optical column. The sample is grossly positioned by a mechanical stage under the electron beam and electrostatic fields are applied to the beam to deflect it, and thus pattern the resist. The whole system has to be under vacuum as electron beams are absorbed in air. The pattern to be created is designed using a computer aided design (CAD) program which then controls the deflection of the beam. Because of the initial nature of the 'mask' EBL can be used to create arbitrary patterns far more easily than photolithography which requires a real mask to cast the shadows. There are two types of exposure methods: raster scan and vector scan. In a raster scan, the position of the beam scans back and forth over the whole area to be exposed a line at a time. A second electrostatic field applied by a beam blander is used to turn the beam on and off at each position, allowing the pattern to be built up as a series of dots. In a vector scan system the electron beam scans each area to be exposed only and does not scan over interesting areas except to move from one

exposure area to another. The resolution of the patterns is controlled by the incident beam energy, beam spot size, dose ((sample current of electrons × exposure time) / area of exposure), backscattering of electrons and the resist. Figure 3.2 shows electrons incident on a resist film. Some of the electrons are forward scattered and others are backscattered from the substrate back into the resist. Each time an electron is scattered it deposits energy in the resist – exposing that bit of the resist. Forwardly scattering tends to broaden the electron beam reducing the resolution and is a greater problem the thicker the resist. Backscattered electrons from the substrate can re-enter the resist a considerable distance from the original beam and expose otherwise unexposed areas. This is known as the proximately effect and is particularly a problem in densely patterned resist, where backscattering between closely spaced exposed features can cause total resolution loss.

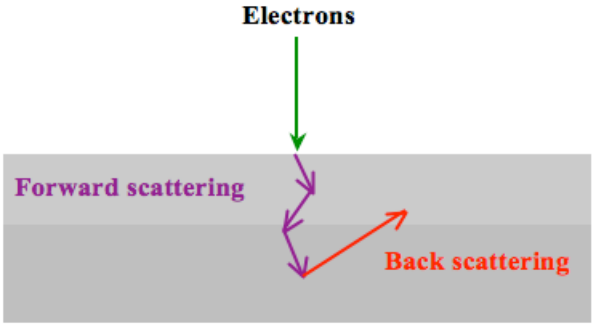

Figure 3.2: Schematic illustration of the electron penetration on the resist coated substrate. Electrons are scattered in the resist film with a small angle scattering event (forward scattering) and a large angle scattering events (backscattering).

Figure 3.3 shows Monte Carlo simulations of the trajectories of incident electrons in the resist and substrate [80]. The resist film thickness was 0.40 μm film coated on a silicon substrate. At 10 keV the backscattered electrons are spread out over distances of the order of 1 μm, while at 20 keV the distance is 3–4 μm.

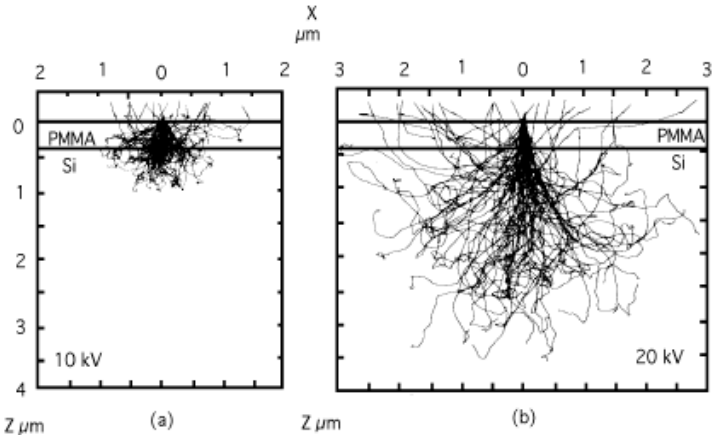

Figure 3.3: Monte Carlo simulations of the electron path in the resist and in silicon for (a) 10 kV and (b) 20 kV. From [80]. The lower electron beam experiences more broadened within the film from forward scattering, whilst the higher energy beams backscattered electrons re-enter the film at much greater distance.

The main advantage of EBL is its ability to create arbitrary patterns with a higher resolution. In practice, 20 nm features are commonly fabricated with EBL and sub-10 nm features are also producible in certain cases (200 keV) [81]. For this work such high resolutions are not required but the ability to produce arbitrary pattern is important.

The EBL tool uses an electron beam to expose selected areas of a resist film. Subsequent processing removes the unexposed (or depending on the resist and process the exposed) areas leaving a pattern on the surface that is used as a mask in subsequent processing. The EBL instrument is a combination of an SEM and a pattern generator (Raith ELPHY Quantum). The pattern generator controls the position of the electron beam when exposing resist, arbitrary patterns can be defined, using CAD software for use in the pattern generator.

In this experiment, EBL was used to produce circular or square resist patterns on the micrometre scale. These patterns were used as a etch mask to create a silicon tip and mesa structures. Negative tone electron beam resist was spin coated onto a silicon wafer and then the resist was exposed with an electron beam of energy 30 kV and a beam

current of approximately 1nA. The primary advantage of EBL in this process, compared to the photolithography system, is that patterns can be easily aligned to previously fabricated structures using a precise stage. The alignment is crucial in this fabrication processes. To create a silicon tip on a high mesa structure, it was necessary to use two separate lithography steps, to define first the mesa structure etch mask and after etching the mesa, the silicon tip etch mask. Typically, in multi steps EBL, alignment structures are produced on the substrate before further processing, which can be seen through the thin resist films normally used. In this work, the creation a high aspect ratio structures required the use of very thick resist films which would have obscured surface alignment features. Known irregularities at the edge of etch chip were therefore used to align the chip at each stage.

Sample Preparation

Patterned negative tone resist was used as a mask so a thicker resist was required. The resist can be also etched by etchant gases during dry etching processes. Negative tone SU-8 (SU-8 2007, Microchem) is a thick resist which is a novolak epoxy based resin able to form a film from 0.5 μm to more than 200 μm in thickness. It is highly viscous and commonly used in microelectromechanics (MEMS) fabrication processes where high aspect ratios are required. Films of SU-8 resist were spin coated onto the silicon substrate using a spin speed of 100 rpm for 10 seconds followed by 1000 rpm for 120 seconds resulting in a coating of approximately 15 μm thickness. A post application bake at 95 ^{o}C for 3 minutes was applied to remove any remaining solvent in the resist. An array of patterns was written in the resist using a Scanning Electron Microscope (SEM; FEI XL30SFEG) with a pattern generator attachment (Raith Elphy Quantum). The resist film was exposed at 30 kV using a dose of 100

$\mu C/cm^2$. A post exposure bake at 95 ^oC for 3 minutes was applied before development in developer solution (Microchem) for 10 minutes, followed by an isopropanol rinse and nitrogen drying.

3.1.3 Dry Etching

Etching is the process of transferring the pattern from the resist to the substrate. There are two types of etching methods: dry etching and wet chemical etching. Dry etching is physically or chemically etching the silicon surface in the gas phase. In general, physical dry etching uses an ion bombardment method and chemical dry etching is done by reactive species generated, for instance in a plasma, from an etchant gas. Wet etching uses chemicals such as acids to chemically etch the silicon surface in liquid. In this work, both dry and wet etches are used. Dry and wet etching each has its advantages and disadvantages. Wet etching can typically only achieve isotropic etching (equal etching rate laterally and vertically) but requires little equipment and can be extremely selective (etch only certain materials and not others) whilst dry etching allows the isotropy (or anisotropy) to be carefully controlled, but requires complex equipment and is usually less selective.

Plasma Etching

Plasma etching is the most common dry etching process in the microfabrication area. A plasma is a fully or partially ionized gas composed of equal numbers of positive and negative ion and also possibly some unionized molecules. Figure 3.4 shows steps in the plasma etching reactions.

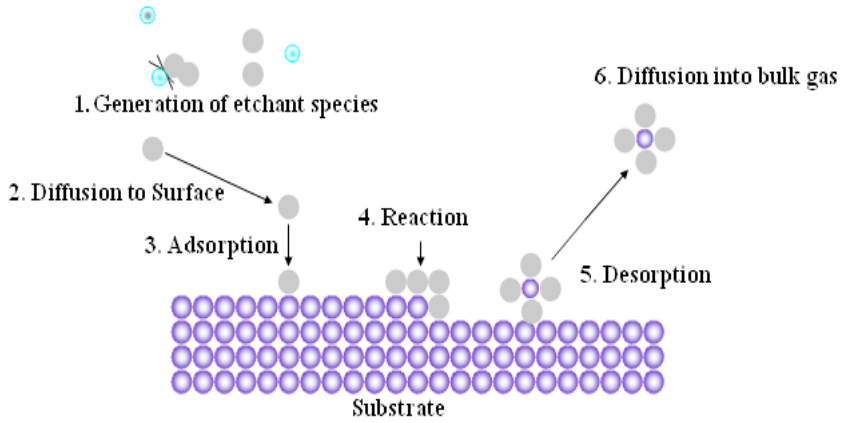

Figure 3.4: Plasma etching steps: 1. Generation of etchant species; 2. Diffusion to surface; 3. Adsorption; 4. Reaction; 5. Desorption; 6. Diffusion into bulk gas.

The etchant gas, for example CF_4, SF_6, or O_2, is introduced into a vacuum chamber. The gas used depends on the material to be etched. Radio frequency (RF) power is applied between two electrodes in the vacuum chamber. The RF field causes oscillation of electrons so that collide with the neutral gas molecules, forming ions and electrons, for example, as in the following chemical reaction [82] (3.2).

$$CF_4 + e^- \rightarrow CF_3^+ + F^* + e^- \qquad (3.2)$$

The radical, F^*, react with the substrate to form volatile products

$$Si + 4F^* \rightarrow SiF_4 \uparrow \qquad (3.3)$$

and the volatile products are pumped away through an exhaust line.

Reactive Ion Etching (RIE)

In RIE the reactive species in the plasma are generated with a high RF power supply as above, at a pressure range of 10^{-3} to 10^{-1} Torr. The pressure in the chamber affects the etching reaction. For example, the reaction mechanism goes from physical sputtering (< 100 mTorr), through physical-chemical (100 mTorr range), to chemical etching (> 100 mTorr) [82]. In chemical etching, the substrate is etched using a reactive etchant species. In sputtering etching, the substrate is bombarded by ion, namely momentum transfer between energetic Ar^+ ions and the substrate surface. Sputtering tends to lead to a more anisotropic etch whilst chemical etching is more isotropic due to their respective working methods. Therefore RIE can control etch profile through a combination of physical sputtering with chemical reaction. Isotropic or anisotropic etching is controllable by the plasma condition. At low pressure (0.1 mTorr ~ 1 mTorr), the etch rate is slow and the etch profile has less selectivity. The impingement rate of the sputtering on the horizontal substrate is greater than at the sidewalls so anisotropic is dominant etching profile. At high pressure (> 100 mTorr), isotropic chemical etching is dominant, and selectivity improves.

Electron Cyclotron Resonance (ECR) Microwave Plasma Etching

ECR etching is performed using high-density plasma. RF power is applied to two electrodes to generate plasma. A static magnetic field and microwave frequency power is then applied to accelerate free electrons in the plasma. The electrons move in a circular motion at the ECR frequency and the electrons are resonated by the microwave power and the magnetic field. The interaction between the microwave power and the magnetic field creates a high-density plasma at a low pressure so the etch rate is relatively high with small RF powers and more selectivity and higher anisotropy than

RIE. The plasma density can be controlled by changing the input microwave power and the gas pressure.

Figure 3.5 shows SEM images of a silicon structure produced by (a) ECR etching and (b) RIE. In each case the same dimension SU-8 resist mask and substrate was used. The ECR etch duration was 40 minutes, whilst the RIE lasted 20 minutes. The etchant was SF_6 in both cases. The resist was slightly deformed during ECR etching so that the silicon structure was etched with a sloped profile and a step. However, with RIE the undercut profile is significantly greater, demonstrating the higher levels of isotropy under RIE.

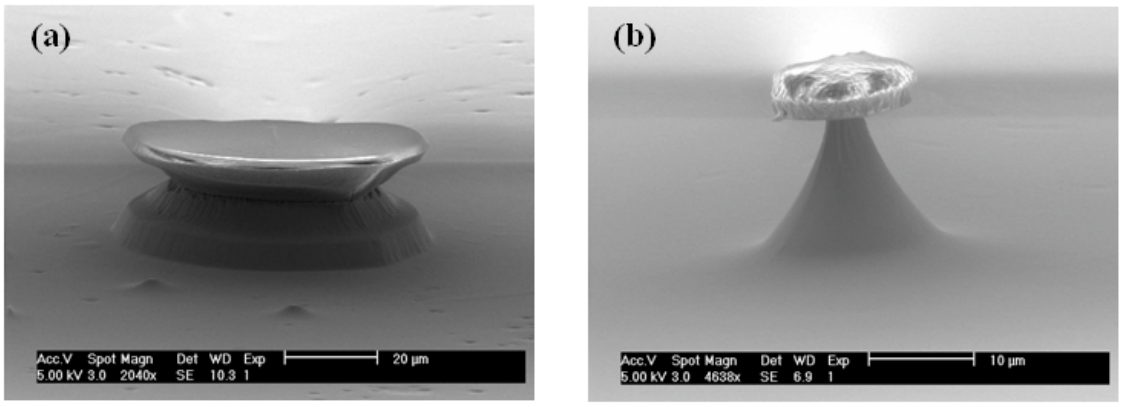

Figure 3.5: SEM images of a silicon structure produced by (a) ECR etching and (b) RIE with an SU-8 resist mask still apparent on the etched silicon structure.

RIE and ECR Processes

The production of a silicon tip on a mesa structure relies on a combination of isotropic and anisotropic etches. To etch the silicon isotropically RIE was used, and ECR etching was utilised for anisotropic etching. The equipment used for this work was a Plasmalab 80^+, manufactured by Oxford Instruments Plasma Technology. This equipment is a combination of both RIE and ECR systems. The plasma reactor consists of opposed parallel plate electrodes in a vacuum chamber ($P \sim 5 \times 10^{-5}$ mbar) and the electrodes

have a water-cooling system to maintain a constant temperature during the etching procedure. There is three gas lines: sulphur hexafluoride (SF_6), tetrafluoromethane (CF_4), and nitrogen (N_2), where SF_6 and CF_4 are etchants and N_2 is for venting. An automatic pressure controller allows pressures in the range 1 to 70 mTorr. Adjusting the pressure allows one to control the plasma density, and thus influences anisotropy, etch selectivity, and speed of etching. The maximum radio frequency (RF) power available for RIE is 200 W at 13.56 MHz and the maximum microwave power for ECR etching is 250 W at 2.45 GHz.

Etching parameters, such as the SF_6 flow, RF powers, RF pressure, and etching time were varied. The optimized etching parameters for silicon tips fabrication were RIE at a pressure of 50 mTorr with 60 sccm of SF_6 and an RF power of 125 W, and ECR etching at a pressure of 1 mTorr with 5 sccm of SF_6, an RF power of 20 W, and microwave power of 250 W.

Deep Reactive Ion (DRIE) Etching

In order to fabricate a high-aspect-ratio structure, the fast etch rate would be highly desirable. The etch rate for silicon substrates is less than 1 μm/minute in the case of RIE and ECR etching. Therefore, it almost takes over 3 h to etch to a height of 150 μm. DRIE is an anisotropic etch process with high aspect ratio silicon microstructures and a high etch rate. The plasma is generated by an inductively coupled coil generator with the power operating at 13.56 MHz. The inductive coupled plasma source produces an axial RF magnetic field from a helical resonator combined with an electrostatic shield [82]. This source creates high density, low pressure and low energy plasmas by coupling electrons to the RF magnetic field. The DRIE technique was further developed by Bosch GmbH to improve the etch rate [83]. DRIE can also be applied to avoid

undesirable thermal stress during etching and protects the sidewalls during etching leading to a more anisotropic etch. However, in this study, we are interested curved sidewall structure, which has slightly isotropically etch profile.

Figure 3.6 represents the schematic diagram of the DRIE procedure. DRIE consists of two steps: etching and passivation. The first step is an etching process using an SF_6 etchant (Figure 3.6(a)). The radical formation is [84],

$$SF_6 + e^- \rightarrow S_xF_y^+ + S_xF_y^* + F^* + e^- \quad (3.4)$$

The second step is the deposition of a passivation layer, for example by ionization of C_4F_8, to create a polymer (C_xF_y) layer on the substrate (Figure 3.6(b)). This process can be represented as follows [84],

$$Si + F^* \rightarrow SiF_x \text{ (volatile gas)} \quad (3.5)$$

$$C_4F_8 + e^- \rightarrow CF_x^+ + CF_x^* + F^* + e^- \quad (3.6)$$

$$CF_x^* \rightarrow nCF_2 \text{ (fluorocarbon polymer)} \quad (3.7)$$

In the third step the SF_6 etching is repeated. Physical sputtering of the ions removes the polymer on horizontal surface whilst not affecting the sidewalls. The subsequent anisotropic nature of the SF_6 etch cleans the passivating layer off the horizontal features more quickly than the sidewalls, and thus etching of the sidewalls can be suppressed (Figure 3.6(c)) [84]. This cycle is then repeated while the required etch depth is achieved, as shown in Figure 3.6(d). By continuously alternating between etching and passivation very high aspect ratio features with highly vertical sidewalls can be achieved.

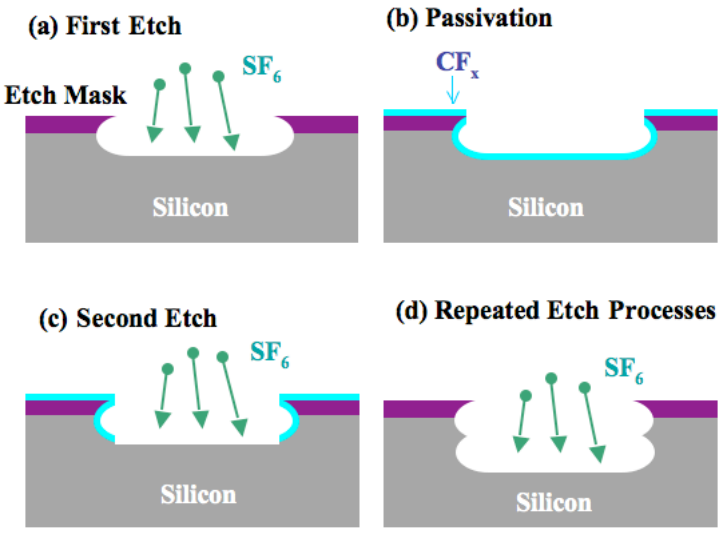

Figure 3.6: Schematic diagram of DRIE procedures: (a) Silicon etching using SF_6; (b) CF_x polymer layer deposition; (c) Second etch; (d) The process cycles. After [85]

A Surface Technology System (STS) deep reactive ion etcher (DRIE) is used to produce the high mesa structure required. The DRIE equipment uses the Bosch process to etch high aspect ratio features with well controlled (vertical) sidewall profiles [85].

A resist film was prepared on a silicon wafer and patterned using EBL. The silicon substrates were then etched using the DRIE process. For this application the optimal parameters were found to be 158 cycles of 12 seconds etching and 5 seconds passivation per cycle with 130 sccm of SF_6, 13 sccm of O_2, an RF power of 600 W and 100 sccm of C_4F_8. The profile of the mesa structure in the multilayer silicon tip was critical to ensure good continuity in the subsequently deposited metal layer. In general, DRIE produces extremely vertical sidewalls as shown in Figure 3.7(a).

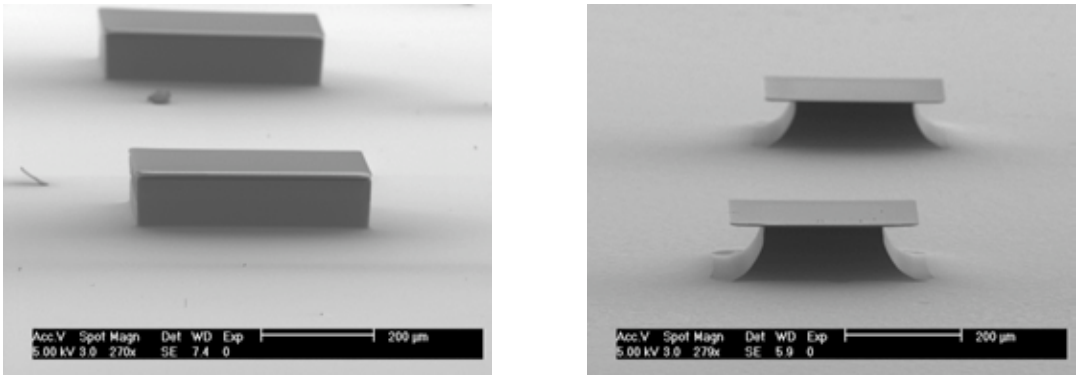

(a) (b)

Figure 3.7: SEM images of intermediated mesa structures formed by DRIE: (a) vertical sidewalls and (b) curved sidewalls. The height of the mesa is 95 μm with the SU-8 resist mask still evident on top of the mesa structure.

However, to ensure good metallization of the feature, a sloped sidewall was required as shown in Figure 3.7(b). The 400 × 400 μm size square patterns in Figure 3.7 were both etched with the same parameters other than temperature control of the sample. In Figure 3.7(a), the sample was loaded directly onto the electrode plate. The temperature of the electrode was controlled, and helium was used between the sample and the electrode to maximize heat transfer and thus minimize the sample temperature during DRIE. This is the normal DRIE process. However, to achieve the profile seen in Figure 3.7(b), the sample was mounted onto silicon wafer coated with a thick photoresist film SRP200-7 (Rohm and Hass). The SRP200-7 resist was spin coated at 800 rpm for 2 minutes onto a silicon wafer and post application baked at 100 °C for 1 hour. The sample was mounted onto the SPR200-7 film whilst it was still hot (and thus soft) to give a good mechanical connection. The thick SPR200-7 photoresist film thermally isolated the sample from the electrode plate so that the temperature of the silicon sample was higher. The passivation layer protecting the sidewalls is affected by a higher temperature and the passivation layer may not protect as effectively, resulting in less vertical sidewall etching as shown in Figure 3.7(b).

3.1.4 Thermal Oxidation

Tip oxidation sharpening is a well-known technique to reduce radius of the apex using a thermal oxidation/oxide stripping. Thermal oxidation is very simple method and the SiO_2 layer is grown very uniformly onto a silicon substrate. Silicon is consumed in the process as shown in Figure 3.8.

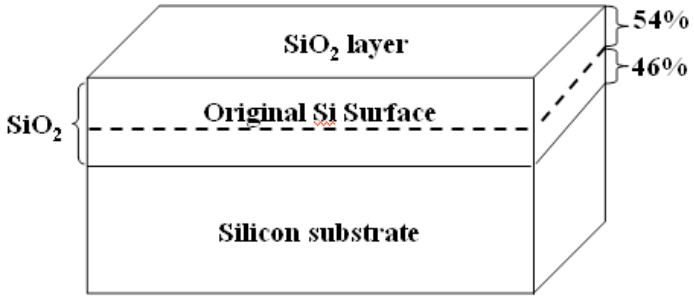

Figure 3.8: Thermal oxide layer onto a silicon substrate. A 46% of silicon layer was consumed to grow 54% of silicon dioxide layer.

The thickness of consumed silicon layer (X_{si}) can be calculated by the following Equation (3.8) [86],

$$X_{si} = \text{Thickness of oxide layer } (X_{oxide}) \times \frac{\text{Molecular density of } SiO_2 \; (2.3\times10^{27}\, molecules/cm^3)}{\text{Atomic density of Si} \; (5\times10^{22}\, atoms/cm^3)} \quad (3.8)$$

Therefore, the thickness of consumed silicon layer (X_{si}) to the resulting oxide layer thickness (X_{oxide}) is

$$X_{si}=0.46X_{oxide} \quad (3.9)$$

Agache *et al.* investigated thermal oxidation sharpening of the silicon tips, as shown in Figure 3.9 [87]. Initially a SiO_2 layer is grown consuming silicon. This is then

removed with an HF etch leading to thinning of the tip and in particular sharpening of the apex.

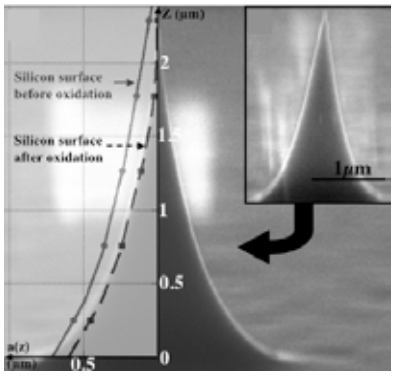

Figure 3.9: Simulated profile of the silicon tip surface. Inset shows the SEM image of oxidised silicon tip. From [87]

Here explains a tip sharpening process in this study. The radius of etched tips was ~ 20 nm. The tips were further sharpened by oxide stripping. A SiO_2 layer is formed on the silicon surface by thermal oxidation using a tube furnace (Carbolite) with O_2 and N_2 supplies. Thermal oxidation of the silicon tip was carried out by heating the tips to 1000^oC under an O_2 atmosphere for 1 hour. The thickness of the SiO_2 layer is approximately 60 nm. The SiO_2 layer on the tip was then removed using HF which selective etches SiO_2 and not silicon, leading to further tip sharpening. The radius of etched tips was ~ 10 nm after the tip sharpening process.

The growth rate of thermal oxidation is 0.8~1 nm/minute so a longer oxidation process can also produce thicker SiO_2 for use as an insulating layer. The thickness of the oxidation layer can be measured using a surface profiler, ellipsometer, or a colour chart. A surface profiler (Dektak^{3}ST, Veeco) was used in this case. The SiO_2 layer was grown on a silicon wafer, coated with resist, and patterned by EBL. HF was used to selectively remove the SiO_2 in areas not protected by resist. The resist was then removed using an

organic solvent, and the SiO_2 thickness was measured as the height difference between the etched and unetched area using a surface profiler.

3.1.5 Thin Film Deposition

Many types of thin film deposition are used in microfabrication. For example, thermal evaporation, sputtering, pulsed laser deposition, and plasma enhanced chemical vapour deposition can all be used to prepare thin films. Sputtering in particular is a common method of depositing thin metal or insulating layers onto a substrate, due to the ability to prepare multilayers easily and the wide choice of materials, such as metals, alloys, semiconductors, and insulators. Additionally, the sputtering method does not require substrate heating and gives better adhesion of the deposited layers to the substrate than thermal evaporation. There are several types of sputtering, including direct current sputtering, RF sputtering, reactive sputtering, and diode sputtering. Here the focus is on RF sputtering. An RF magnetron sputter coater is schematically presented in Figure 3.10. A high-frequency generator is used to generate electromagnetic power in the MHz region. In our experiment, we used 13.56 MHz. The principle of sputter coating is as follows: The sputtered target required for deposition is mounted onto a magnetron and acts as the cathode of an electrical circuit. The substrate to be coated is placed on a grounded plate and acts as the anode. The chamber is then pumped down to ~ 1×10^{-6} mbar. Argon is introduced and then ionized by the RF power applied across the electrodes. During sputtering, the negatively biased target is bombarded with positive argon ions created in the plasma, which strike the target with sufficient force to knock atoms off the target into the vacuum. If the pressure of the Ar gas is too high, sputtered atoms cannot pass through the sputtering gas and are reflected back to the cathode by

collisions. Sputtering at low gas pressure leads to improved film adhesion because the sputtered atoms have a higher energy.

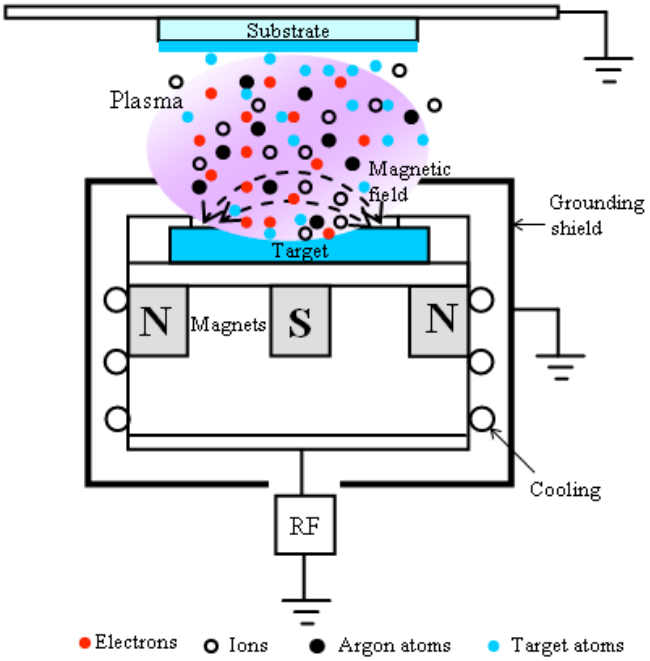

Figure 3.10: Schematic diagram of the RF magnetron sputter coater. The plasma is generated above the target by an RF field and sputtered materials are deposited onto the substrate.

The amount of material, Q, sputtered from the cathode is proportional to power divided by number of gas atoms [86]:

$$Q = \frac{kVi}{Pd} \tag{3.10}$$

where k is a constant of proportionality, V is the working voltage, i is the discharge current, P is a gas pressure and d is a anode-cathode distance. The applied voltage determines the maximum energy with which sputtered particles can escape from the target. The pressure in the sputter chamber determines the mean free path (λ) for the

sputtered material. The amount of sputtered material can be controlled by changing the voltage, pressure, or the distance between the target and the sample.

In order to produce the metal layers required, a multilayered tip was produced. An Edwards 306 RF magnetron sputter coater was used. The sample is placed in a vacuum chamber and the pressure reduced to 5×10^{-5} mbar. A plasma is then generated by introducing argon into the chamber ($P_{Ar} = 2.8 \times 10^{-2}$ mbar) and applying RF power of up to 600 W. The plasma sputters atoms from a suitable target, which are then deposited on the sample. The sample is mounted onto a grounded plate, whilst the target is mounted ~100 mm below the sample on a second electrode which is biased to 400 V (to ensure the plasma sputters the target rather than the sample). The grounded plate contains a water-cooling system to keep the sample cooled. Three target materials (PI-KEM LTD, purity 99.9%) could be mounted simultaneously, allowing sequential deposition without exposing the sample to atmosphere. Prior to depositing a layer the sample was protected with a shutter and the targets were cleaned by sputtering any contaminations or oxides away. The sample was then exposed to the target to deposit a layer. The deposition rate and film morphologies of the materials are dependent on many parameters such as bias between sample and target, gas pressure, and RF power. The optimized sputtering process parameters used in this work are listed in Table 3.1.

Metal layers can be sputtered coated onto the substrate easily but insulating materials, and especially SiO_2, are difficult to sputter because the deposition rate is very slow and the mean free path of SiO_2 in a vacuum is relatively short compared to that of other materials. By reducing the argon pressure and decreasing the sample target separation, the rate of deposition material on a substrate increases. The tip holder was therefore changed to reduce the distance between the target and substrate for SiO_2

sputtering, from 100 mm to 60 mm, and to argon pressure was reduced, as shown in Table 3.1.

Table 3.1: Optimized sputtering parameters used in the Edwards 306 sputter coater

Material	Ar pressure (mbar)	RF Power (W)	Bias (V)	Rate (nm/minute)
Au	$2.8\text{x}10^{-2}$	100	246	~40 nm/minute
Cr	$2.8\text{x}10^{-2}$	300	540	~25nm/minute
HfO_2	$2.8\text{x}10^{-2}$	100	300	~5 nm/minute
SiO_2	$5.0\text{x}10^{-3}$	250	700	~22 nm/minute

Sputtered Hafnium Dioxide (HfO_2) layer

In this study, we also use the sputtered hafnium dioxide (HfO_2) rather than SiO_2 as an insulating layer. HfO_2 is a very well known high-*k* dielectric material and it has much lower leakage current than SiO_2 as shown in Figure 3.11 [88].

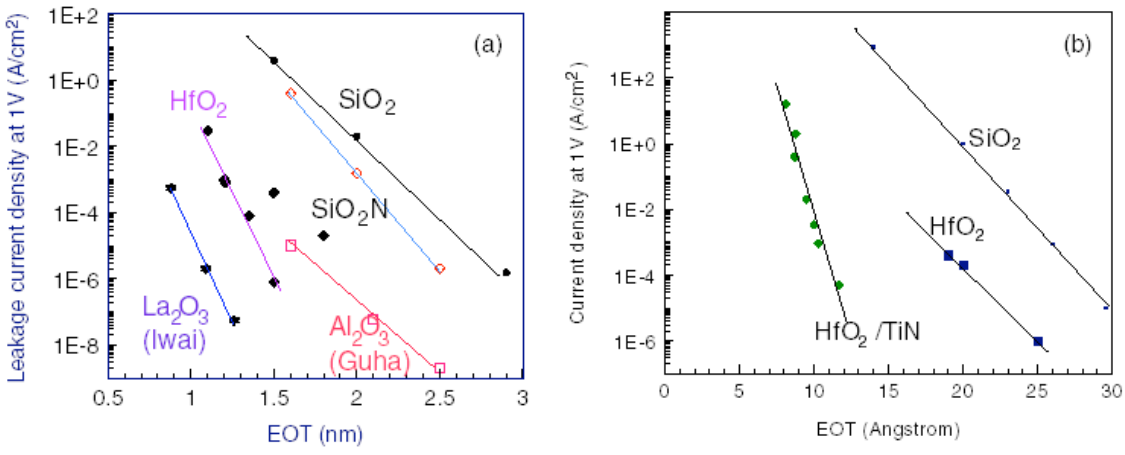

Figure 3.11: (a) Leakage current density versus equivalent oxide thickness (EOT) for various high-*k* oxides and (b) leakage current density versus EOT for HfO_2 with poly-Si gates and TiN gates. From [88]

Table 3.2 compares with properties of SiO_2 and HfO_2. HfO_2 has ~ 6 times larger high-k constant than SiO_2 layer and higher melting point. HfO_2 can also be easily the prepared using sputter deposition onto a substrate, for example an Au surface. The sputtered SiO_2 layer is very hard to make as a uniform layer compared to a sputtered HfO_2 layer, which causes a breakdown of the insulating layer during field emission measurements. For these reasons, sputtered HfO_2 layer was chosen as an insulating material, preferable to SiO_2 for the Au cathode co-axial silicon tip.

Table 3.2: Properties of SiO_2 and HfO_2 compared

	Silicon dioxide (SiO_2)	Hafnium dioxide (HfO_2)
Dielectric Constant (*k*)	3.9	High-*k* (~ 25)
Band gap (eV)	9 eV	6 eV
Melting point (^oC)	1650 ^oC	2758 ^oC

3.2 Apparatus for Experimental Measurements

3.2.1 Introduction to the SPELS Ultra High Vacuum (UHV) System

The properties of the microfabricated silicon tips were tested using the SPELS UHV system. Figure 3.12(a) and (b) show photographs of the SPELS instrument, and a schematic diagram of the SPELS system is shown in Figure 3.12(c). The UHV system consists of three main components: a load-lock chamber, preparation chamber, and STM chamber. The pressures of load-lock, preparation, and STM chambers are approximately 1×10^{-6} mbar, 7×10^{-10} mbar, and 9×10^{-10} mbar respectively. The main chamber contains an STM (Omicron STM-1). A hemispherical electron energy analyser is mounted above the STM chamber and has a linear drive, as shown in Figure 3.12(a),

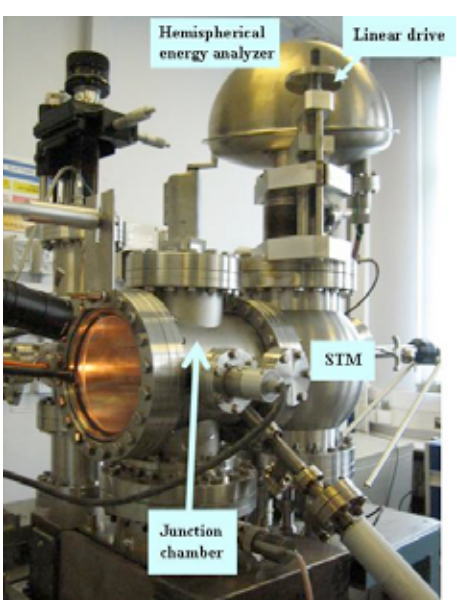

(a)

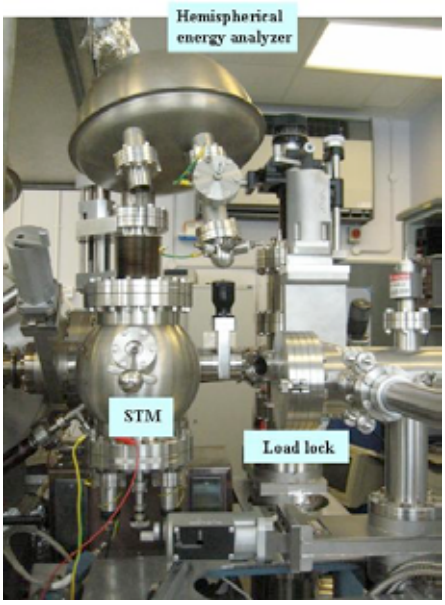

(b)

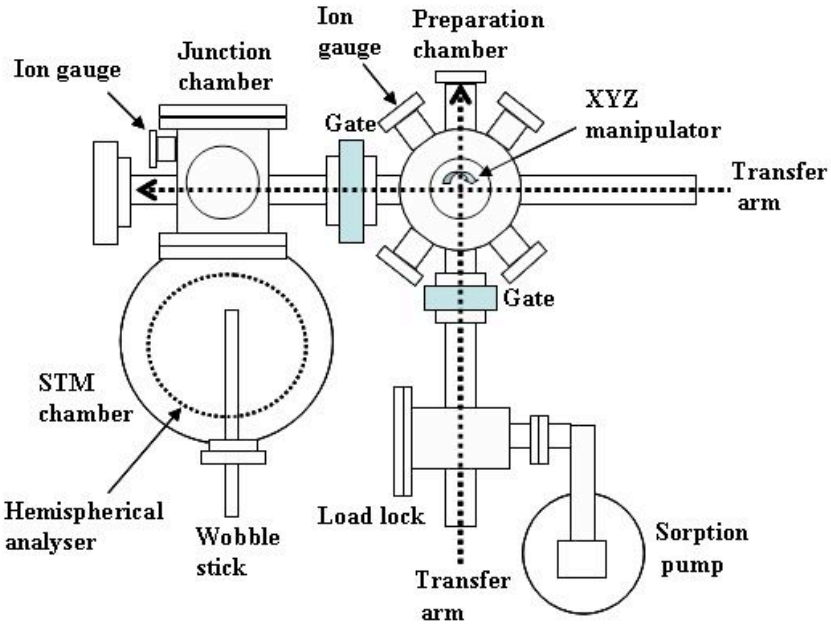

(c)

Figure 3.12: Photographs of SPELS instrument: (a) front side and (b) right side. (c) Top view of a schematic diagram of the SPELS system. SPELS consists of an STM, junction chamber, preparation chamber, load-lock, and hemispherical analyser. Tips and samples are transferred from the load-lock to the STM chamber via the preparation chamber.

in order to raise it for access to the STM head for sample and tip transfer. To measure SPELS spectra the analyser is moved to within 40 mm of the sample. A carousel is also installed in the STM chamber so it is possible to keep several samples and tips in a UHV environment, ready for use. To minimise vibrations the STM chamber is not directly pumped. Instead it is pumped by an ion pump connected to the bottom of the junction chamber, which houses the pressure gage. The junction chamber is connected to the preparation chamber via a gate valve. The preparation chamber is also pumped with an ion pump together with a titanium sublimation pump (TSP). The ion pump is backed by a turbo pump with a rotary roughing pump. The preparation chamber is connected to a load-lock which is also isolated by another gate valve. The load-lock is pumped by a rotary backed turbo pump.

In order to achieve the UHV, each flange has to be well sealed. To achieve this, the steel knife-edges within the flanges are used to cut into the copper gaskets. UHV also requires the use of low out-gassing materials, such as stainless steel, tantalum, and copper. The UHV environment can only be achieved after the system is baked. The SPELS system is pumped first by rotary pump down to 10^{-3} mbar and then by turbo pump down to 10^{-7} mbar. The SPELS system is then baked at 150^{o}C for 2~3 days. Baking is used to remove the water molecules from the chamber walls after the system has been exposed to the atmosphere. Baking was carried out by wrapping the system with heating tape. The maximum recommended temperature of the STM is 170^{o}C, to avoid damaging electronics, but the temperature fluctuated by ±5^{o}C and therefore the baking temperature was set at 150^{o}C for safety. Once the SPELS system had cooled down to 50^{o}C, the ion pump was started to reach a pressure of 10^{-9} mbar. Finally, the TSP was run several times, resulting in a base pressure of 6×10^{-10} mbar in the SPELS chamber.

Tip and Sample Transfer

Tip and sample transfer from atmosphere to UHV is a useful capability to carry out experiments in a UHV system. This is achieved using the load-lock system. The load-lock, turbo pump is isolated using the gate valve and the load-lock is vented with liquid nitrogen via a leak valve. After the tip/sample is loaded into the load-lock, a liquid nitrogen cooled sorption pump is used to make the pressure to 10^{-3} mbar (Figure 3.12(c)). A turbo pump is then used to reach a pressure of 1×10^{-7} mbar which may take several hours, especially if out -gassing materials such as silver paste or silver epoxy have been used in the tip. When the pressure reaches ~ 10^{-7} mbar, the gate valve between the preparation chamber and the load-lock is opened. The tip/sample is loaded into the carrier stub to transfer it from the load-lock to the preparation chamber, as shown in Figure 3.12(c). A schematic of sample and tip transfer via the carrier stub is shown in Figure 3.13(a) and (b) respectively.

The sample is fixed to the sample plate using a tantalum foil strip as illustrated in Figure 3.13(a). Highly oriented pyrolytic graphite (~ 1 × 1 cm) is used as a sample in all experiments. The tantalum strips are spot welded over the sample and onto the sample plate to ensure good electrical contact between the sample and the plate for STM. The carrier stub is screwed onto a transfer arm, indicated by a circular dashed line in Figure 3.13(a), to move the tip/sample from the load-lock to the preparation chamber. The tip was loaded onto the tip plate as shown in Figure 3.13(b) and the tip plate was mounted onto a carrier stub. Next, the carrier stub was attached to the forked transfer arm by insertion into a pinhole. The same method was used to transfer the tip and the sample.

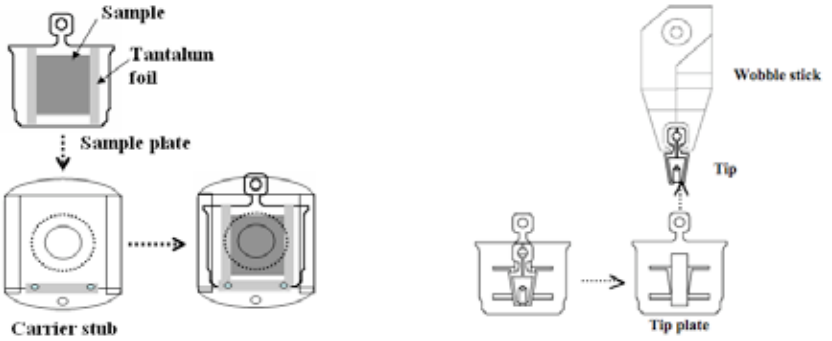

(a) (b)

Figure 3.13: Schematic representation of (a) sample and (b) tip transfer with a carrier stub. (a) The sample is mounted onto the sample plate by tantalum foil welding, and then loaded onto the carrier stub. (b) A wobble stick jaw picks up a tip from a tip plate.

After the carrier stub is transferred to the junction chamber, the tip/sample is removed from the carrier stub using the wobble stick as shown in Figure 3.13(b). To load the sample into the STM the sample is placed into a carousel and rotated by 180 degrees, before picking it up again with the wobble stick and loading it into the STM. The tip can be loaded directly without needing to be rotated.

3.2.2 Scanning Tunnelling Microscopy

An Omicron STM-1 is used in this study. The STM head was controlled by a commercial RHK controller. The Omicron STM-1 is a UHV STM for topographic and spectroscopic imaging of a surface with sub-nanometre resolution. The RHK controller supports all required functions for operating the STM.

The STM head has an eddy damping stage for vibration isolation. The STM head consists of piezotubes on the x, y, and z-axes that were calibrated to move at 5 nm/V. The sample is approached to the tip by coarse motors (RHK PMC-100), and fine control was via the piezoelectrics.

The Omicron STM-1 can apply a voltage to the sample in the range ±10 V. However, to take a SPELS spectrum, a high negative tip voltage is required (~ 100 – 200 V) to generate field emission from the tip. The field emission current can reach several microamperes and could cause damage to the on-board low-noise current amplifier on the STM stage. In order to avoid this, an external low-noise current amplifier was installed on the STM stage so that the field emission current goes directly to a picoameter during SPELS measurement.

The high voltages applied to the tip cause strong fields which can affect the scattered electrons. Therefore, it is important to shield the high voltage piezo, tip holder, and tip substrate using a tip shield constructed from a stainless steel fork and a piece of tantalum foil welded in place. A photograph and schematic of the STM head are shown in Figure 3.14. All modifications of the STM were designed by former students at the Nanoscale Physics Research Laboratory [89].

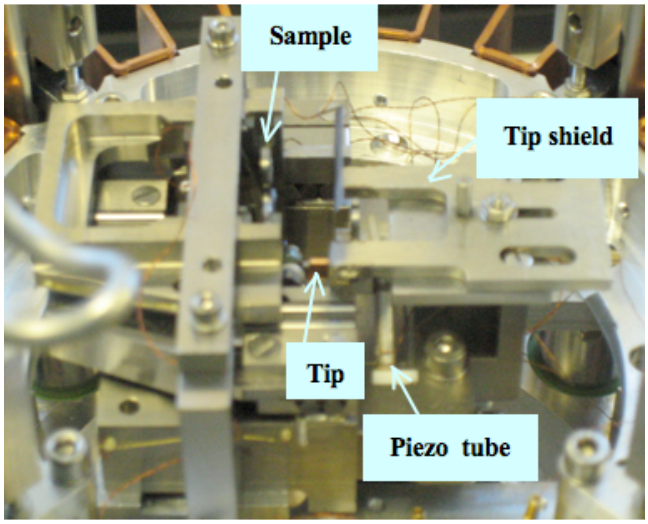

Figure 3.14: Photograph of the STM head with a tip shield. The tip shield can be moved forward to the sample (or backward to the tip) when changing a tip.

3.2.3 Hemispherical Electron Energy Analyser

In the SPELS system, a hemispherical electron energy analyser (VG Scientific 100AX) shown in Figure 3.15, also known as a concentric hemispherical analyser (CHA), was used to collect and analyses the scattered electron. The CHA consists of two main components: the entrance electrostatic lens and the hemispherical analyser. The electrostatic lens of the analyser could be positioned as close as 40 mm from the tip-sample and was installed parallel to the sample surface. The backscattered electrons from the substrate were collected by the electrostatic lens system and focused onto the entrance slit of the analyser. Within the hemispherical analyser the electrons travel through an electrostatic field following a curved path before being focused onto a Channeltron detector.

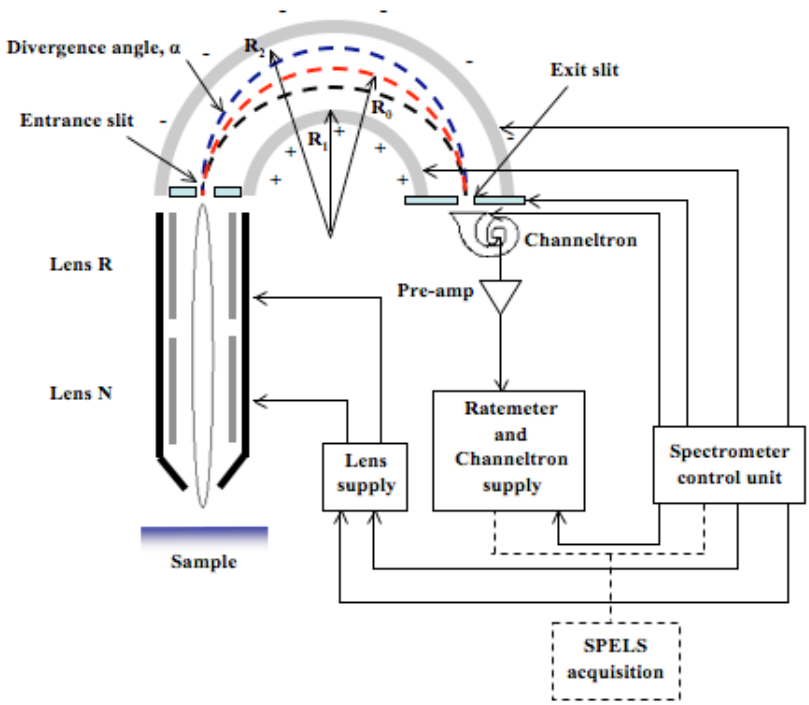

Figure 3.15: Schematic diagram of a VG Scientific 100AX hemispherical electron energy analyser. It consists of lenses, a hemispherical analyser, and a detector (Channeltron). Electrons are focused on to the hemispherical analyser by electrostatic lenses and detected by the Channeltron. The field applied to the hemispheres and the electron energy determines the whether an electron is detected.

Electrostatic lens

The two electrostatic lenses, Lens N (nose element) and Lens R (rear element), act as a coarse filter. There are two operating modes, Constant Retard Ratio (CRR) mode and Constant Analyser Energy (CAE) mode. The first lens (lens N) collects electrons from the analysis area and the second lens (lens R) retards the electrons passing to the analyser.

In CRR mode the rear lens (lens R) is earthed and the electrons are slowed down to an energy that is a constant ratio of the energy to be analysed. For example, if the ratio is 10 and 1000 eV electrons are to be detected, the electrons will be slowed down to 100 eV by the lens and the pass energy will be set to 100 eV. This mode is generally used for Auger and the detection of low kinetic energy electrons.

In CAE mode both lenses (lens N and lens R) are at the same potential and the pass energy (energy at which the electrons enter the analyser) is fixed. For example, if the pass energy is set to a 50 eV, electrons of 1000 eV will be slowed down by 950 eV to be detected. This mode is used when the source has a relatively large beam size and peaks tend to have high kinetic energy.

In this study, CAE mode was used to take SPELS spectra. Spectra were studied with and without applying potential to the lenses. For example when the energy scan range operated from 0 eV to 200 eV, a positive potential was applied to the lenses that ranged from 0 V to 500 V. The spectra were also studied using the same energy range, but without applying any potential to the lenses. This allowed a comparison of lens effects, which will be discussed in detail in Chapter Five.

Hemispherical analyser

The hemispherical analyser consists of two hemispherical electrodes with the radii R_1 and R_2, as shown in Figure 3.15. A potential difference (ΔV) is applied between the outer sphere electrode (negative) and the inner sphere electrode (positive). The electrons pass through the entrance and exit slits that lie on the median radius (R_o) where $R_o = (R_1 + R_2)/2$

The radial electric field $\varepsilon(R_o)$ between the two electrodes is given by [90],

$$\varepsilon(R_o) = \frac{\Delta V R_1 R_2}{(R_2 - R_1) R_o^{\,2}} e \qquad (3.11)$$

where ΔV is the potential difference between the two electrodes, R_1 and R_2 are the inner and outer radii, and e is the electron charge. An electron which follows a path with radius R_o and can thus pass through both the entrance and exit slits must have a centripetal force which matches the electrostatic force provided by the radial electric field $\varepsilon(R_o)$. It can then be written that

$$\frac{m v_o^{\,2}}{R_0} = \frac{\Delta V R_1 R_2}{(R_2 - R_1) R_o^{\,2}} e \qquad (3.12)$$

where v_o is the velocity of the electron at the position of entry. The kinetic energy of the electrons passing through the analyser can be written as E_{pass}, and thus $mv_o^2 = 2eE_{pass}$. Thus Equation (3.12) can be written as

$$\frac{mv_o^{\ 2}}{R_0} = \frac{2eE_{pass}}{R_o} = \frac{\Delta V R_1 R_2}{(R_2 - R_1)R_o^{\ 2}} e \tag{3.13}$$

Therefore,

$$E_{pass} = \frac{\Delta V R_1 R_2}{R_2^{\ 2} - R_1^{\ 2}} \tag{3.14}$$

The size (*d*) of the entrance slit is much smaller than the diameter of the lens, and thus some electrons can collide with and be deflected by slit. This divergence angle α (Figure 3.15) can affect the energy resolution (ΔE) of the analyser. ΔE can be calculated as follows [91]:

$$\Delta E = E_{pass}(\frac{d}{2R_o} + \alpha^2) \tag{3.15}$$

The parameter α depends on the entrance lens settings.

The VG Scientific 100AX has an entrance and exit slit width of 4 mm and an outer and inner radius of 185 mm and 115 mm respectively. The length and diameter of the analyser nose are 200 mm and 59 mm, respectively, and the entrance diameter of the nose is 170 mm.

The electrons that pass through the analyser are amplified by the Channeltron. When an electron hits the walls of the Channeltron, secondary electrons are generated and are accelerated by a field. These electrons interact with the surface of the Channeltron multiple times to generate up to 10^8 electrons per incoming electron. These electrons are detected by a pre-amplifier. The output of the Channeltron is a current proportional to but many times larger than the current of incoming electrons. To take a

SPELS spectrum, the accelerating voltage of the Channeltron was generally set to 2.35 kV, which was the optimised value in our system.

3.2.4 Field Emission Measurement

The field emission current properties of tips were measured before taking SPELS spectra. The field emission current was measured using a Keithley 485 picoammeter which was connected to the sample via a feedthrough on the STM. The tip - sample distance generally used was to ~ 600 - 700 nm. A negative bias was applied to the tip and the field emission current was recorded using an RHK STM controller and software (RHK XPM Pro). The range of voltages applied for collecting SPELS spectra was 0 V to -250 V and the corresponding field emission current was measured at these potentials.

To measure the current-voltage (I-V) characteristics of the tips it was necessary to optimise several experimental parameters before a stable I-V characteristics could be obtained. A typical current profile is depicted depending on changing voltage in Figure 3.16(a). The bias voltage as a function of time is shown in Figure 3.16(b), whilst Figure 3.16(a) shows the corresponding current. The rate of voltage change is faster than the rate of current change. Therefore, a large ΔV occurs in a short time Δt. Due to this unwanted transient current, increasing the delay time can avoid this immediate jump in the field emission current. There are three time parameters that can be adjusted in the software to avoid capacitive coupling between bias and the field emission current. The first delay (t_1) is the 'spectrum delay'. The delay at each individual voltage step (t_2) is the 'pre-sample delay', and the time spent averaging at each step (t_3) is the 'sample/point'.

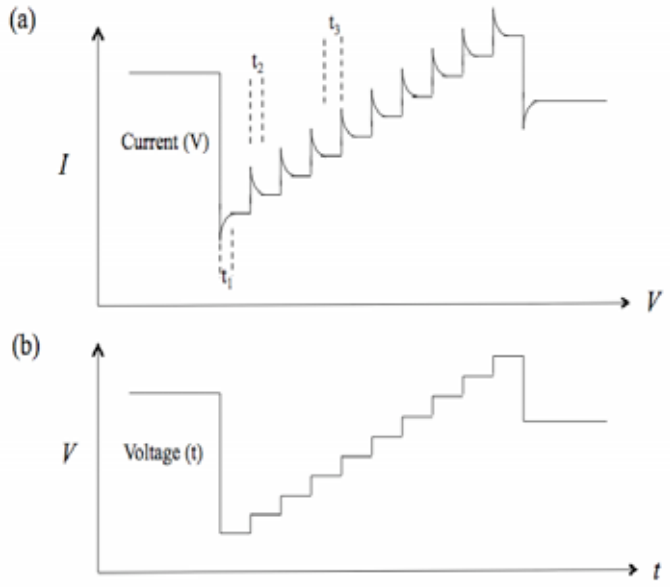

Figure 3.16: Typical (a) current profiles depend on (b) changing voltage, showing three time parameters. The first delay (t_1) is determined by the spectrum delay. The delay at each voltage step (t_2) is set using the pre-sample delay and the amount of time spent averaging the current reading at each step (t_3) is determined by the samples/point.

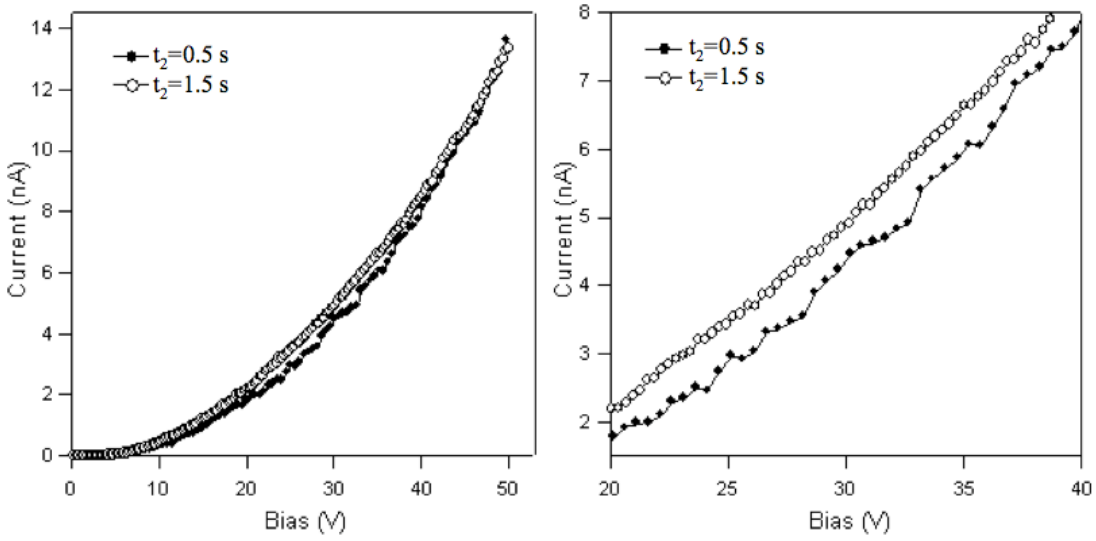

Figure 3.17: I-V characteristics of an Au coated silicon tip (left) and a magnification of the I-V curve between 20 V and 40 V (right). Pre-sample delay (t_2) of 0.5 seconds and of 1.5 seconds is shown. For t_2=1.5 seconds (which took measurements over a longer set time) the curve is more stable than for t_2=0.5 seconds.

Figure 3.17 shows an example of I-V curves with different 'pre-sample delay (t_2)' times. The field emission current was measured using an Au coated silicon tip. The values of the 'sample/point (t_3)' and 'spectrum delay (t_1)' were set to 25 points and 1 second in both cases whilst the pre-sample delay (t_2) was set to either 0.5 seconds or 1.5 seconds. With t_2 set at 0.5 seconds, the current appears to be noisy and unstable, but for t_2 set at 1.5 seconds the I-V curve appears for more stable. Therefore, increasing the setup rate can reduce the noise.

3.2.5 Operating the SPELS

Before operating the SPELS, the wobble stick was fully retracted and the hemispherical analyser was moved close to the tip and sample (40 mm distance). The tip was approached to the sample in STM mode so that the tip is close to the sample, within the tunnelling region. The tip was then fully retracted using SPM mode which is located the tip above vacuum level. During this action the z-piezo voltage was recorded to make it possible to calibrate the working distances between the tip and sample. For SPELS the working distance between tip and sample was set to several hundred nanometres. Negative bias was applied to generate a field emission current from the tip. The field emission current was measured by using the picoammeter. The field emitted electrons hit the sample and backscattered electrons were detected by the hemispherical analyser. In order to obtain good quality SPELS spectra it was necessary to optimise various aspects of the system as described below.

Normalized SPELS Spectrum by Field Emission Current

The field emission current is used as an electron source in SPELS. It is generally stable with small fluctuations but sometimes it changes abruptly, as shown in Figure 3.18(c).

Figure 3.18 shows an example of SPELS spectra of graphite with a normalized by the field emission current (b) and without a normalized by the field emission current (a). The SPELS spectrum was taken using a tungsten tip and at a tip bias voltage of -90 V, field emission current of ~9 μA, and tip-sample distance of 615 nm. The spectrum was taken with an energy interval of 0.1 eV and a dwell time of 200 ms. In Figure 3.18(c), the field emission shows a discontinuity between 30 eV and 40 eV. This was caused either by field emission properties of the tip or by noise from outside.

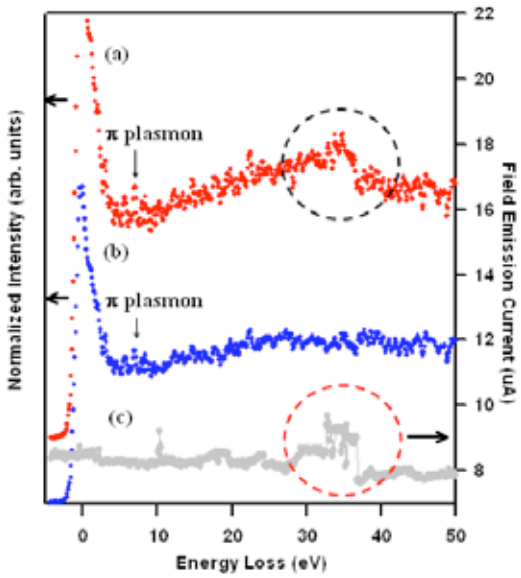

Figure 3.18: An example of SPELS spectra and field emission current. (a) SPELS spectra of graphite before normalization by field emission current and (b) after normalization by field emission; (c) field emission current. A tungsten tip was used to take the spectrum and the tip bias voltage and tip-sample distance used were -90 V and 615 nm respectively.

The SPELS spectrum without a normalized field emission current shows a discontinuity between 30 eV and 40 eV (Figure 3.18(a)). It is therefore necessary to normalize the SPELS spectra to the field emission current to present the appearance of specific peaks.

The Sampling Rate

One of the parameters that affects the quality of SPELS spectra is the sampling rate. The data acquisition card allowed dwell times at multiples of 100 ms. Long dwell times are generally favourable as they increase the number of counts that are accumulated at each energy step. However, the field emission can fluctuate whilst collecting data leading to a discontinuous spectrum. Therefore, an average dwell time of 200 ms was chosen in this study.

The Averaging Spectra

If the count rate of the spectra is too low, energy loss features cannot be clearly detected. In particular, plasmon features are usually very low in intensity compared with the elastic or secondary electron energy loss features. The averaging of spectra is one of the solutions used to obtain the energy loss spectra clearly. Figure 3.19 shows a spectrum consisting of ten averages (black line) compared to a single scan spectrum of graphite (grey dots). These data were taken using an Au cathode co-axial silicon tip with a tip bias voltage of -250 V, field emission current of ~13 μA, and distance between tip and sample of 220 nm. The spectrum was taken ten times with the same parameters. The signal-to-noise from the average spectrum is 6 times less than that from a single scan spectrum, and the weak plasmon energy loss feature can be seen clearly only in the averaged spectrum, see Figure 3.19. In this study, averaged SPELS spectra are presented.

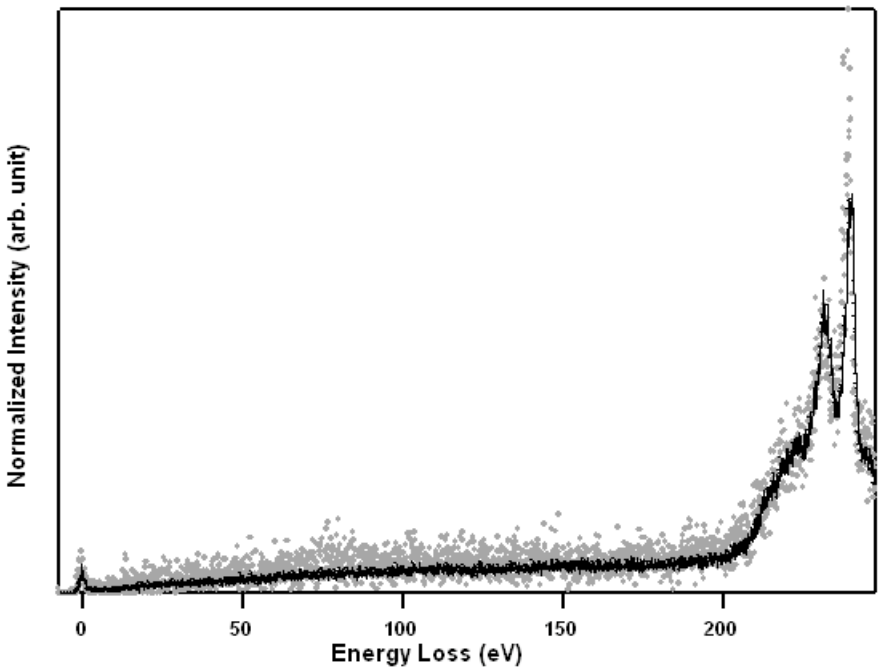

Figure 3.19: SPELS spectra of graphite using Au cathode co-axial silicon tip. The grey dots and black line represent a single scan and the average of 10 scans, respectively. Spectra are taken with a tip bias voltage of -250 V, a field emission current of ~13 μA, and a tip-sample distance of 220 nm.

Chapter Four

Microfabrication of Silicon Tips for SPM

In this chapter the microfabrication of silicon tips for SPM is reported. First, new fabrication processes needed to make a higher silicon tip and a mesa structure are presented. A batch process to simultaneously produce multiple silicon tips, over 100 μm in height, using EBL and dry etching techniques was successfully developed. The second section describes the silicon field emitters with Au coated cathodes fabricated for SPELS. A multilayer Si/Au/HfO_2/Au structure was created and the outer Au and HfO_2 layers were stripped successfully from the apex of the tip. The outer Au layer is used as a ground shield and the inner Au layer is used as the field emitter in SPELS. Finally the fabrication of tips for SPEAR is reported. These consist of Si/SiO_2/Au/SiO_2/Au layers, which together are designed to function as a retarding field electron analyser. The silicon tip, the inner Au layer and the outer Au layer are designed to be used respectively as the electron collector, retarding field element and ground shield.

4.1 Microfabrication of Silicon Tips for STM

Microfabrication of silicon tips has applications in several fields, including FEDs, AFM and STM as discussed in Chapter Two. The dimensions of a microfabricated silicon tip can be finely controlled using reproducible microfabrication processes. Silicon is also an attractive material because of its good mechanical properties, extreme flatness and well-established processes for metallization. This section presents an investigation of silicon tips fabricated using EBL, RIE, ECR and DRIE and their application to STM.

4.1.1 Formation of Silicon Tips

The production of silicon tips depends on the well-established method of isotropic etching of silicon in RIE. RIE is a lateral sideways etch and good etch selectivity between etch mask and silicon substrate. Figure 4.1 shows schematically the process of silicon tip formation and corresponding SEM images of the fabricated parts, taken at various stages of the RIE process.

In order to fabricate a silicon tip, negative tone electron beam resist (SAL 601-SR7 (Rohm and Hass)) was spin coated onto the wafer to a thickness of 1.5 μm. A post application bake of 90^{o}C for 60 seconds was applied to remove excess solvent. An array of 6 μm diameter dots was written in the resist using an electron beam at 30 kV at a dose of a 50 μC/cm^2. A post exposure bake of 115^{o}C for 60 seconds was applied before development in MF322 (Rohm and Hass) developer. These electron beam resist patterns were used as etch masks in order to fabricate the tips. The patterned resist was etched using SF_6 gas with a RIE plasma process (Figure 4.1(a)-(c)). Optimisation of the etching parameters, such as the SF_6 flow, the RF power, the RF pressure and etching time were required to fabricate a sharp tip. The RF power applied was 125 W. The etchant flow

rate was 60 sccm and the etch was performed at room temperature and at a pressure of 50 mTorr. Under these conditions the silicon etch rate was 0.62 μm/minute and the etch duration was 10 minutes.

For SPM the most important feature of the tip is its sharpness. Figure 4.1(a) and (b) show the development of the tip shape due to the isotropic nature of the etch. In Figure 4.1(b), it can be seen that some resist still sits on the apex of the tip, and it is important that the etch duration is long enough to fully remove this resist, as seen in Figure 4.1(c) where it can be seen that the resist cap has fallen to the side. The sharpest tips were obtained at this point and further etching lead to tip blunting. Subsequently the silicon wafer was cleaned with a stream of dry nitrogen gas to remove loss resist fragments. A tip of height 4.8 μm and apex radius of ~ 15 nm is shown in Figure 4.1(d).

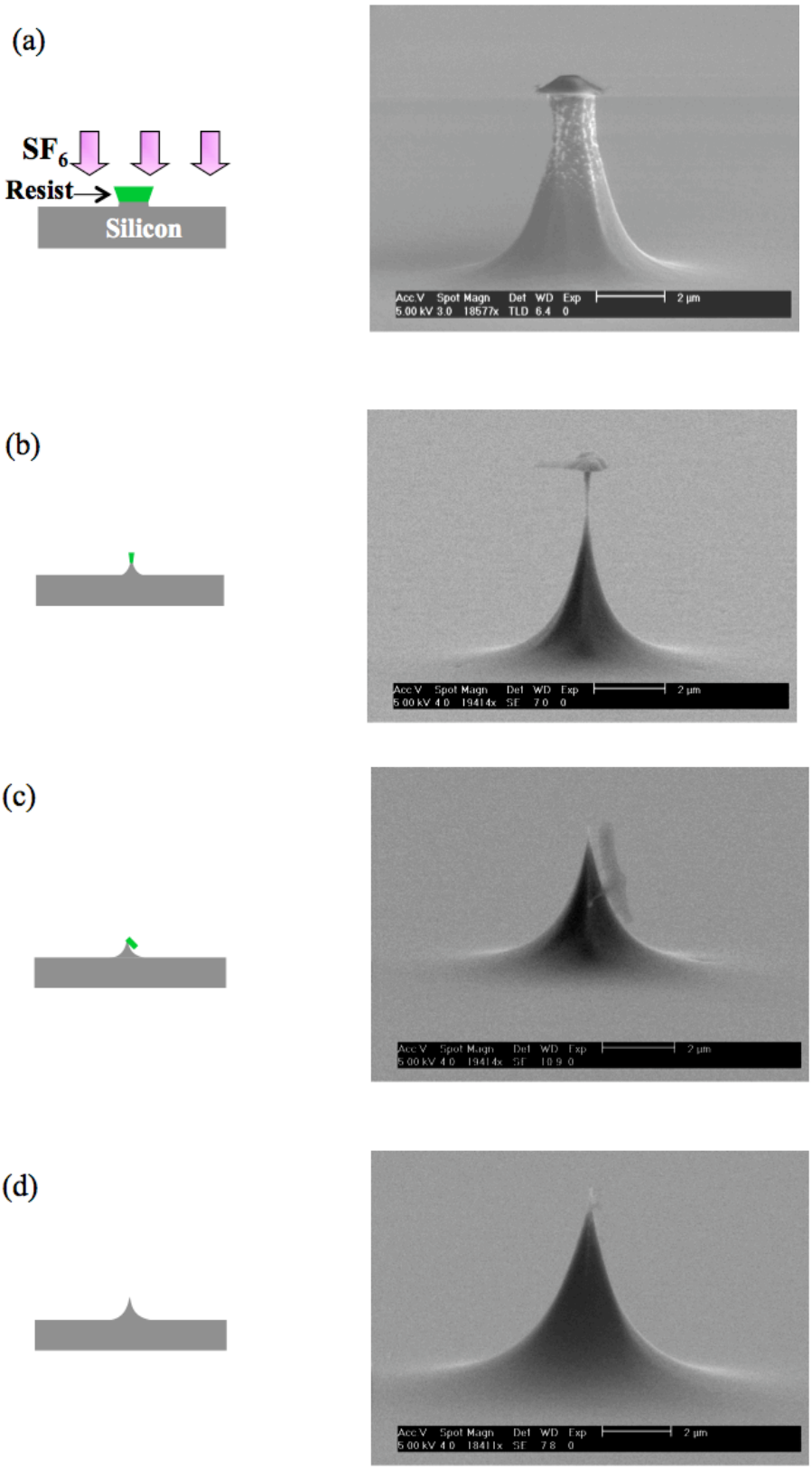

Figure 4.1: Schematic of the silicon tip formation process and the corresponding SEM images, (a) reactive ion etching, (b) under-etched silicon tip, (c) optimum etched silicon tip and (d) completed silicon tip.

4.1.2 Tip Sharpening

The silicon tips were further sharpened using a thermal oxidation/oxide stripping technique. It is possible with this method to fabricate the silicon tip with less than 1 nm radius [92]. The silicon tips were thermally oxidized at 1000^{o}C under O_2 atmosphere and the oxide layer was then removed using HF.

Oxidation occurs at the Si-SiO_2 interface. Oxygen diffuses through the presenting native SiO_2 layer (or previously formed oxide) and reacts with the silicon at the interface. Figure 4.2 shows SEM images of a silicon tip (a) before and (b) after tip sharpening.

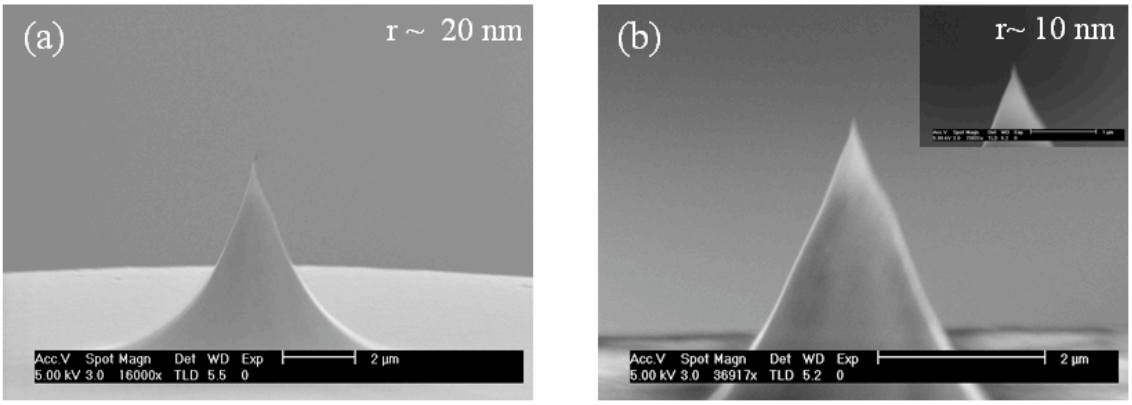

Figure 4.2: SEM images of the silicon tips, (a) before tip sharpening and (b) after tip sharpening. Insert shows the magnification SEM image of the tip apex. The apex radius of the tip was ~ 20 nm before and ~10 nm after tip sharpening.

A tip with a radius of 20 nm before tip sharpening is shown in Figure 4.2(a). After tip sharpening the tip radius was 10 nm as shown in Figure 4.2(b).

4.1.3 Mesa Structure of Silicon Tips

Silicon tips were fabricated on a planar silicon substrate as described in the previous section. Because the height of the tip was small compare to the dimensions of the substrate. The substrate edge is likely to touch the sample during SPM as shown in Figure 4.3(a) unless very strict control of the angle between the sample and the tip substrate could be exercised. In order to reduce the requirement for angular alignment whilst also presenting the problem on the edge of the tip substrate coming with contact with the sample being imaged, the tip was raised above the level of the wafer on a mesa as mentioned by Bale *et al.* [17], as shown in Figure 4.3(b).

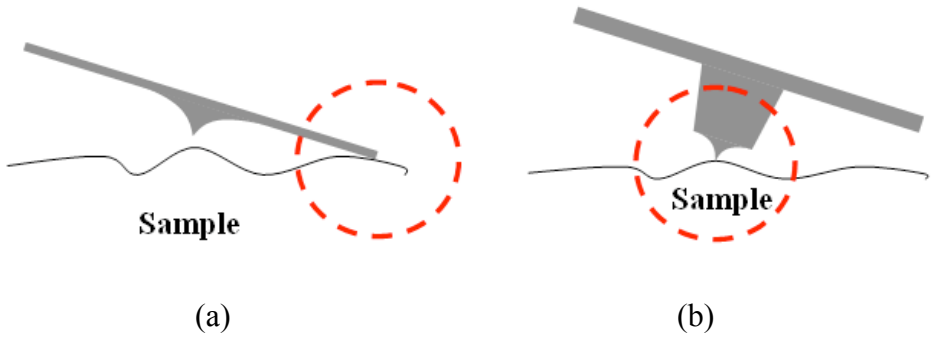

Figure 4.3: Schematic illustration of (a) the problem of angular alignment of a silicon tip on a substrate with respect to the sample and (b) the solution of placing the silicon tip on a mesa structure.

A microfabrication process of a silicon tip with a mesa structure was previously reported by Bale *et al.* [17]. Photolithography was used to place a tip onto a mesa structure following the methodology. EBL can, however, be patterned with a higher resolution than photolithography and be aligned more accurately without any mask. Therefore EBL was used in this study. Here the tip was prepared first, and the mesa structure was etched subsequently, as shown in Figure 4.4.

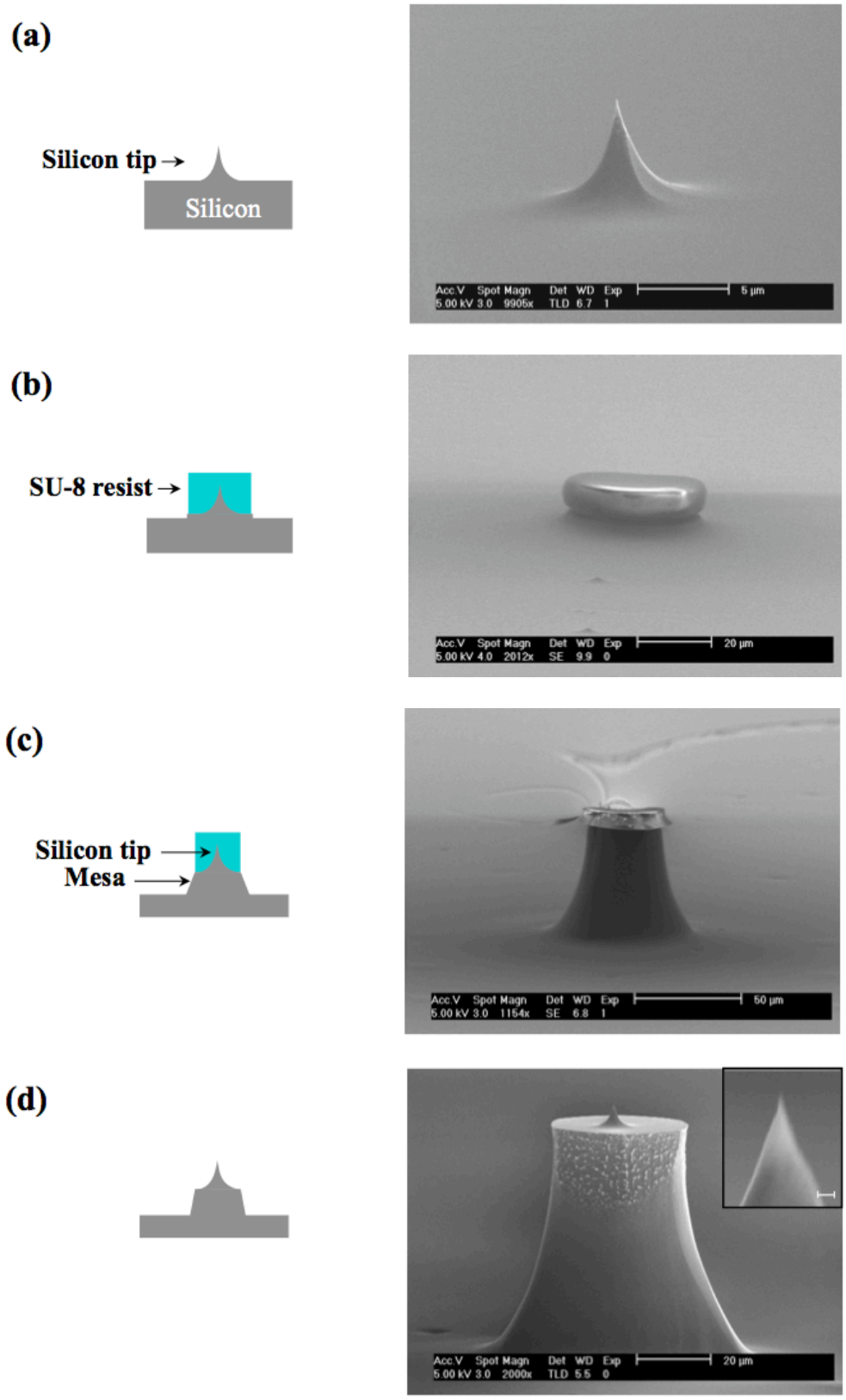

Figure 4.4: Schematic and SEM images of mesa production for a microfabricated silicon tip. (a) Silicon tip, (b) resist protected silicon tip, (c) etching the mesa (d) the final structure showing that the tip is unaffected (apex inset with 200 nm scale bar).

The fabrication process starts with an array of silicon tips produced as described in Section 4.1.1. A thick film of SU-8 resist was spin coated onto the substrate and circular patterns were written over the silicon tips. For a successful process the resist thickness needed to be significantly greater than the height of the silicon tip, in order to fully protect it during the ECR etching process. Figure 4.4 also shows SEM images recorded during the fabrication of the mesa. Figure 4.4(a) and (b) show silicon tip and a silicon tip of ~5 μm in height covered with a protective resist mask respectively. SEM image in Figure 4.4(b) was taken after a protective resist mask was etched ~ 5 μm in height. Figure 4.4(c) shows the intermediate mesa structure obtained under ECR etching with a microwave power of 250 W, RF power of 20 W and DC bias of 114 V. The etchant gas was SF_6 with a flow rate of 14 sccm at a pressure of 1 mTorr. An etching rate of 260 nm/minute was established under these conditions. The SU-8 was also etched and the initial SU-8 resist film thickness of 27 μm was reduced to 8.3 μm after an etch duration of 190 minutes. At that point, the mesa height was 50 μm. The structure of the mesa was found to be strongly dependent on the SF_6 flow rate. At slower flow rates the etch is more anisotropic and therefore higher mesa structures could be fabricated. In order to protect the tip it was necessary that, after the completion of the ECR etch, significant resist remained. The remaining resist was removed by dipping into '1165' remover solution (Rohm and Hass). The silicon tip was then further sharpened by thermal oxidation and stripping as before. Figure 4.4(d) shows an SEM image of such a mesa structure with a height of 70 μm. The inset of Figure 4.4(d) shows a magnified SEM image of the apex, which has a radius of curvature of 10 nm. Due to the rate at which the resist etches, and the electron penetration depth limitations on the maximum thickness of the resist it is not possible to produce mesa structures significantly higher than 70 μm via this processes. An electron beam is scattered on a

thick resist as discussed in Chapter Three so the exposure pattern is bigger size than the designed pattern. The bigger size pattern can be affected the alignment of the mask onto the silicon tip. Additionally, thicker SU-8 resist is difficult to remove without damaging the apex of the silicon tip. It is also difficult to know whether the silicon tip is damaged or not until the fabrication processes are finished. For these reasons, another fabrication process is required.

Due to the need to make wire bonded electrical connections to the multilayered structure from the front of the chip, the silicon tip has to be much higher than height of the wire. So 70 μm high mesa provide insufficient structure (see for instance Figure 4.22). Therefore a new process was developed for this project. In the revised method the mesa structure was fabricated first and the silicon tip was then produced on the mesa structure. The fabrication of the silicon tip can be recorded during etching processes as shown in Figure 4.5.

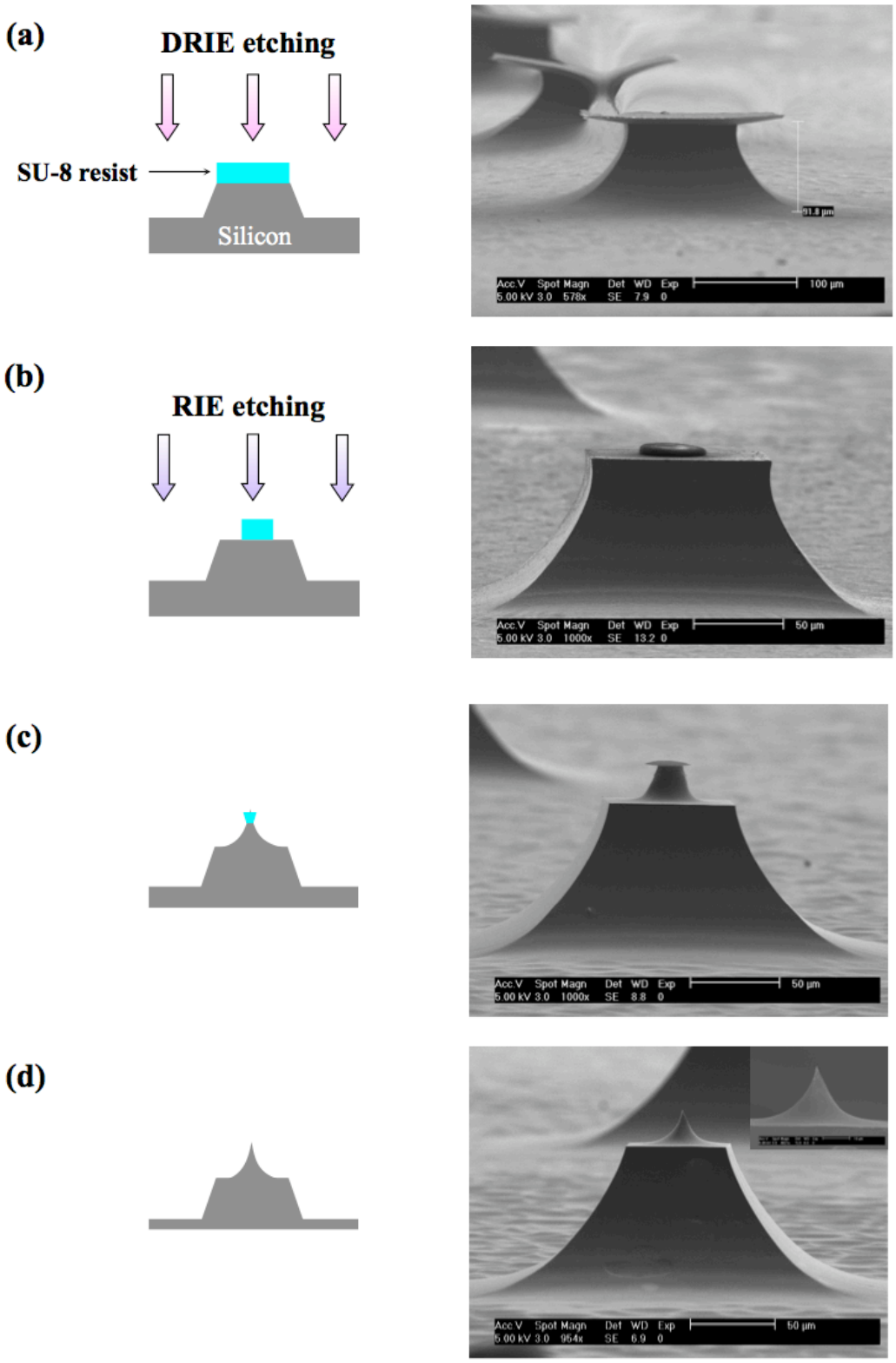

Figure 4.5: Schematic and SEM images of the modified microfabrication processes. (a) Electron beam patterned SU-8 lithography and deep reactive ion etching to form the mesa, (b) circular resist pattern on a mesa structure and reactive ion etching (c) under-etched silicon tip on the mesa structures and (d) completed silicon tip, inset the apex (radius ~ 20 nm).

A thick resist layer to protect the silicon tip is not necessary during fabrication of the mesa via this method, allowing more of the resist mask to be used during mesa fabrication and easing removal of resist after processing. Furthermore, as a protection layer, of limited thickness was no longer required for mesa production the silicon tip height could be increased (>50 μm in height). A schematic of the fabrication process and the corresponding SEM images are shown in Figure 4.5. A 16 μm thick SU-8 resist film was spin coated onto a silicon substrate. A 250 × 250 μm square pattern was written by EBL. The patterned SU-8 resist was etched under DRIE process with a 100 sccm of C_4F_8, 130 sccm of SF_6, 13 sccm of O_2 and RF power of 600 W. An etching rate of 2 μm/minute was achieved under these conditions. The etch rate of DRIE is 10 times faster than that of our ECR process. The resist was also etched during DRIE process so that the initial SU-8 resist film thickness of 16 μm was reduced to 4.6 μm after an etch duration of 45 minutes. Figure 4.5(a) is a SEM image of the resist on a mesa structure, showing a mesa structure of 92 μm height; (the SEM image is distorted due to charging of the non conductive resist). The SU-8 resist was removed using '1165' remover solution and the substrate was then cleaned after acetone to remove organic contamination. Next a new resist layer was spin coated on the substrate. The positions of the mesa structures were carefully mapped with respect to the alignment points at the edge of the wafer. A large quantity of SU-8 resist was then deposited on the substrate and spun at a 100 rpm for 10 seconds follow by a second step at 900 rpm for 120 seconds. Whilst the thickness of the SU-8 layer after spin coating was less then the height of the mesa, surface tension during spin coating ensured that the top of the mesa were well coated with resist.

A 37 μm circular pattern was written in the resist on top of the mesa structure aligned using the map created prior to coating, as shown in Figures 4.5(b). The substrate was etched with RIE to make the tip, showing an SEM image of the top on the mesa partway through RIE etch, where RF power was 125 W, pressure was 50 mTorr and SF_6 etchant flow rate was 60 sccm. An etching rate of 480 nm/minute was achieved under these conditions. The RIE was performed without any additional mask to protect the mesa itself and as a result, the mesa structure was further etched. As the top of the mesa was removed at the same rate as the base level silicon, the height of the mesa was not significantly altered. The isotropic nature of the RIE did reduce the slope of the sidewalls, which proved beneficial during subsequent metallization. After completion of RIE, the remaining resist was removed. Figure 4.5(d) shows an image of a silicon tip on a mesa structure with a high magnification image of the apex inset. The completed silicon tip was 22 μm in height on a mesa structure with a height of 100 μm. The apex had a radius of curvature of ~20 nm which could be improved by oxide stripping. This fabrication method can also be used to batch fabricate multiple tip-on-mesa structures as shown in Figures 4.6(a) and 4.6(b). Silicon tips were generally fabricated in 4 × 4 arrays on a silicon substrate 1.5 × 1.5 cm in size but SEM image of tip arrays is only shown in 2 × 4 arrays because of limited SEM magnification. Figure 4.6(b) is the lowest magnification in our system. The individual tip were the separated either by decreasing the chip by hand, or with a precision wafer dicer.

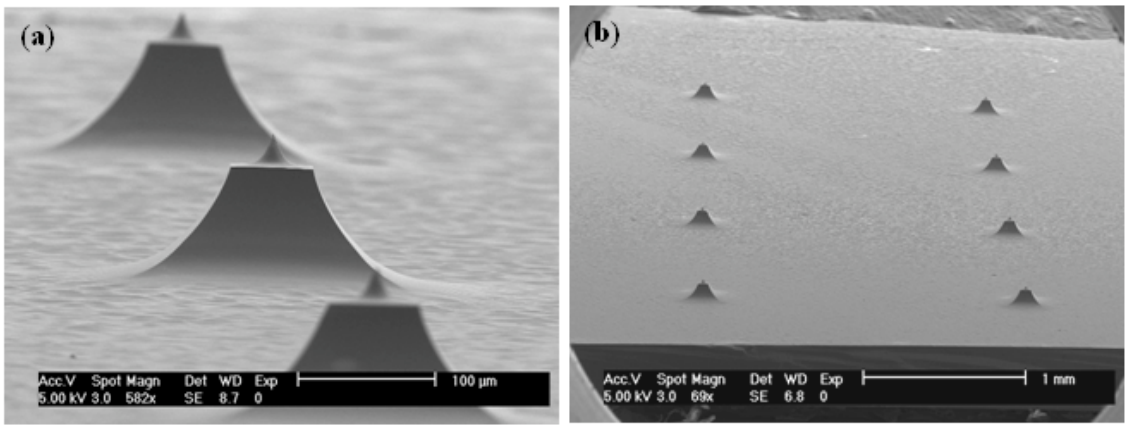

Figure 4.6: Images of (a) silicon tips and (b) a silicon tip array. The distance between each mesa is 2 mm and 2 × 4 tip arrays were fabricated on a silicon substrate.

4.1.4 Analysis of Sloped Sidewall on a Mesa Structure

The effects of the fabrication process parameters on the shape of the mesa structures were investigated. A sloped sidewall is required to ensure electrically conducting films which are formed during the metallization process. Figure 4.7 illustrates the definition the sidewall angle θ used here, which could be calculated using the mesa with (measured by SEM) and the mesa height (calculated from the etching rate and the etch duration). The effect of the tip formation RIE step on θ is shown in Table 4.1.

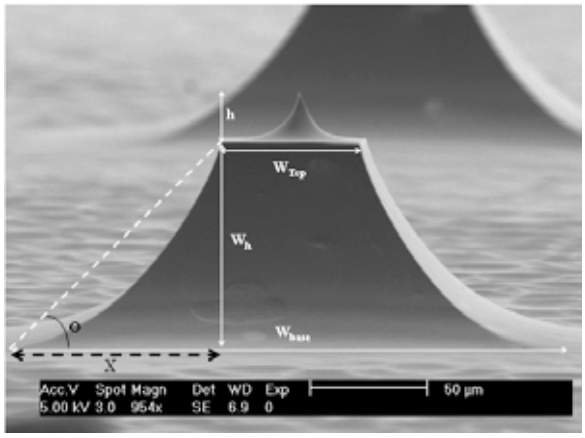

Figure 4.7: The measurements of the sidewall angle θ.

It can also be seen from Table 4.1 that the height of the mesa was not affected by RIE. The footprint (W_{base}) of the mesa was not significantly altered, but the dimensions of the top of the mesa structure (W_{top}) were reduced by almost 50%.

Table 4.1: Side angle θ of a mesa structure

RIE time	0 minute Figure 4.7(b)	39 minute Figure 4.7(c)	46 minute Figure 4.7(d)
W_{top} (μm)	102 μm	69 μm	57.7 μm
W_{base} (μm)	214 μm	230 μm	237.5 μm
W_h (μm)	91.8 μm	91.8 μm	91.8 μm
θ	**58.6**	**48.7**	**45.56**

The reduction of W_{top} is advantage on in terms of the issue of angular alignment discussed in Section 4.1.3 and illustrated in Figure 4.3(a).

4.2 Microfabricated Au Cathode Co-axial Silicon Tips for SPELS

4.2.1 Design of Au Cathode Co-axial Silicon Tips

In this section, the further development of the tip for Scanning Probe Energy Loss Spectroscopy (SPELS) is described. In SPELS, the tip is mainly used as a field emitter, although it must also be able to function as an STM probe. Its described in Section 2.5, the strong potential used in field emission can affect the trajectories of the electrons scattered from the surface. To reduce this effect a co-axial shield was fabricated on the tip.

The effect of the tip shield was simulated using an ion optics simulation program (SIMION, Idaho National Engineering and Environmental Laboratory). Cylindrical symmetry around the z-axis was used, with 200 × 200 grid lines and a grid unit of 2 nm. Figures 4.8 and 4.9 show the simulated electron trajectories and electric field lines around a normal and a shielded tip respectively. The tip bias was set to -100 V with respect to the sample ground. The apex of the tip is 15 nm and the distance between tip and sample was 100 nm. The electron trajectories from the apex of the unshielded tip are shown in Figure 4.8(a). Since the apex of the tip has the strongest electric field, electrons are emitted from the apex along the z-axis. The trajectories of backscattered electrons are shown in Figure 4.8(b). Most backscattered electrons are deflected back towards the surface, and some are completely suppressed by the strong electric field around the tip.

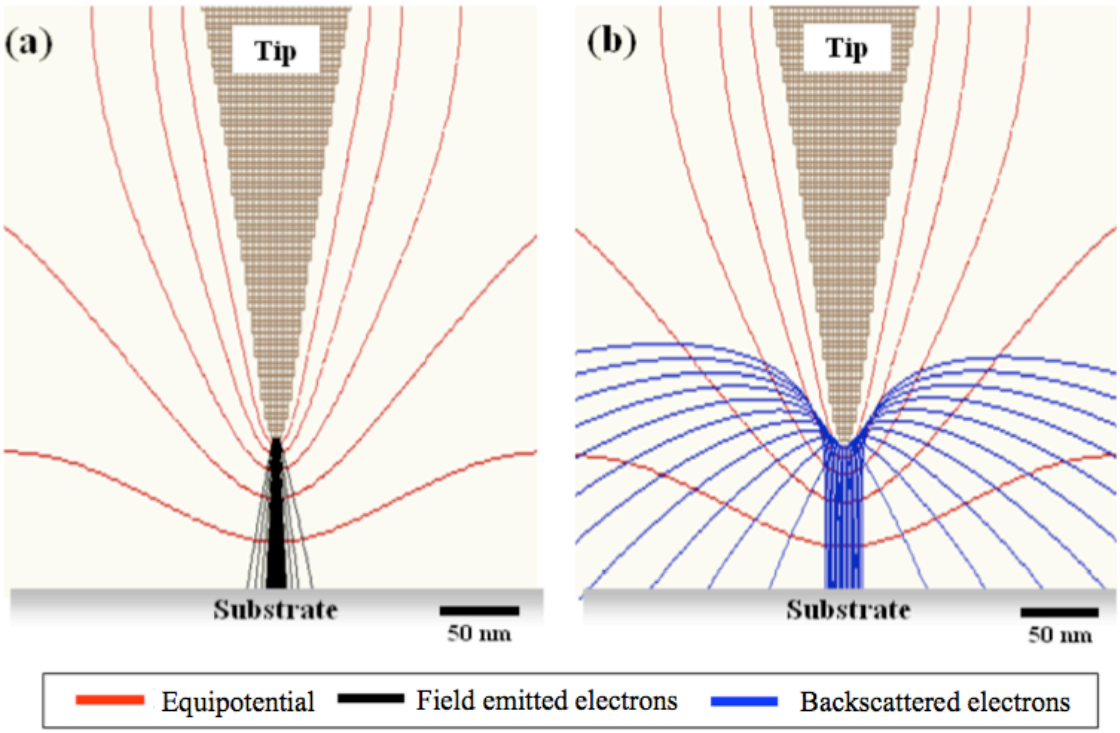

Figure 4.8: Simulated electron trajectories, (a) electrons emitted from a tip and (b) backscattered electrons from surface. Tip bias is -100 V, distance between tip and sample is ~ 100 nm, apex radius of the tip is ~ 15 nm.

Figure 4.9 shows the simulation when the electric field has been screened. The electron trajectories from the apex of the co-axial tip are shown in Figure 4.9(a), and are similar to the case in Figure 4.8(a).

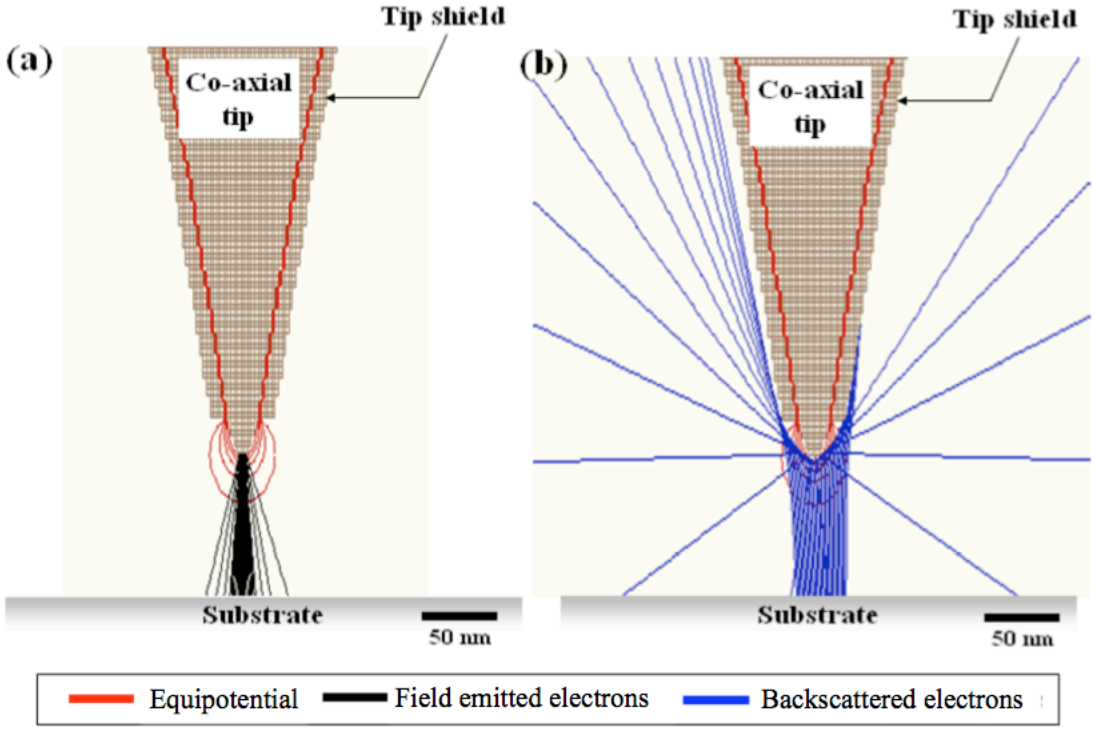

Figure 4.9: Simulated electron trajectories, (a) electrons emitted from a co-axial tip and (b) backscattered electrons from surface. Co-axial tip bias is -100 V, distance tip to sample is ~ 100 nm and apex radius of the tip is ~ 15 nm.

The backscattered electrons shown in Figure 4.9(b) were not deflected by an electric field and emerge over a much wider range of angles. The kinetic energy of the backscattered electrons is the same, 95.5 eV ($E_{kinetic}$ = incident energy (100 eV) – work function of graphite (4.5 eV)), and most backscattered electrons are escaping the tip-surface junction. Therefore, the co-axial tip would be expected to enable angle resolved measurements and also to work at much smaller tip-surface distance, allowing higher spatial resolution.

Field Emitting Layer

Initially, for simplicity, a two-layer tip was fabricated, comprising a thermal oxide layer on the silicon tip with a 20 nm Au outer layer. A 5 nm Cr adhesion layer was applied prior to Au coating. The Au and SiO_2 were removed at the apex as described in Section 4.2.2 (Figure 4.12), leaving the hydrogen terminated inner silicon tip exposed. The completed hydrogen terminated co-axial silicon tip is shown in Figure 4.10(a). The Au and SiO_2 etched layer are etched back from the apex by 2 μm, Figure 4.10(b). Figure 4.10(c) shows a cross sectional SEM image of a co-axial silicon tip. The layered structure of the co-axial tip can clearly be observed. However, even under UHV conditions, the silicon oxidized leading to small and unstable field emission currents.

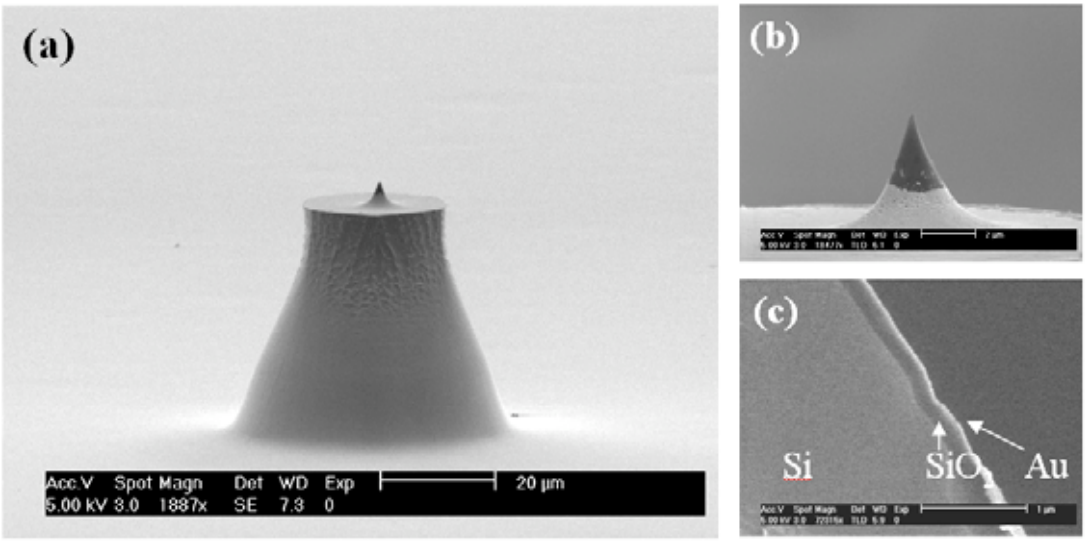

Figure 4.10: SEM images of the co-axial tip with hydrogen terminated silicon inner surface. (a) The structure consists of a 43 μm high mesa structure with a tip of 4.7 μm height, (b) magnification of the apex, showing how the outer layer are removed, and (c) cross sectional image of the co-axial silicon tip, showing the layers.

To stabilise the properties of the tip an inner Au layer was applied directly to the silicon tip (with Cr adhesion layer) prior to the dielectric, as shown in Figure 4.11. Even though Au is not ideal for field emission it is easy to prepare a thin layer on the tip

and it has excellent chemical stability, which is necessary for stable field emission. For SPELS a stable field emission current is highly advantages for collecting spectra.

Insulating Layer

In order to isolate the grounded outer layer from the biased inner layer, an insulating layer was placed between them. The capacitance across this insulating layer was extremely high. Therefore, the insulating layer must be uniform and of very good quality, to prevent a breakdown and subsequent shorting of the conductive layers.

SiO_2 is widely used as an insulating material in the semiconductor industry. SiO_2 is easy to grow thermally on silicon substrate so the SiO_2 layer has an excellent interface with the silicon, and thus forms a very good quality of an insulating layer. Figure 4.10(c) shows the uniformity of an insulating layer produced this way. However, in the modified design with an Au field emission layer it was no longer possible to use a thermal oxide-insulating layer. As an alternative, a sputtered SiO_2 insulating layer was prepared. However, sputtered SiO_2 is generally very rough compared to the thermally grown SiO_2, and the sputtered SiO_2 was extremely unreliable. Therefore, HfO_2, a high-*k* dielectric material frequently used in the semiconductor industry was substituted for the SiO_2.

Grounded Layer

The outer layer is grounded and acts as a tip shield. It must be stable in UHV as well as in air, form a good quality film on the HfO_2 layer and should also be easy to etch. Therefore, a Au layer was also used for the outer layer.

4.2.2 Fabrication of Au Cathode Co-axial Silicon Tips

Figure 4.11 shows the schematic of an Au cathode co-axial silicon tip for SPELS.

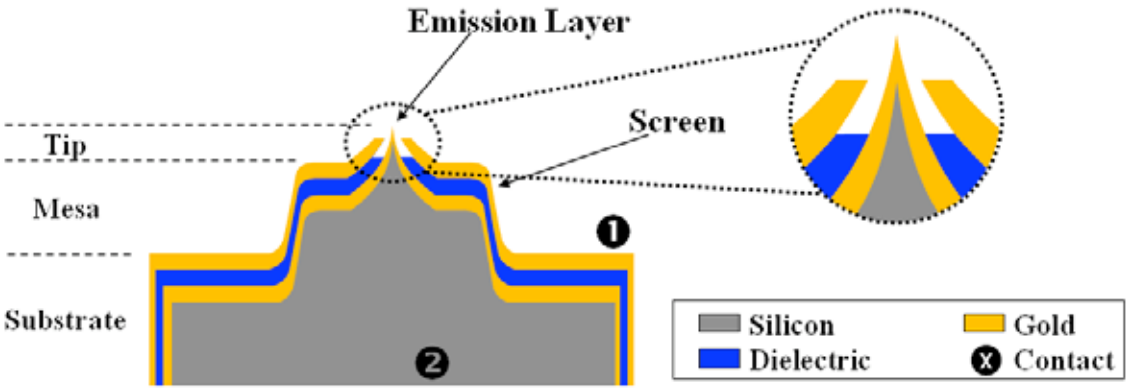

Figure 4.11: Schematic of an Au cathode co-axial silicon tip for SPELS. It consists of a Au/HfO_2/Au layers on silicon with two electrical contacts, -one to the backside and the other one to the front. The outer Au layer and HfO_2 layer are stripped from the apex.

The microfabricated Au cathode co-axial silicon tip consists of a thin sputtered Au layer on a highly doped silicon tip, coated with a sputtered hafnium dioxide (HfO_2) dielectric layer and finally an outer Au layer. Electrical contacts were made to the outer Au layer directly (labelled 1) and to the inner Au layer via the silicon substrate (labelled 2). The outer layer was grounded, and a negative bias was applied to the inner layer.

The fabrication process of the Au cathode co-axial silicon tip is shown in Figure 4.12. Prior to metallization the tip array was cut into individual tips on 2 × 2 mm substrates. It was necessary to dice the chip prior to metallization to allow metal coating of the sides for the second contact.

The natural SiO_2 layer was removed using HF, and the Au, HfO_2 and Au layers were immediately sputtered onto the chip. The inner, field emission layer was 20 nm thick, whilst the insulating HfO_2 and the thicker Au ground layers where both 60 nm thick. A 5 nm adhesion layer of chromium was deposited between the silicon and the

first Au layer, and between each of the subsequent layers (Figure 4.12 (b)). The Au and HfO_2 layers were also sputtered on the sides of the silicon substrate. The metal coated silicon tips had to be handled very carefully to avoid breaking or damaging the apex of the tip. Since the tip substrate was very small, to prepare it for etching the apex, the substrate was mounted on a 1.5 × 1.5 cm piece of silicon using a very small amount of vacuum grease. SU-8 resist was then spin coated to achieve uniform coating of ~15 μm thickness across the tip substrate.

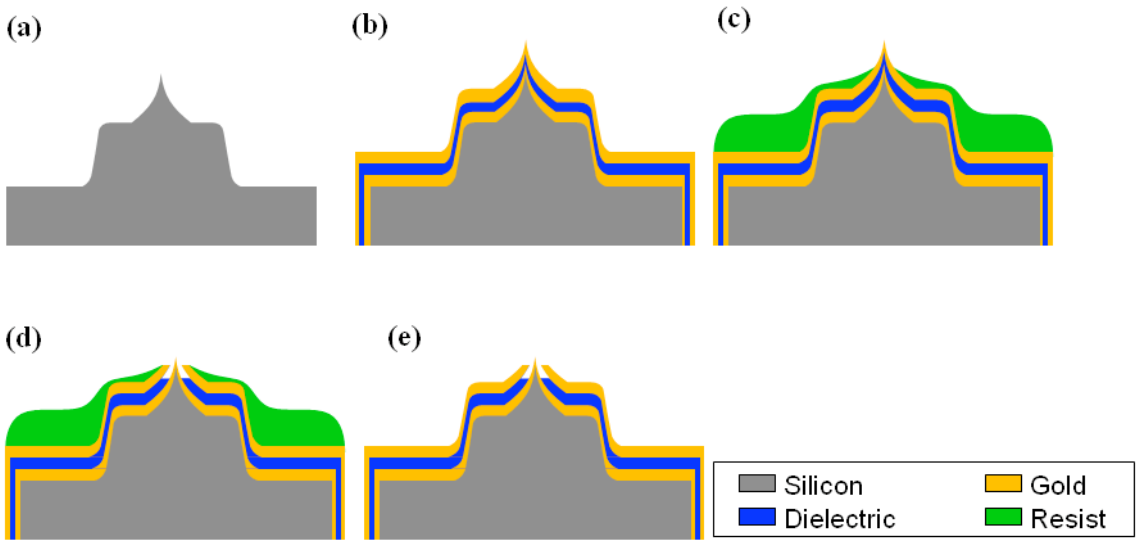

Figure 4.12: Microfabrication processes of Au cathode co-axial silicon tip, (a) silicon tip, (b) sputter coating, (c) resist coating as a mask, (d) etching the outer Au and HfO_2 and (e) completed co-axial tip.

Due to surface tension, the resist coated the tips, over the apex, as well as the substrate. However, the resist thickness at the apex was considerably lower than elsewhere. The protected substrate was then treated with a wet Au etchant, comprising a strong oxidiser, made using iodine (0.5 g) and potassium iodide (2 g) in deionised water (7 mL), mixed with an acid chromium etchant (7 mL, ETCH 18, Rohm and Hass), in a 1:1 ratio by volume. A small amount of the Au etchant was dropped onto the silicon tip.

The thin layer of resist at the apex was quickly removed by the etchant, whist sufficient of the resist remained in the other area to protect the substrate. The etchant was therefore able to etch the outer Au layer and the Cr adhesion layer, but only at the now uncovered apex. The etch duration was ~ 5 seconds after which the substrate was dipped in deionised water to remove the etchant. The HfO_2 at the apex was then removed by aqueous HF (Figure 4.12(d)). The thickness of the resist at the apex varies continuously, being thinnest at the tip and becoming thicker further down. Therefore the metal free area of the apex could be controlled by etch duration. The etch rate of HfO_2 is quite slow, but it is critical that the HfO_2 is fully removed to prevent charging. Fortunately the HF etch for HfO_2 does not affect the Au layers, and thus the HfO_2 can be over etched for safety. A etch duration of 1 minute was used. Finally the remaining resist was removed using acetone, Figure 4.12(e).

To confirm HfO_2 etch, Energy-dispersive X-ray spectroscopy (EDX) spectra were obtained before and after etching the HfO_2 layer as shown in Figure 4.13.

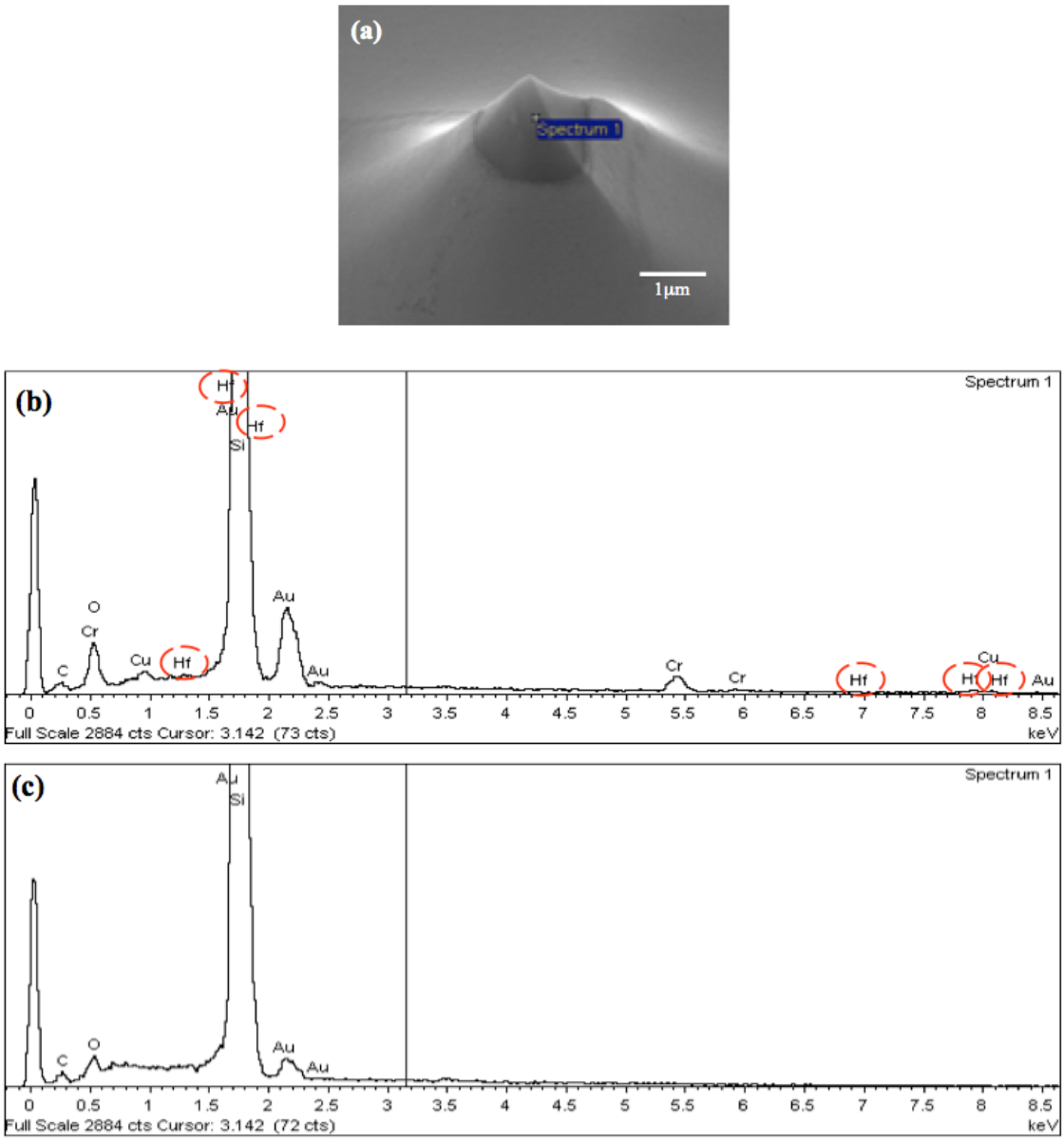

Figure 4.13: EDX analysis of a co-axial silicon tip, (a) SEM image of the tip, (b) EDX spectra before etching the HfO_2 layer and, (c) after etching the HfO_2 layer.

Figure 4.13(a) shows a SEM image of an Au cathode co-axial silicon tip; the EDX spectrum was taken at the opened area of the tip. Figure 4.13(b) show the EDX spectrum before etching the HfO_2 layer. Hafnium (Hf) peaks can be seen clearly. After the HfO_2 layer of the co-axial silicon tip, the Hf signal disappeared, Figure 4.13(c).

The completed microfabricated Au cathode co-axial silicon tip is shown in Figure 4.14(a) with the apex inset. The structure is Si/Au/HfO_2/Au and consists of a

mesa structure 76 μm high with a tip height of 23.3 μm. The outer Au and HfO_2 layers have been removed from the top 12.5 μm of the apex. Figure 4.14(b) shows an SEM image of a cross section of the co-axial silicon tip.

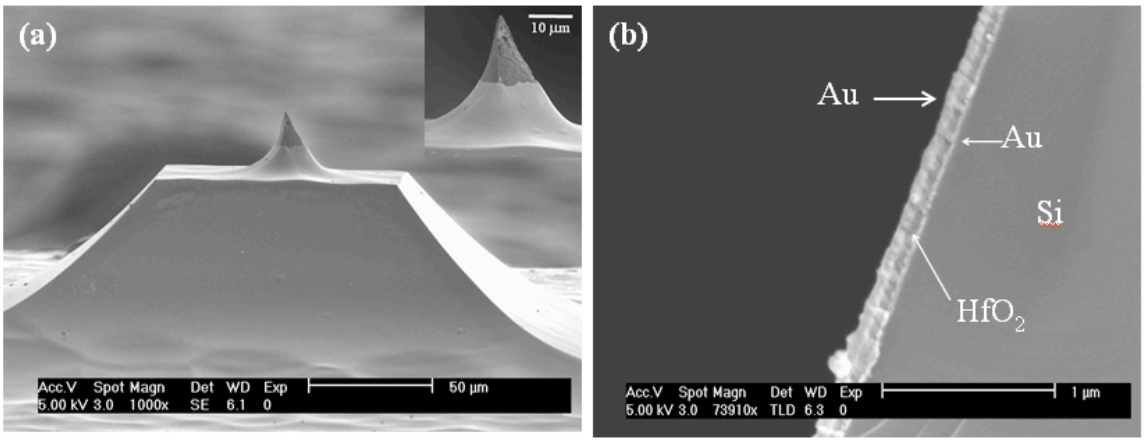

Figure 4.14: (a) SEM image of a microfabricated Au cathode co-axial silicon tip on a mesa with a Si/Au/HfO_2/Au multilayered structure. Inset is a magnified image of the tip shown the outer Au and HfO_2 layers stripped from the apex. (b) SEM image of a cross section of a co-axial silicon tip show the multilayer.

The silicon, the inner Au layer (20 nm), the HfO_2 layer (60 nm) and the outer Au layer (60 nm) can be seen clearly. The application of this Au cathode co-axial silicon tip to SPELS is in Chapter Five.

4.2.3 Design of Au Cathode Co-axial Silicon Tip Holder

The tip holder has been designed in order to load a co-axial silicon tip into a UHV Omicron STM-1. The tip holder is one of the most important parts for SPELS because it can strongly affect the electron trajectories between the sample and the hemispherical analyser. The modified co-axial tip silicon holder is shown in Figure 4.15.

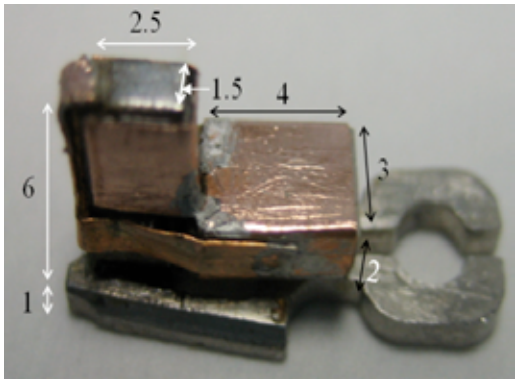

Figure 4.15: Photograph of a co-axial silicon tip holder used in SPELS. The numbers indicate dimensions in mm.

Due to the constraints of the STM possible modifications of the tip holder are very limited. The tip chip is 2 mm × 2 mm, and 500 μm thickness including the height of the tip. The silicon tip has to be elevated so that the distance from the base of the holder to the top of the tip is ~ 7.5 mm. A stainless steel rectangular cube with dimensions 6 mm × 1.5 mm × 2.5 mm was therefore attached to the tip holder, as shown in Figure 4.16, conducting UHV glue (EpoTek 377, Promatech Ltd.). The body of the tip holder, via the stainless steel cube, is used to apply the negative bias to the tip, and must therefore be shielded to prevent electron trajectory distortion. Ceramic insulation was therefore attached to the tip holder, and all parts were covered with copper foil which was grounded via the STM's built in tip shield, also shown in Figure 4.16.

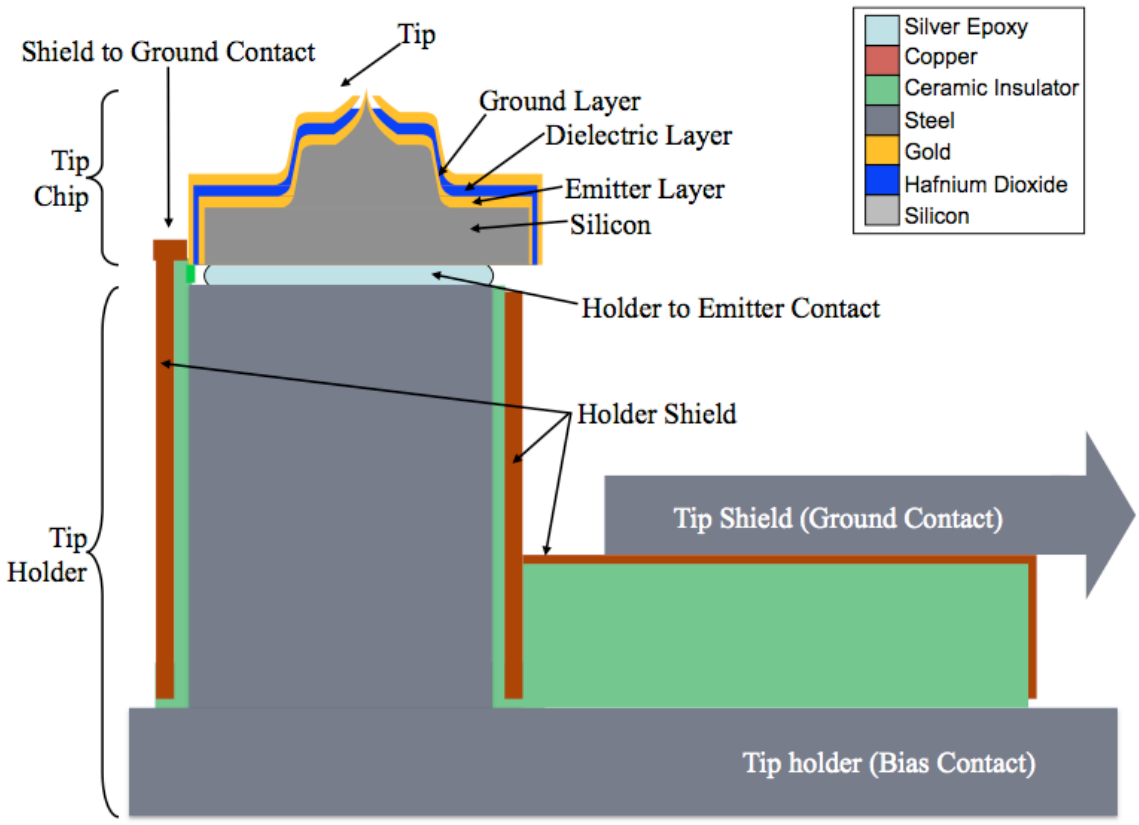

Figure 4.16: Schematic diagram of the Au cathode co-axial silicon tip with two electrical connections. The silicon tip was mounted onto the stainless steel block and the outer Au layer of the co-axial silicon tip was connected with the tip shield.

The Au cathode co-axial silicon tip was mounted onto the stainless steel block using a small amount of silver epoxy (Conductive epoxy CW2400, ITW Chemtronics) which was required curing at 150^{o}C for 20 minutes to improve the conductivity between silicon tip and tip holder. Silver epoxy was preferred over the silver paste typically used in such UHV application to ensure a good mechanical bond of the tip chip, which otherwise frequently became detached in the UHV chamber during tip transfer. The grounding of the outer layer of the co-axial tip was achieved by contacting the outer Au layer of the tip mechanical with the copper foil at the side of the tip chip as shown in Figure 4.16.

Due to out gassing of the epoxy, the assembled tip and tip holder were left for one day in the load-lock prior to transfer to the preparation chamber.

4.3 Microfabricated Multilayered Silicon Tips for SPEAR

In this section, the fabrication of silicon tips for the scanning probe electron analyser (SPEAR) described in Section 2.6 is presented.

4.3.1 Design of Multilayered Silicon Tips

The five layers are the silicon substrate, a dielectric, an inner metal layer, a second dielectric layer, and outer metal layer. The silicon substrate forms the photoelectron collector. The inner metal layer is the retarding field element which prevents electrons with energy from reaching the collector. A negative bias, V, is applied to this layer during use. The outer metal layer is grounded, generating a field free region away from the centre of the tip. The outer metal layer and the second dielectric layer are removed at the apex, so that electrons can pass through to the retarding field element without obstruction. Each metal layer and the silicon substrate are contacted with separate electrical connections, denoted 1,2 and 3 in Figure 4.17.

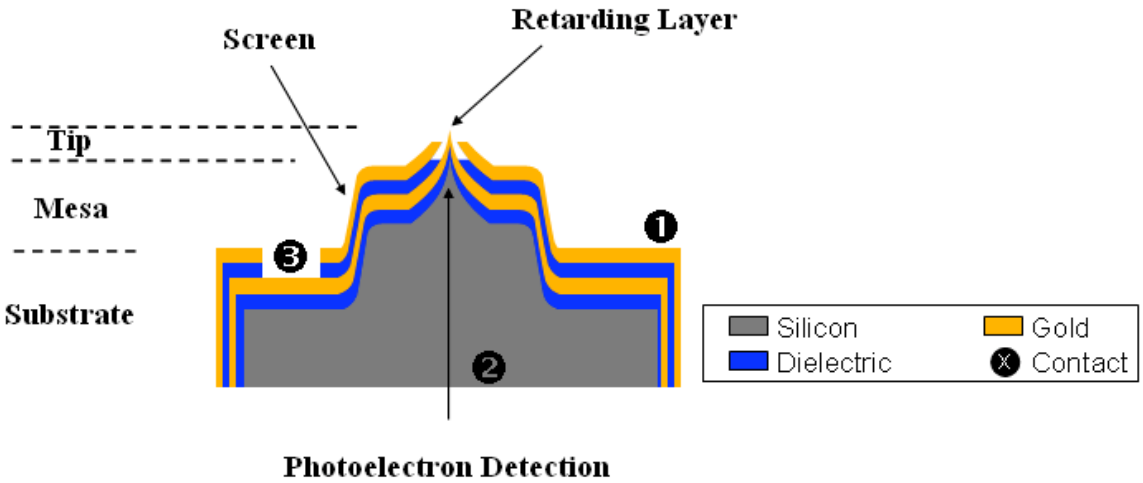

Figure 4.17: Schematic of a multilayered silicon tip for SPEAR. The tip consists of a Si/SiO_2/Au/SiO_2/Au layers. Three electrical contacts are required.

4.3.2 Fabrication of Multilayered Silicon Tips

The multilayered SPEAR tip structure is depicted schematically in Figure 4.17. The fabrication process starts with the production of a silicon tip on a mesa, fabricated as described in Section 4.1.3 (Figure 4.5). The tip radius was sharpened using thermal oxidation and HF stripping, as described in Section 4.1.2. As shown in Figure 4.18, the sharpening process has the side effect of removing contaminations.

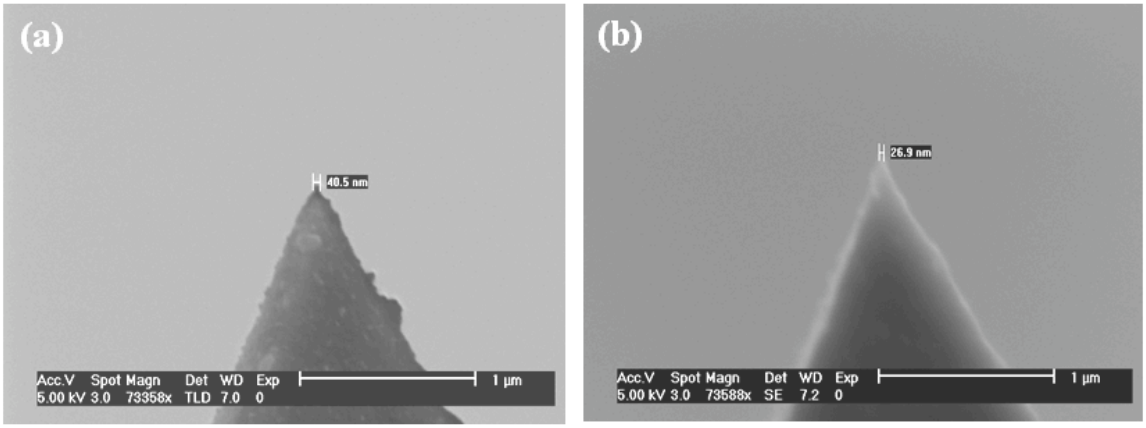

Figure 4.18: SEM images of an apex on a silicon tip, (a) thermally grown SiO_2 layer on an apex and (b) silicon tip after removing SiO_2 layer. The tip radius is sharpened from 20.3 nm to 13.5 nm.

Figure 4.18 shows (a) an apex with thermally grown SiO_2 layer and (b) a sharpened apex. Prior to sharpening the radius is 20.3 nm and some contaminants can be seen. After HF treatment the tip radius is 13.5 nm and the tip appears much cleaner as expected.

The fabrication processes of the SPEAR tip is shown in Figure 4.19. The inner SiO_2 layer was created by thermal oxidation of the silicon tip in a furnace at 1000^{o}C under O_2 for 30 minutes. This was followed by sputter deposition of a Cr adhesion layer (5 nm) and an Au layer (15 nm) (Figure 4.19(b)). The photoelectrons have to pass

through the Au layer to the silicon collector so it best as thin as possible. The thickness was measured on the plane surface so the thickness at the apex is most likely less.

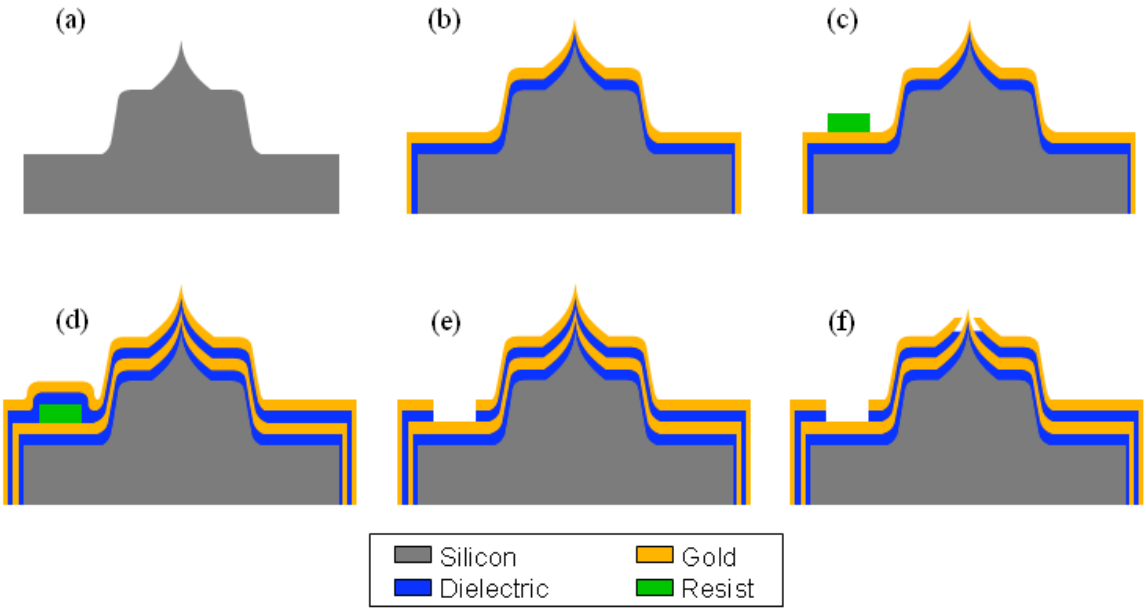

Figure 4.19: Schematic of the SPEAR tip forming processes, (a) silicon tip, (b) sputter coating, (c) third contact mask, (d) sputter coating, (e) lift off, and (f) apex opening.

In order to make electrical connections to the inner Au layer in the finished device, it was necessary to prevent subsequent layers from covering the contact point on the inner layer. SU-8 resist was spin coated over the whole substrate using a spin speed of 4000 rpm for 60 s to give a film thickness of 3 μm. A post application bake of 95°C for 120 s was applied to remove any remaining solvent on the resist. A 370 × 370 μm square pattern was written on the SU-8 resist using an electron beam at 30 kV and a dose of a 70 μC/cm^2. A post bake of 95°C for 2 minutes was applied before development SU-8 developer for 1 minutes followed by an isopropanol rinse and nitrogen drying (Figure 4.19(c)). The outer SiO_2 (275 nm) and metal layer (Cr/Au, 5 nm/50 nm) were then deposited by sputtering (Figure 4.19(d)). The second insulating layer was formed by sputtering as a thermally oxidized SiO_2 layer can only be grown on

silicon. The second insulating layer was formed from sputtered SiO_2, but other insulators, for example HfO_2 could be used.

The resist protecting layer which was allowed the inner Au layer electrically contact left off using 1165 remover solution at 150^{o}C, followed by an acetone rinse (Figure 4.26(e)). As for the SPELS tip, the outer metal and insulator layer were etched from the apex as described in Figure 4.12 (Figure 4.19(f)).

SEM images of the fabrication steps are shown in Figure 4.20. Figure 4.20(a) is a SEM image of a silicon tip with the apex inset. The tip radius, height of the tip and height of the mesa structure are 13.5 nm, 31 μm and 107 μm, respectively. Figure 4.20(b) and (c) show a five layered silicon tip with resist patterns protecting the inner metal layer electrical contact before and after removing the resist, corresponding to fabrication process step, Figure 4.19(d) and (e), respectively. The areas indicated by the white dashed squares on Figure 4.19(d) are the inner metal layer whilst other areas are the outer metal layer. A image of the completed structure is shown in Figure 4.20(d). The inset of Figure 4.20(d) shows the etched apex of the tip. The outer two layers are removed from the top 7 μm of the tip. Due to the complex series of fabrication steps the yield of working tips was not necessarily 100%, so typically several devices were made in parallel on a single substrate which was then diced into 2 × 2 mm chip after processing.

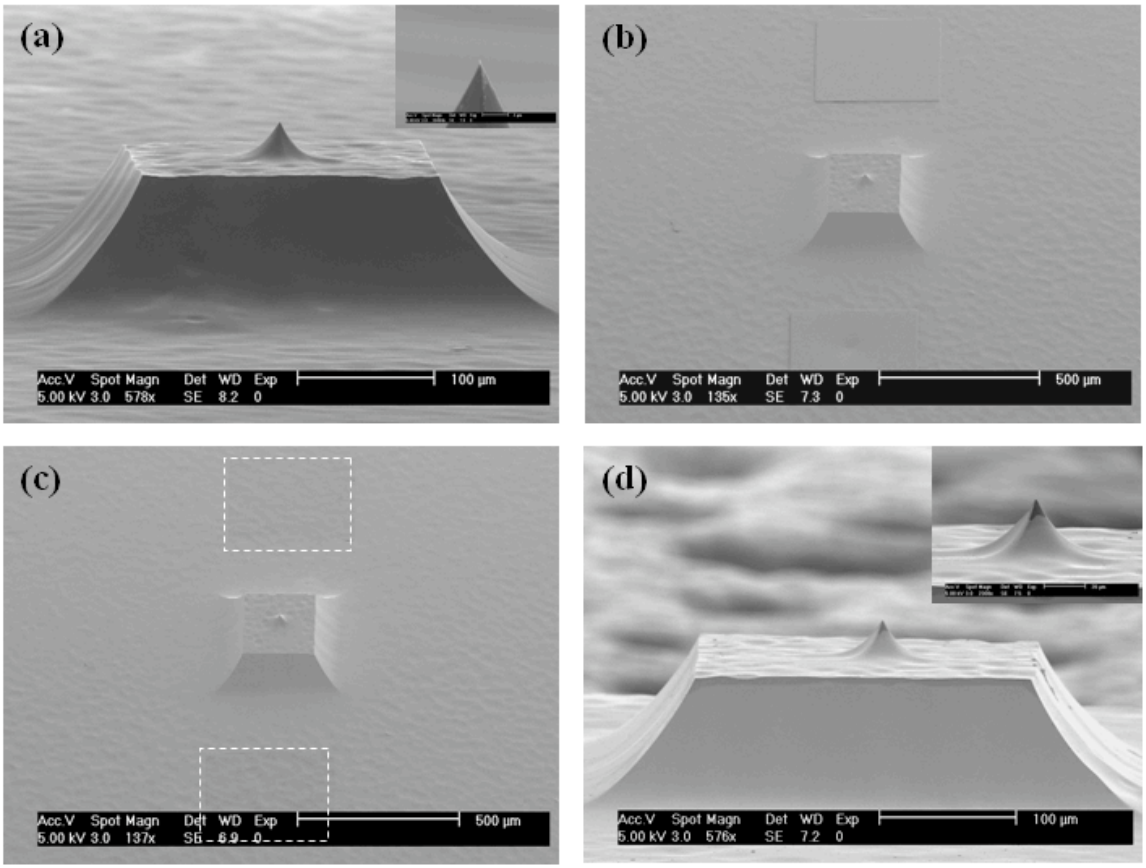

Figure 4.20: SEM images of a multilayered silicon tip for SPEAR (a) silicon tip and inset the apex of the tip, (b) sputtered outer Au layer with a resist pattern, (c) removed resist pattern and (d) opened apex of the tip, corresponding to the stage shown in Figure 4.19 (a), (d), (e) and (f) respectively.

4.3.3 Design of Multilayered Tip Holder

The multilayered silicon tip requires three electrical connections, as shown in Figure 4.17. To make the contacts, wire bonding between tip and a tip holder was used. Wire bonding is an electrical interconnection technique using a combination of heat, pressure and/or ultrasonic energy to attach a thin wire to semiconductor devices. Here 25 μm diameter aluminium wire was pressed onto the surface. Figure 4.21 shows a wire bonded to the tip chip surface. The wire bond dimensions constrain the minimum size of the electrical contact area on the chip to 100 × 140 μm, as shown in Figure 4.21(a). Figure 4.21(b) shows a side view of the bonded wires. The height of the wire above the

chip is ~30 μm. The total mesa and tip height must be significantly greater than this to avoid problem related to angular alignment. For this application a mesa and tip height of 140 μm was chosen. Figure 4.22(a) illustrates the SPEAR tip holder schematically in plan view. The main design was done by Christopher Jones in Nanoscale Physics Research Laboratory. The tip holder was designed to mount and transfer in UHV STM which forms the basis of the SPEAR system. The main body and electrodes were made of ceramic and copper, respectively. The silicon tip substrate is mounted on the centre of the tip holder using a small amount of silver paste or conducting UHV glue.

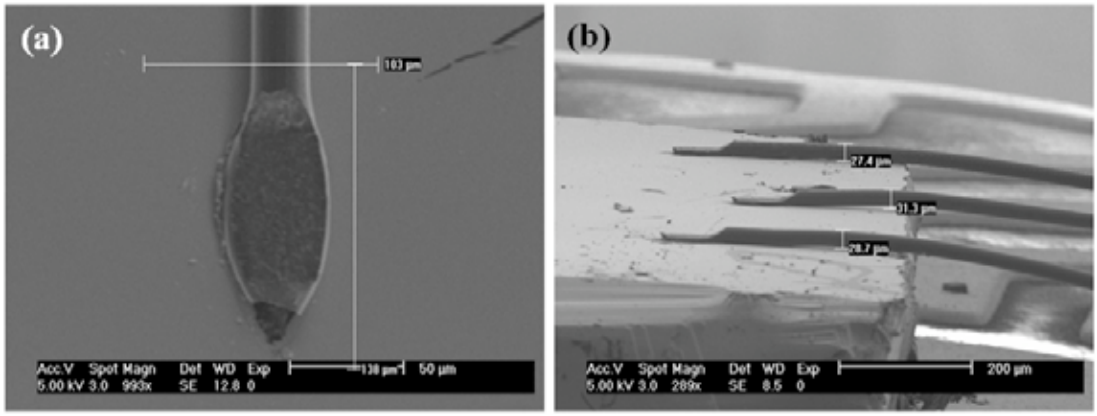

Figure 4.21: SEM images of the wire bond (a) plan view. The contact area requires 100×140 μm, approximately. (b) Side view. The height of wire is below 30 μm.

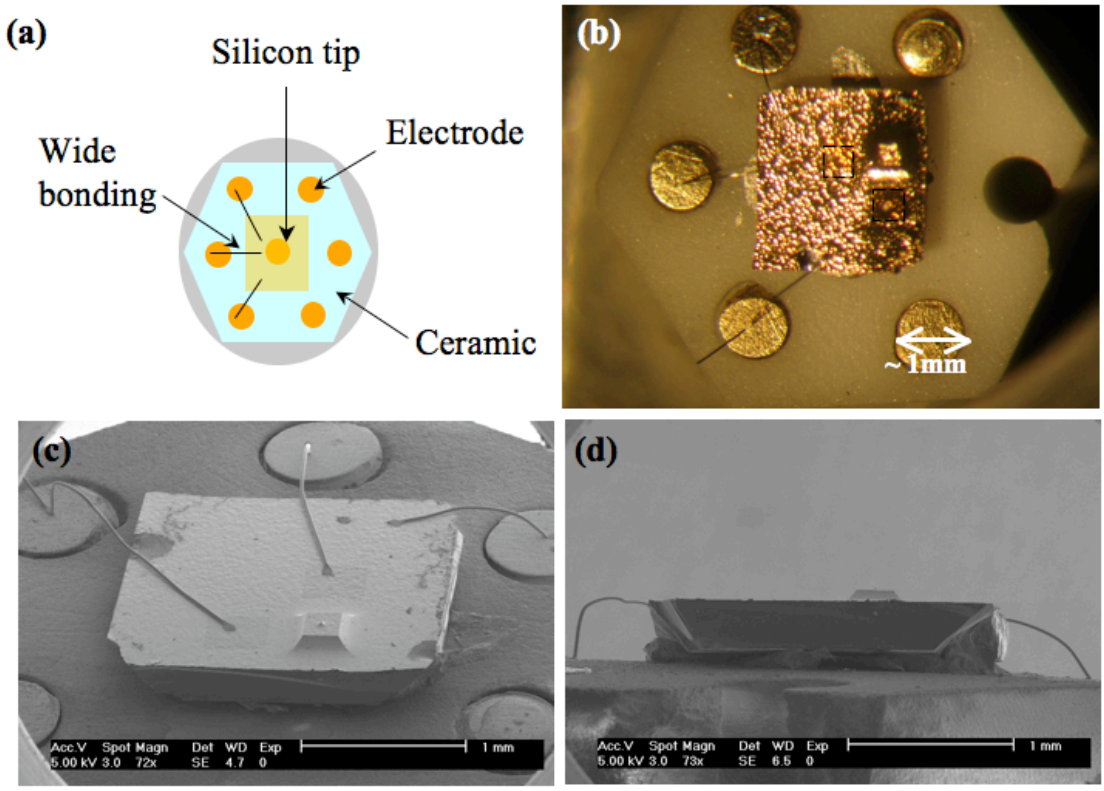

Figure 4.22: (a) Design of the SPEAR tip holder, (b) photograph of the multilayered silicon tip mounted on the tip holder with wire bonding, (c) image of a multilayered silicon tip with connections and (d) side view of the same.

Figure 4.22(b) and (c) shows a photograph image and an SEM image of a multilayered silicon tip on the tip holder with wire bonded connections. Two wires are connected to the inner metal layer and a further connection is made to the outer metal layer. Figure 4.22(d) shows a side SEM view of the wired tip.

Chapter Five

Application of Microfabricated Silicon Tips in SPM

This chapter reports on how microfabricated silicon tips were applied in STM and SPELS. First, an Au coated silicon tip was used as an STM probe. Atomic resolution STM images of graphite and STM images of the superlattice structure of graphite, Au_{100} clusters, and Ag_{3000} clusters were obtained. These result shows that the Au coated silicon tip can be successfully employed as an STM probe. Secondly, a microfabricated co-axial silicon tip with Au coated cathode is demonstrated as a SPELS probe. "Simple" Au coated silicon tips and chemically etched tungsten tips are also investigated in SPELS for comparison with the co-axial silicon tips. The field emission properties and the stability of the tips are reported. SPELS spectra of graphite are obtained with all three kinds of tip, and electrostatic lens effects in a hemispherical analyser were also investigated. The co-axial silicon tip has screened the long-range electric field so that secondary electrons' features are strongly represented.

5.1 Scanning Tunnelling Microscopy (STM)

The STM tip is the most important component in obtaining an atomic scale STM image of a surface. The size, shape, and cleanliness of the STM tip affect the atomic scale of STM images. Various tip preparation techniques have been developed since Binnig *et al.* produced the first tunnelling tips from 1 mm diameter tungsten wire which was sharpened mechanically by grinding [5]. STM tips are usually made from tungsten, gold, or platinum-iridium (Pt/Ir) wires by mechanical or electrochemical etching. Figure 5.1 shows SEM images of (a) a mechanically cut Pt/Ir tip, (b) a chemically etched tungsten tip, and (c) a microfabricated silicon tip. Mechanically sharpened Pt/Ir tips can be simply prepared by clipping the ends of the wire at an angle with wire cutters; however, this means that the shapes of the tips are hard to control, as shown in Figure 5.1(a). The electrochemical method is the most common in UHV STM and among inexpensive methods of creating tips for STM applications. Figure 5.1(b) shows a typical tungsten tip which has a radius of ~ 40 nm. The consistency of tip size and shape is also difficult to control using this process and tips are often contaminated during the etching procedure.

However, the dimensions of a microfabricated silicon tip can be carefully controlled using reproducible microfabrication techniques and the apex can be made much sharper than a Pt/Ir tip or a chemically etched tungsten tip. The shape of the microfabricated silicon tip is well designed and a silicon tip with a radius of 15 nm is shown in Figure 5.1(c). Here, the microfabricated Au coated silicon tips are demonstrated in STM.

The STM (Digital Instruments NanoScope II) was operated in ambient conditions. In order to test the microfabricated silicon tip, it was mounted onto a specially designed tip holder using a silver paste. This was then sputter coated with 20

nm of Au on top of a 5 nm adhesion layer of chromium to make it suitable for STM measurement in air. The radius of the tip became ~ 25 nm after the Au layer was coated on the silicon tip. The thickness of the Au layer was measured on the planar substrate so that a much thinner Au layer was coated on the silicon tip. Deposition of the tip metal coating was performed after mounting the tip on the holder so that an electrical contact could be made between the metal layer and the tip holder without any physical clamping to the top of the wafer.

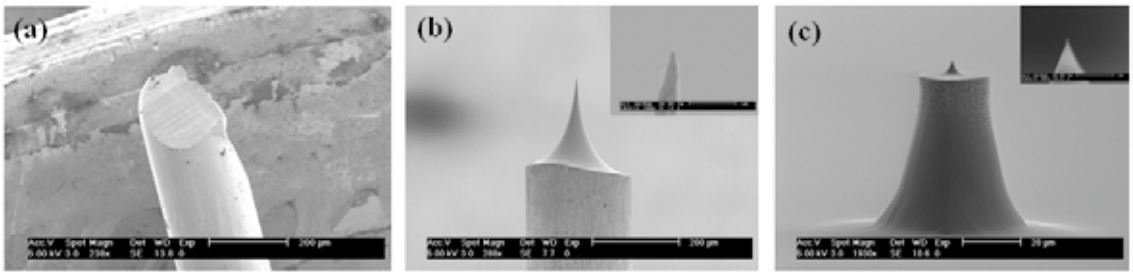

Figure 5.1: STM images of (a) a mechanically cut Pt/Ir tip, (b) a chemically etched tungsten tip: inset: the apex (radius ~ 40 nm), and (c) a microfabricated silicon tip; inset: the apex (radius ~15 nm).

The performance of the Au coated silicon tip was evaluated in the STM using highly oriented pyrolytic graphite as a substrate in air. The graphite surface was prepared by cleaving with a suitable sticky material, Scotch tape, to leave a clean uniform surface. Graphite is one of the most commonly used substrates in an STM because graphite has a flat surface on an atomic scale, is inert under ambient conditions, and is easy to handle, prepare, and clean. Figure 5.2 shows the structure of the graphite lattice. Graphite is composed of layers that are combined by Van der Waals bonds. The hexagonal structure of each layer has strong σ bonding of the hybridized 2S, $2P_x$, and $2P_y$ orbitals. The π bonds between atoms in the layer are a P_z orbital. The carbon–carbon distance between hexagonal planes is 1.42 Å and the distance between each

layer is 3.35 Å. Each layer was displaced in the ABA type displacement and it gives rise to inequivalent sites of atoms (called types α and β) [39].

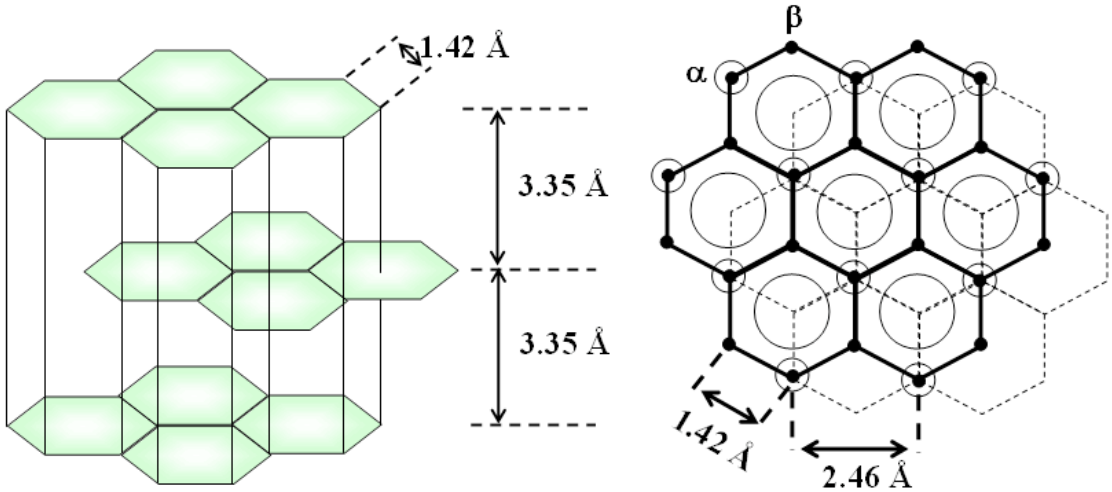

(a) (b)

Figure 5.2: The layer structure of graphite (a) side view and (b) top view. The distances between carbons and layers are 1.42 Å and 3.35 Å, respectively. Each layer was displaced in the ABA type displacement, giving rise to inequivalent sites of atoms (called types α and β). After [39]

Figure 5.3 shows an atomic resolution STM image of graphite and its height profile obtained with the Au coated silicon tip in air. Under optimum conditions atomic spatial resolution was achieved. The STM image was taken with a tunnelling current of 3.0 nA, a bias voltage of 0.1 V, and a scanning frequency of 3.0 Hz. The distance between each peak two positions was 0.25 ± 0.04 nm. The atomic spacing in the STM image appears to be approximately 0.25 nm rather than the actual 0.142 nm. This value matches the theoretical value of 0.246 nm [39]. These atomic scale images demonstrate the success of using silicon nanoprobes in STM.

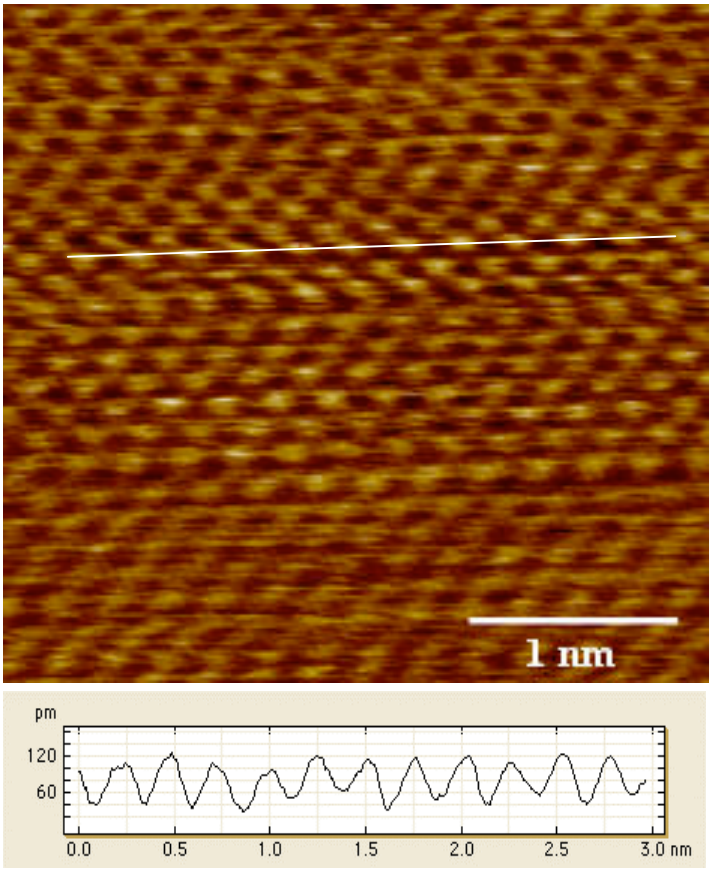

Figure 5.3: Atomic resolution STM image of graphite (0.1 V × 3.0 nA) and its height profile obtained with an Au coated silicon tip in air.

Another interesting STM image of graphite is shown in Figure 5.4. The Au coated silicon tip was prepared using the same method as explained previously. The flake of graphite shows the superlattice and a magnified STM image of the superlattice on graphite is shown in Figure 5.4(b). Superlattice structures have a superperiodic hexagonal structure similar to the graphite atomic lattice. Kuwabara *et al.* suggested that the superperiodic features might be Moiré patterns due to rotational misorientation between two graphite layers [93]. The superlattice structures of the graphite phenomenon have been observed by many groups [94, 95]. The superlattice was introduced by various kinds of defects on graphite; for example, heating or sputtering. No further processes are used to produce superlattice structures on graphite in this study. The STM measurement was done with a tunnelling current of 0.6 nA and a bias

voltage of 0.4 V in ambient conditions. A terrace on the graphite shows the superlattice with a periodicity of 5.6 nm. The STM image has been filtered in the Fourier domain and it is shown in the inset image of Figure 5.4(a). This Fast Fourier Transform (FFT) image shows that the STM image of graphite has hexagonal symmetry.

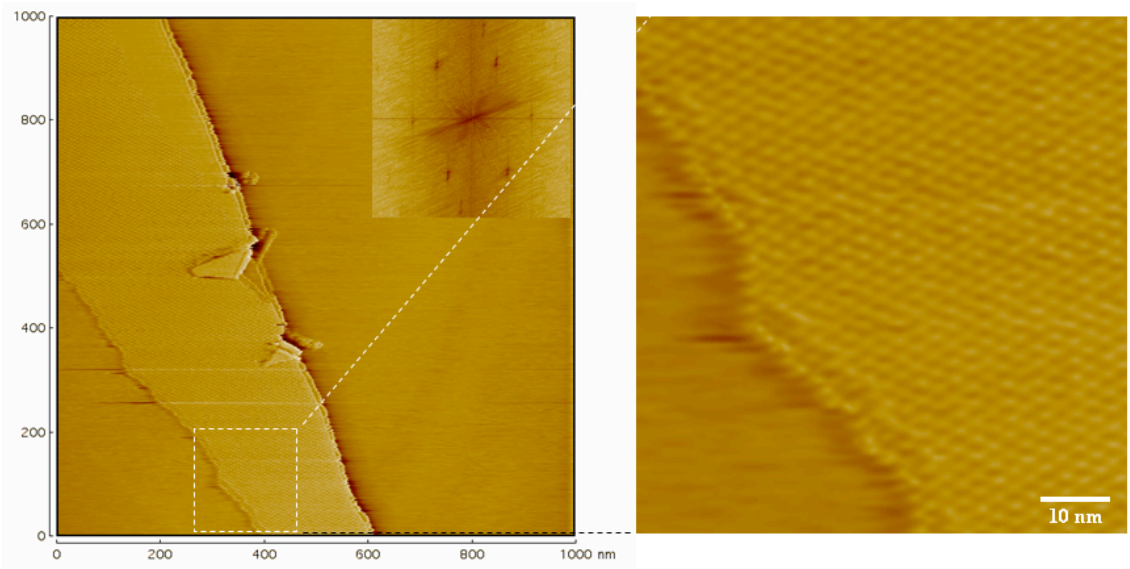

(a) (b)

Figure 5.4: (a) STM images of superlattice on graphite (0.6 nA × 0.4 V); the inset shows the corresponding FFT. (b) STM image (70 × 70 nm) showing a boundary that separates the superlattice from the graphite substrate.

Pinned Au_{100} clusters on graphite were also used as a nanostructured test sample. Au clusters have various applications in catalysis, nanoelectronic circuits, and biological materials [96–98]. Au_{100} clusters were prepared using an RF magnetron sputtering gas condensation cluster beam source in the Nanoscale Physics Research Laboratory [99]. A schematic of the cluster source is shown in Figure 5.5 [100]. The cluster source consists of three main parts. The first part generates clusters of various sizes in a liquid nitrogen cooled magnetron-sputtering source. Ar plasma is ignited in front of the metal target and the Au target is bombarded by Ar^+ ions. In this process, Au

atoms are sputtered off the target. Then, on mixing with helium gas, one of whose functions is to conduct heat to the liquid nitrogen cooled chamber wall, there are hundreds of thousands of collisions among different particles. Clusters will form and continue to grow to various sizes. Then in the second stage, joint optics is used to extract these clusters and to accelerate and focus them into a well-defined beam. In the final stage, electrically charged clusters are size-selected according to their mass using a time-of-flight mass filter. The mass selected Au clusters were deposited on a graphite substrate with sufficient kinetic energy to "pin" the clusters to their individual points of impact on the surface [101]. The pinned Au_{100} clusters are very stable in ambient conditions, thus making the sample suitable for testing in air.

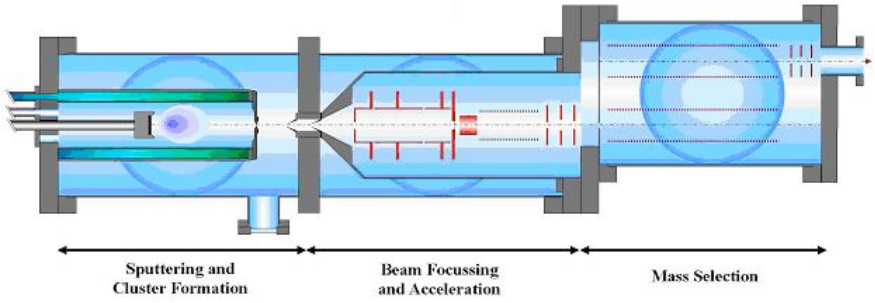

Figure 5.5: Schematic of the RF magnetron sputtering gas condensation cluster beam source. The first part generates clusters from a magnetron-sputtering source and clusters are then focused in the second stage. Finally, clusters are size-selected using time-of-flight mass filter. From [100]

Figure 5.6(a) and (b) show STM images of Au_{100} clusters on a graphite substrate in a 500 × 500 nm scan and a 60 × 60 nm scan respectively. The STM image was taken with a tunnelling current of 1.5 nA and a bias voltage of 0.3 V. The distribution of heights and diameters in a 100 × 100 nm scan area is shown in Figure 5.7(a) and (b). The mean height and diameter of the Au_{100} clusters are 0.52 ± 0.15 nm and 3.12 ± 1.12 nm respectively.

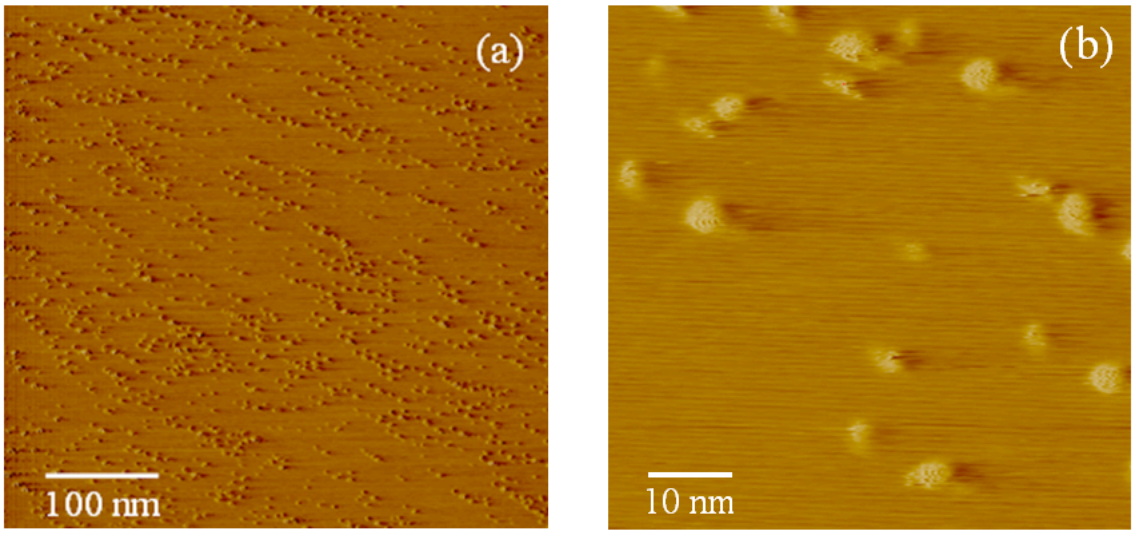

Figure 5.6: STM images of Au_{100} clusters (0.3 V × 1.5 nA): (a) 500 × 500 nm scan and (b) 60 × 60 nm scan.

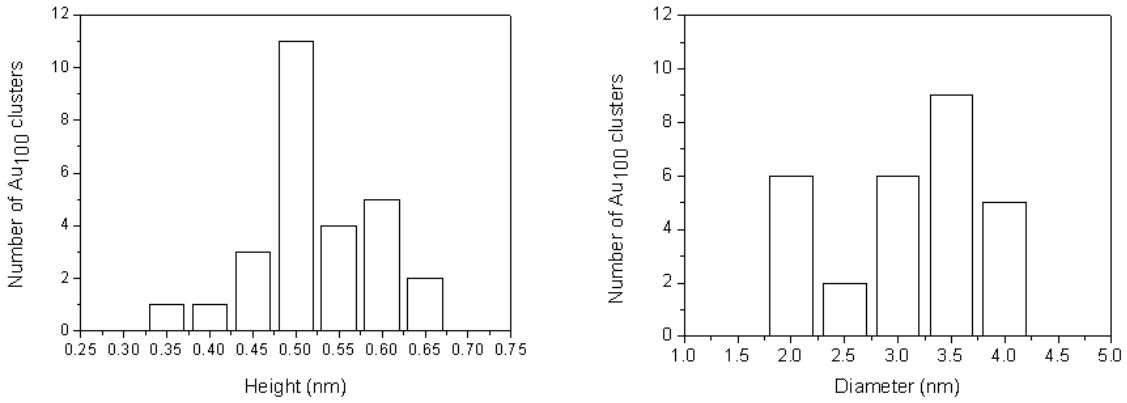

(a) (b)

Figure 5.7: Distributions of (a) height (nm) and (b) diameter (nm) of Au_{100} clusters in a 100 × 100 nm area.

The performance of the Au coated silicon tip was also tested as an STM (Omicron STM-1) probe in a UHV environment (P = 6 × 10^{-10} mbar). Pinned Ag_{3000} clusters were also prepared by the cluster source onto an Au/mica substrate. Ag_{3000} clusters are easily oxidized in air so this sample is only suitable in a UHV system. In order to avoid mechanical noise, all pumps are switched off during the scanning processes. The sample is free from any contaminants in a UHV environment, so more clear STM images can be obtained. Figure 5.8 shows STM images of Ag_{3000} clusters on

Au/mica substrate. The Ag_{3000} clusters fully cover the centre of the substrate and are aggregated to the edges of the substrate as shown in Figure 5.8(a) and (b) respectively. The STM measurement in Figure 5.8(a) was done with a tunnelling current of 0.2 nA and a bias voltage of 0.4 V. Ag_{3000} clusters were pinned compactly and the average diameter of Ag_{3000} was approximately 20~30 nm. The STM measurement in Figure 5.8(b) was done with a tunnelling current of 0.2 nA and a bias voltage of 0.9 V. As shown in Figure 5.8(a), the Ag_{3000} clusters provide more dense coverage than the Au_{100} clusters in Figure 5.6. The STM images of Ag_{3000} clusters taken from an Au coated silicon tip are also compared with those taken from a normal tungsten tip. The same sample is used for comparing STM images. Figure 5.9 shows the STM image of Ag_{3000} clusters taken from a normal tungsten tip. A tunnelling current of 2 nA and a bias voltage of –0.2 V were used. The Ag_{3000} clusters fully cover the scanning area, in the same way as in Figure 5.8(a). The diameter of an Ag_{3000} cluster is approximately 25 nm in both STM images. The STM images of Ag_{3000} clusters which are taken from the Au coated silicon tip (Figure 5.8(a), (b)) shows a clearer cluster feature than the STM images of Ag_{3000} clusters taken from the tungsten tip (Figure 5.9). These STM images demonstrate that the microfabricated Au coated silicon tip has sufficiently good performance to be used as an STM tip.

Microfabricated silicon tip is possible to batch processes with well-controlled tip dimensions as discussed in chapter 4.1. Therefore, microfabricated silicon tip have more chance to further development as a STM probe, for example, multiple STM probe.

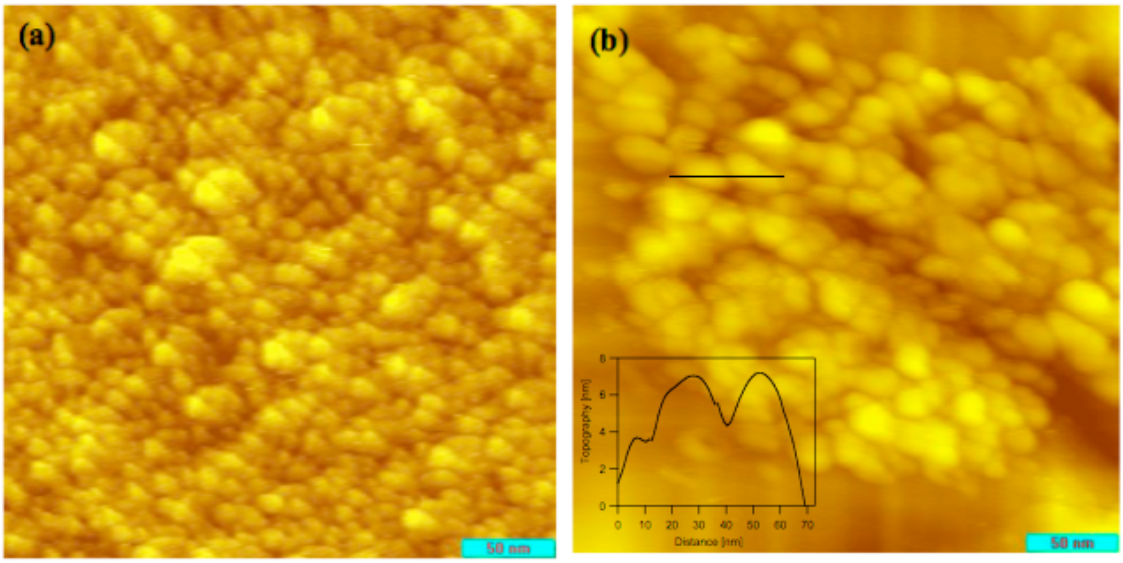

Figure 5.8: STM images of Ag_{3000} clusters on Au/mica substrate in a UHV environment, taken from an Au coated silicon tip: (a) dense Ag_{3000} clusters (0.2 nA × 0.4 V); (b) aggregated Ag_{3000} clusters (0.2 nA × 0.9 V).

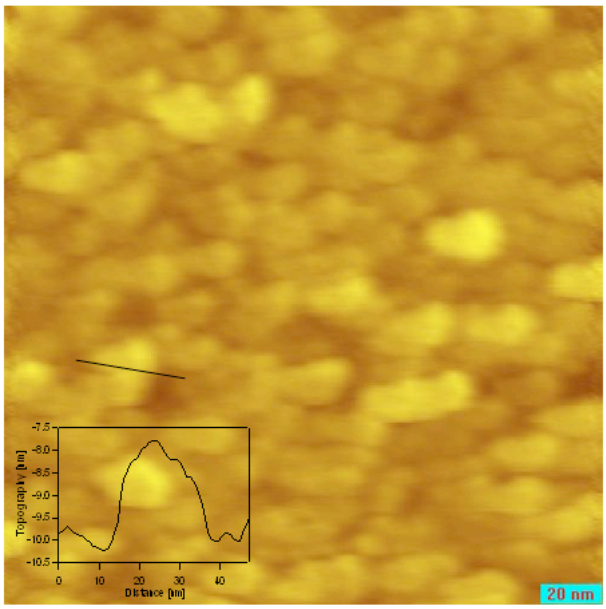

Figure 5.9: STM images of Ag_{3000} clusters (2 nA × –0.2 V) on Au/mica substrate in a UHV environment, taken from a tungsten tip. After [102]

5.2 Field Emission Characteristics

The field emission properties and stabilities of an Au coated silicon tip, an Au cathode co-axial silicon tip, and a tungsten tip are studied. A high field emission current, low tip bias voltage, and stable field emission current are required to obtain good SPELS spectra. All field emission measurements were carried out with a base pressure of 6×10^{-10} mbar at room temperature.

Au Coated Silicon Tip

The field emission properties of Au coated silicon tips were investigated before Au cathode co-axial silicon tips were applied to the SPELS. The native oxide was removed by HF and then an Au layer was immediately sputtered on a silicon tip. The Au layer was thus in ohmic contact with a silicon tip. A negative bias was applied through the silicon substrate on the backside and field emission current was emitted from the Au surface.

The current-voltage characteristics and the Fowler-Nordheim plot are presented in Figure 5.10(a) and (b) respectively. The Au coated silicon tip and a graphite substrate were used as a cathode and an anode respectively. The distance between cathode and anode was 624 nm. The field emission data were collected over a voltage range of 0 V to -200 V covering a current of 0 to ~6 μA. The voltage was increased from 0 V to -200 V and also decreased from -200 V to 0 V. The field emission current shows stable behaviour as both increasing and decreasing voltages have reproducible characteristics. If the tip has contamination or a blunt area on the apex, the field emission properties of the tip are not reproducible. Figure 5.10(b) illustrates that field emission from an Au coated silicon tip is successfully described by Fowler-Nordheim theory. The red and

black circles are the experimental data and the solid lines (blue) are a result of linearly fitting from the experimental data.

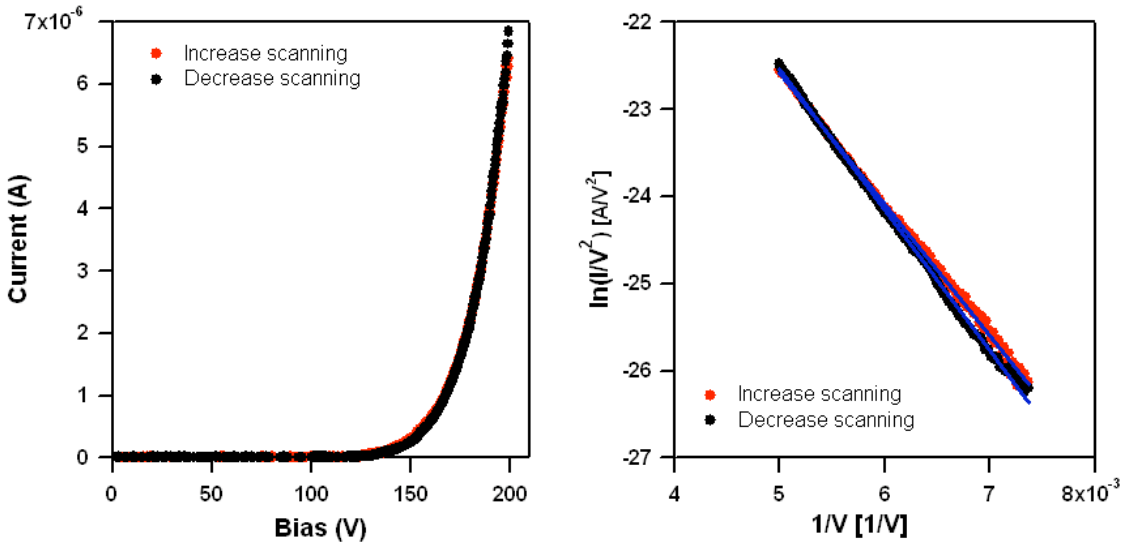

(a) (b)

Figure 5.10: (a) Current-voltage characteristics and (b) corresponding Fowler-Nordheim plot of the Au coated silicon tip. The red and black circles are the experimental data and the solid lines (blue) are a result of linearly fitting from the experimental data.

It is observed that plotting $\ln(I/V^2)$ versus 1/V yields a straight line in agreement with a Fowler-Nordheim equation, confirming that the current is the result of field emission. Following the Fowler-Nordheim Equation (2.26), field enhancement factor (β) can be extracted from the Fowler-Nordheim plots of the Au coated silicon tip assuming a work function of 5.1 eV for Au. The straight line of slope (m) is a $-6.8\times10^{7}\phi^{3/2}kR$ so that $\beta\,(\mathrm{cm}^{-1})$ can be obtained from *1/kR*. $\beta\,(\mathrm{cm}^{-1})$ is related to the sharpness, structure, and geometry of tips. The m and calculated β value of the Au coated silicon tip are shown in Table 5.1. The field emission properties were measured up to several days and have shown stable current-voltage characteristics. This means

that an Au coated silicon tip is stable in a UHV system and can be used as a field emitter for SPELS.

Table 5.1: Values of the slope and field enhancement factor taken from the Au coated silicon tip

	Slope (m)	Field enhancement factor (β)
Increase scanning	–1509.8	5.18×10^5 cm^{-1}
Decrease scanning	–1613.5	4.85×10^5 cm^{-1}

Au Cathode Co-axial Silicon Tip

The Au cathode co-axial silicon tip consists of Si/Au/HfO_2/Au layers and the outer Au layer and HfO_2 layer are stripped from the apex. The field emission current is thus emitted from the inner Au layer. This Au cathode co-axial silicon tip has a more complicated fabrication process than an Au coated silicon tip does so it is possible to contaminate the apex during the fabrication processes. For example, the Au cathode co-axial silicon tip is covered by the electron beam resist and it is then dipped into the etchant to remove the HfO_2 and the outer Au layer. Even though the electron beam resist was removed completely using chemicals, carbon atoms may remain on the apex or some contamination may be introduced when transferring the tip from the atmosphere to the UHV system. These contaminations can affect the field emission current. Oxygen plasma can be used to remove the residual contaminations. This is a very common method in a microfabrication process but it is possible to oxidize the Au surface [103]. The apex can also be damaged during oxygen plasma treatment so it is not used in this study.

Figure 5.11 shows the field emission properties of the Au cathode co-axial silicon tip. The field emission current is slowly increased on consecutive current-voltage measurements. The distance between cathode (co-axial silicon tip) and anode (graphite substrate) is 700 nm. The field emission current was measured over a voltage range of 50 V to 200 V. The field emission current can be seen to fluctuate slightly at the beginning in Figure 5.11(a) and the field emission current is gradually increased at third scanning as shown in Figure 5.11(c). This is a very common process in a silicon field emitter and is called an "aging" process [104, 105]. This behaviour can be explained by the contaminations being emitted due to the relatively high emission current heating the tip.

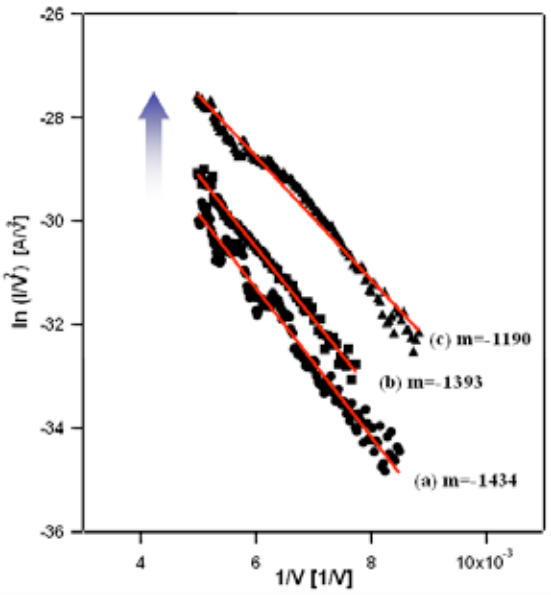

Figure 5.11: Fowler-Nordheim plots corresponding to Au cathode co-axial silicon tips: (a) first, (b) second, and (c) third scan. The dots (black) are the experimental data and the solid lines (red) are a result of linearly fitting from the experimental data.

The straight line of slope (m) was obtained from the Fowler-Nordheim plot and the values of m are (a) –1434, (b) –1393, and (c) –1190. The field enhancement factor (β) was then calculated from these values of m and the β of (a) the first, (b) second, and (c)

third scanning were 5.4×10^5 cm^{-1}, 5.6×10^5 cm^{-1}, and 6.6×10^5 cm^{-1} respectively, assuming a work function of 5.1 eV for Au. After the field emission was obtained several times, it was shown to be reproducible.

Field emission properties from the Au cathode co-axial silicon tip are also investigated with different tip–sample distances. Figure 5.12 shows the Fowler-Nordheim plots of the Au cathode co-axial silicon tip. The plot was represented by 1/V instead of an electric field (F = V/d). The field emission data were collected over a voltage range of 120 V to 200 V. As the tip–sample distance decreases, the field emission current increases. For example, the field emission currents of the tip–sample distances (a) 680 nm, (b) 500 nm, and (c) 480 nm are 4.5 nA, 9.7 nA, and 19 nA at –150 V respectively. The Fowler-Nordheim plot shows good linearity with a constant slope with changing distance so the low tip bias voltage can be used at a smaller tip–sample distance in a SPELS.

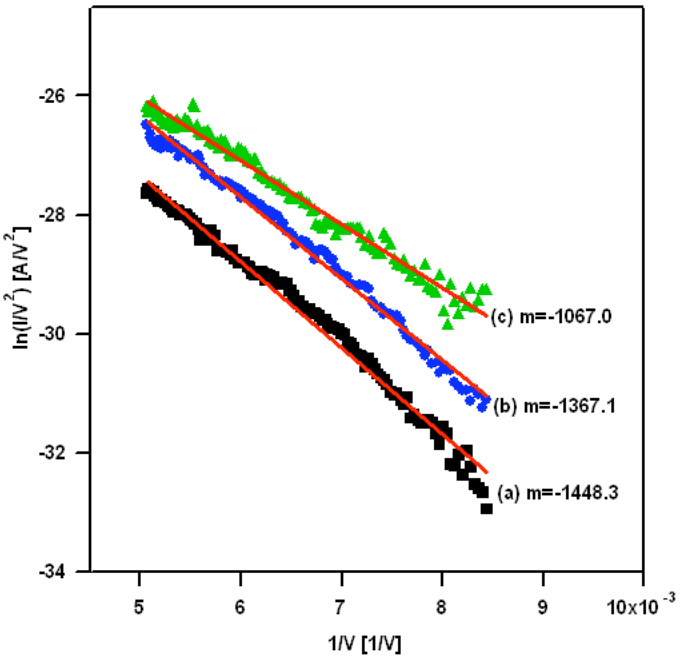

Figure 5.12: Fowler-Nordheim plots depend on the tip–sample distance corresponding to Au cathode co-axial silicon tips. The tip–sample distances are (a) 680 nm, (b) 500 nm, and (c) 480 nm. The linear fittings (red line) from the experimental data are presented.

Comparison with Au Coated Silicon Tip, Au Cathode Co-axial Silicon Tip, and Tungsten Tip

A chemically etched tungsten tip is commonly used as a probe in UHV STM and SPELS. The field emission properties of the Au coated silicon tip and the Au cathode co-axial silicon tip are thus compared with those of a normal tungsten tip. The tungsten tip is prepared following a method [106].

A polycrystalline tungsten wire (99.95%, 0.25 mm diameter) of approximately 1.5 cm length is mounted on a tip holder using a spot weld. The tungsten is electrochemically etched with a 2 M NaOH (16 g NaOH/ 200 mL H_2O) solution. A tungsten wire and an Au wire were used as a working electrode and a counter electrode respectively. Half of the tungsten wire was immersed into a solution and a dc current was passed between the electrodes. The length of the tungsten tip is between 5 and 8 mm. If the tungsten tip is too short or too long, the tip cannot approach the STM or the tip can easily damage the apex while transferring the tip. After the tungsten tip was completely etched, the tip was cleaned using deionized water and then loaded into the load-lock chamber. In order to remove any contamination, the etched tungsten tip is cleaned using an electron bombardment heating process in a preparation chamber [89]. The field emission properties are very dependent on this cleaning process [89]. The tungsten tip is then loaded into the STM and the field emission properties of the tip are subsequently tested.

The current-voltage characteristics and their Fowler-Nordheim plots corresponding to (a) the Au cathode co-axial silicon tip, (b) the Au coated silicon tip, and (c) the tungsten tip are represented in Figure 5.13 and SEM images of the apexes of those tips are shown in Figure 5.14. The tip–sample distance is ~ 600 nm.

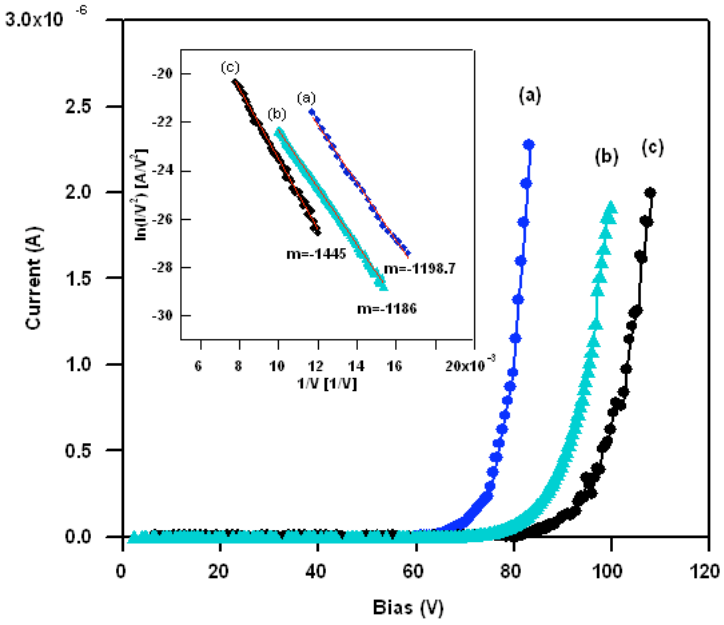

Figure 5.13: Current-voltage characteristics and Fowler-Nordheim plots (inset) corresponding to (a) the Au cathode co-axial silicon tip, (b) the Au coated silicon tip, and (c) the tungsten tip. The tip–sample distance is ~600 nm. The linear fittings (red line) from the experimental data are also presented.

Table 5.2: Field emission characteristics of three different tips

	Slope (m)	Field enhancement (β)*	Radius
(a) Au cathode co-axial silicon tip	1198.7	$6.53 \times 10^5\,cm^{-1}$	34.9 nm
(b) Au coated silicon tip	1186	$6.60 \times 10^5\,cm^{-1}$	39.5 nm
(c) Tungsten tip	1445	$4.49 \times 10^5\,cm^{-1}$	55.5 nm

(* A work function of Au and tungsten is taken from 5.1 eV and 4.5 eV respectively.)

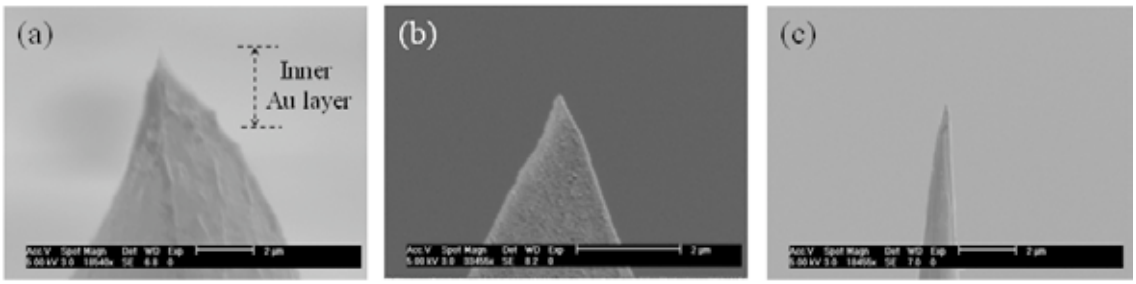

Figure 5.14: SEM images of tip apex: (a) Au cathode co-axial silicon tip (radius 34.9 nm), (b) Au coated silicon tip (radius 39.5 nm), and (c) tungsten tip (radius 55.5 nm)

The shallower slope in a Fowler-Nordheim plot is characteristic of a shaper emitter and the plot represents higher values of 1/V (from left to right in Figure 5.13). The slopes of the Au cathode co-axial silicon tip (Figure 5.13(a)) and the Au coated silicon tip (Figure 5.13(b)) are slightly shaper than that of a tungsten tip (Figure 5.13(c)). The slope (*m*), field enhancement factor (β), and radius of the apex are presented in Table 5.2. The silicon tips are shown to have better field emission properties than the tungsten tip as seen in Figure 5.13. The field emission current depends on the material, geometry, sharpness, and cleanliness. There are two possible reasons.

First, the Au cathode co-axial silicon tip and Au coated silicon tip can be made sharper (by around 40 nm) than the tungsten tip (55.5 nm) so they may give better field emission properties as shown in Figure 5.14. Second, the silicon tips do not undergo a further cleaning process in a UHV environment because the Au layer is not oxidized in air. However, the normal etched tungsten tip needs a careful electron bombardment heating process to remove the tungsten oxide layer. It is hard to know whether the tungsten oxide layer is removed perfectly or whether some is left on the tip. It may affect the field emission properties of the tungsten tip. The Au cathode co-axial silicon tip and the Au coated silicon tip are thus shown to be good field emitters for SPELS.

Field emission stability was also investigated. Stable field emission currents are required to obtain spectra in SPELS. Figure 5.15(a), (b), and (c) show the stability of the field emission current for the Au cathode co-axial silicon tip, Au coated silicon tip, and tungsten tip respectively. The applied voltages are –200 V. The average field emission currents of (a) the Au cathode co-axial silicon tip, (b) the Au coated silicon tip, and (c) the tungsten tip are found to be 6.6 μA, 1.72 μA, and 2.09 μA respectively. In Figure 5.15(a) and (b), the field emission current shows stability during measurement.

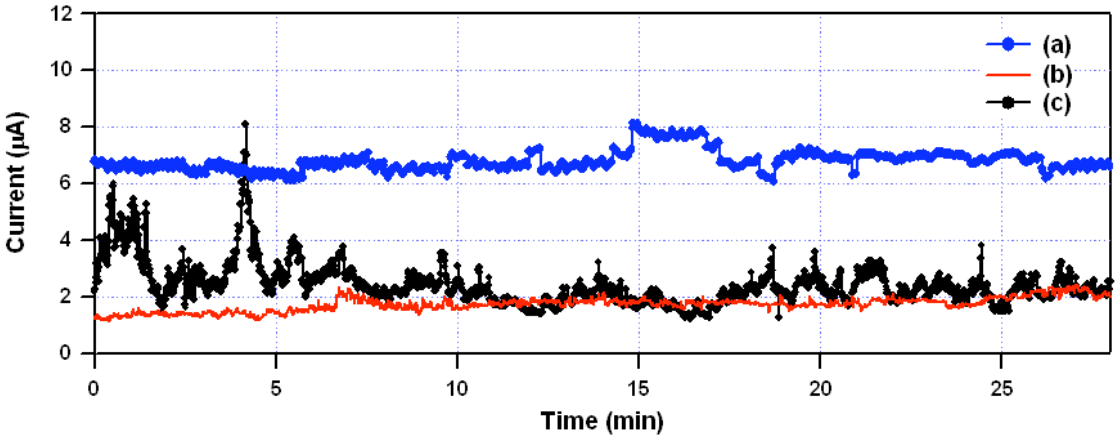

Figure 5.15: Stability of the field emission current at –200 V: (a) Au cathode co-axial silicon tip, (b) Au coated silicon tip, and (c) tungsten tip.

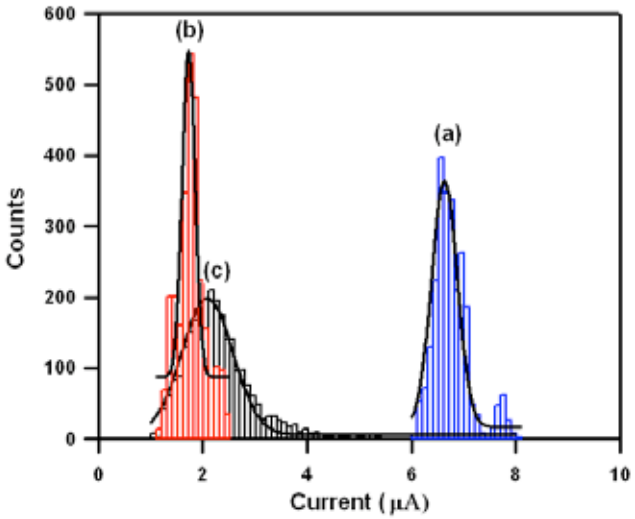

Figure 5.16: Distribution of field emission current corresponding to Figure 5.14: (a) Au cathode co-axial silicon tip, (b) Au coated silicon tip, and (c) tungsten tip.

Table 5.3: Average field emission current and distribution of field emission current.

	(a) Au cathode co-axial silicon tip	(b) Au coated silicon tip	(c) Tungsten tip
$I_{average}$ (μA)	6.6 μA	1.72 μA	2.09 μA
FWHM	0.6331	0.3236	1.195
Tip–sample distance (nm)	673 nm	520.5 nm	624 nm

However, the field emission current of the tungsten tip in Figure 5.15(c) shows dramatic fluctuation in the first ~6 minutes and diminishing fluctuation thereafter. The field emission properties of the tungsten tip may be very dependent on the tip cleaning process in a UHV system so it is difficult to make a perfectly cleaned tungsten tip every time. The distribution of field emission current is shown in Figure 5.16, which corresponds to Figure 5.15. The FWHM of the field emission currents in (a) the Au cathode co-axial silicon tip, (b) the Au coated silicon tip, and (c) the tungsten tip are 0.6331, 0.3236, and 1.195 respectively. The narrow FWHM value means that the field emission current is a stable and the Au cathode co-axial silicon tip shows an FWHM value that is two times smaller than that of the tungsten tip. The results of stability measurements are summarized in Table 5.3. The more stable field emission current of silicon tips compared to those of normal tungsten tips will be good for SPELS.

5.3 Scanning Probe Energy Loss Spectroscopy (SPELS)

Au cathode co-axial silicon tips were introduced in Chapter Four and here they are applied as an electron source for SPELS for the first time. First, the SPELS spectra of graphite from the Au coated silicon tip, which is not grounded, will be discussed. Second, the Au cathode co-axial silicon tips are tested for the SPELS and the SPELS spectra of graphite will be discussed. The aim of the Au cathode co-axial silicon tip is to screen a long range electric field so that backscattered electrons may be not affected by electric field. Third, SPELS spectra of graphite are taken from a normal tungsten tip as a reference. Figure 5.17 shows a schematic diagram of (a) the Au coated silicon tip, (b) the Au cathode co-axial silicon tip, and (c) the tungsten tip. In order to focus on the tip effects, the sample used was graphite, which is a widely known and well-understood

substrate. The hemispherical analyser is fixed at 0^{o} to the sample and all SPELS spectra are taken at 6×10^{-10} mbar.

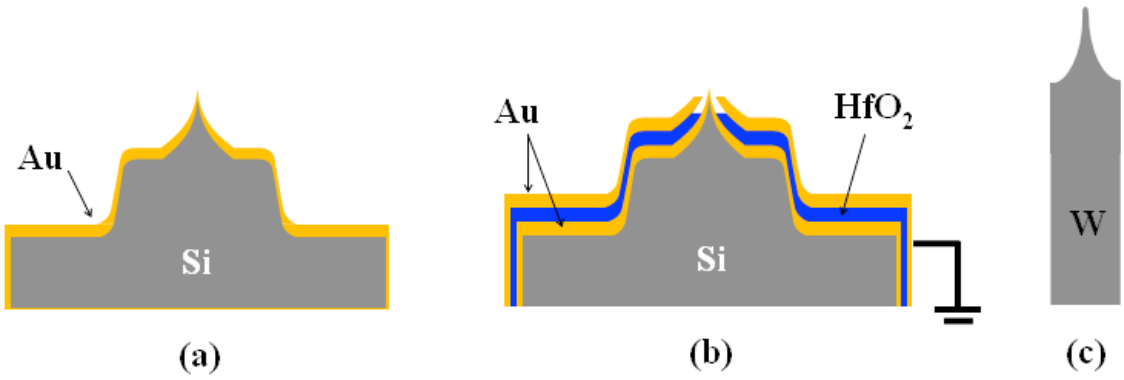

Figure 5.17: Schematic diagram of (a) the Au coated silicon tip, (b) the Au cathode co-axial silicon tip, and (c) the tungsten tip. The tip (b) is only connected with grounded shield.

The lens effects in a hemispherical electron energy analyser are also discussed with respect to SPELS spectra. The hemispherical analyser is used in conjunction with an electrostatic lens that transfers electrons from the sample to the entrance slit of the analyser. Figure 5.18 illustrates (a) the electrons' path to the hemispherical analyser via the electrostatic lens [107] and the SIMION simulation of the electrostatic lens, (b) while applying a positive bias to the lens, and (c) without applying potential to the lens (grounded). Backscattered electrons from the sample enter the electrostatic lens with kinetic energy T and are focused by the lens. The electrons then enter the hemispherical analyser with angle α as shown in Figure 5.18(a) [107]. Electrons entering the analyser are retarded by the potential at the entrance slit before reaching the electrostatic field. The spherical electrostatic field is established by the inner and outer hemispheres, which are at positive and negative potential with respect to the retard potential. Higher energy electrons move at a relatively high speed and have a chance to strike the outer hemispheres. Lower energy electrons strike the inner hemisphere easily.

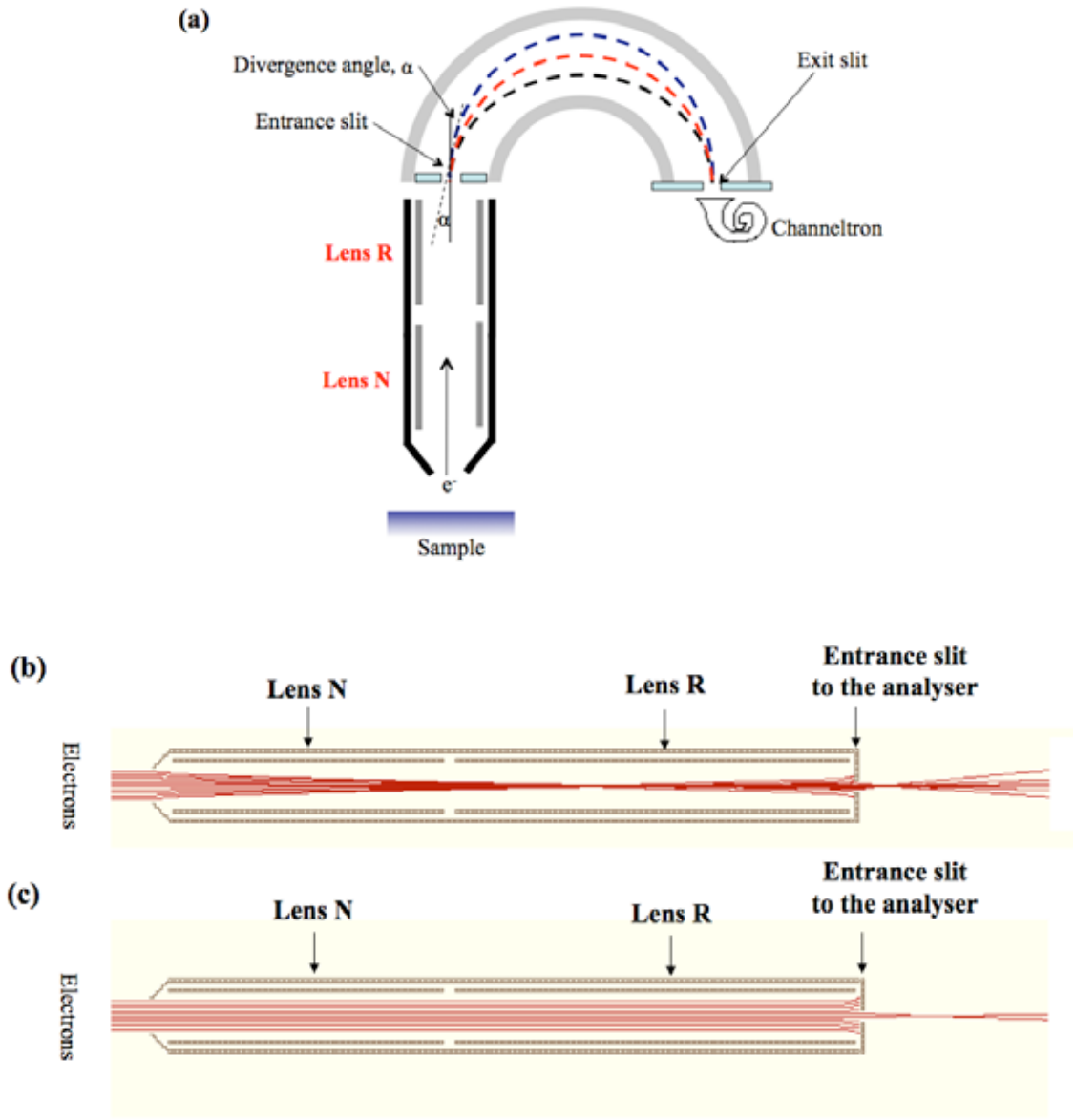

Figure 5.18: (a) Schematic of hemispherical analyser. The electrons enter the analyser via the electrostatic lens with a kinetic energy T. Electrons are focused and decelerated by the electrostatic lens. After [107]. Simulation of electrostatic lens (b) while applying positive bias to lenses and (c) grounded lenses, showing the electron path.

When electrons pass through the central orbit as shown in Figure 5.18(a), the energy resolution can thus be improved. The retard potential –66.6 V is applied at the entrance slit which is optimized to improve the energy resolution in our system. Figures 5.18(b) and (c) show the electrostatic lens used in our system. The electrostatic lens consists of the two-element transfer lenses, which are called “Lens N” (nose element) and “Lens

R" (rear element). A cylindrical symmetry around the z-axis was used with 1000 × 1000 grid lines, and one grid unit was set to 1 mm. In this simulation, the kinetic energy of backscattered electrons uses 95.5 eV and the applied potentials of Lens N, Lens R, and the entrance slit were set to +100 V, +100 V, and –66.6 V respectively as shown in Figure 5.18(b). In Figure 5.18(c), both lenses are grounded and only negative potential, –66.6 V, was applied to the entrance slit. The same positive bias between Lens N and Lens R was applied to cylindrically symmetric plates so that the electrons were more focused through the entrance slit via the electrostatic lens as shown in Figure 5.18(b). This contributes to increasing the intensity of SPELS spectra. If the electrostatic lenses are grounded, the electrons may not be focused at the entrance slit and fewer electrons are collected into the analyser, as shown in Figure 5.18(c). The analyser angular acceptance in a SPELS spectrum will be also affected by electrostatic lenses and the detail of the lenses effect will be discussed in Section 5.3.2.

5.3.1 SPELS Spectra of Graphite using an Au Coated Silicon Tip

An Au coated silicon tip is applied to SPELS for the first time in this thesis. The geometry of the silicon tip is very important to obtain a SPELS spectrum. A negative bias is applied to the whole Au coated silicon substrate (2 × 2 mm size). The silicon substrate can also generate an electric field as shown in Figure 5.19(b) and thus the backscattered electrons will be suppressed. In order to avoid this problem, the silicon tip is fabricated at the edge of the silicon substrate as shown in Figure 5.19(a).

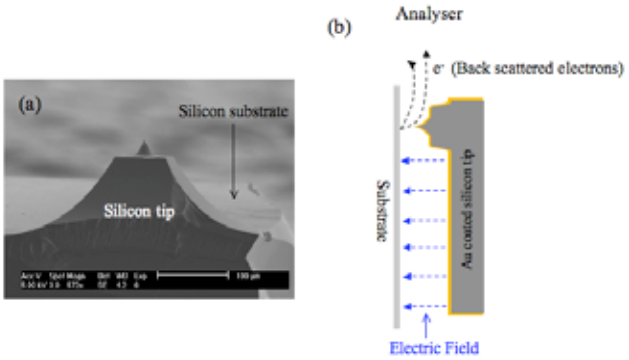

Figure 5.19: (a) SEM image of a silicon tip. The silicon tip is fabricated at the edge of the silicon substrate. (b) Schematic diagram of the geometry of the Au coated silicon tip. Negative bias applies to the tip. The tip is the edge of the silicon substrate so backscattered electrons are less affected by the electric field from the silicon substrate.

Figure 5.20 represents a typical SPELS spectrum of graphite taken with an Au coated silicon tip, showing the elastic peak, two plasmon peaks, and secondary electron emission peaks (SEE).

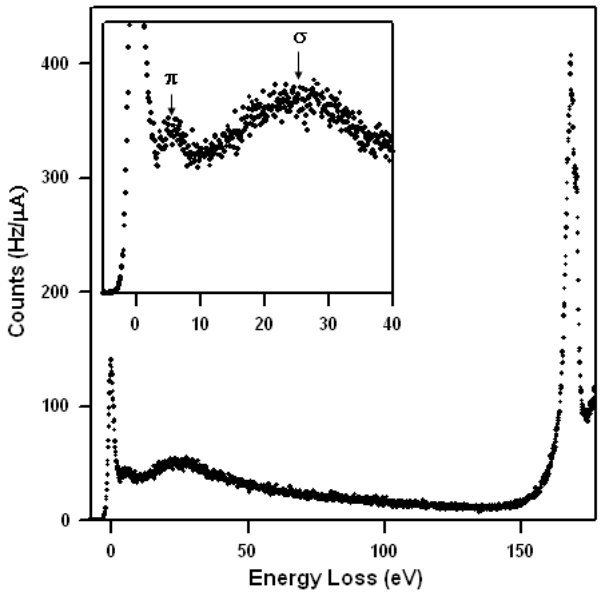

Figure 5.20: A SPELS spectrum of graphite taken with an Au coated silicon tip. The tip bias voltage is –180V, the field emission current is 16 μA, and the tip–sample distance is 638 nm. The lens is grounded. The inset shows the π and σ plasmon peaks.

The tip bias voltage, field emission current, and tip–sample distance were –180 V, ~16 μm, and 638 nm respectively. The lens is grounded. The incident electrons are

elastically and inelastically scattered from the graphite surface. Elastically scattered electrons have the same energy as the primary ones and inelastically scattered electrons have an energy loss due to interactions between the incident electrons and substrate. The elastic peak is at zero energy loss and the SEE peaks are toward the higher energy loss.

Graphite is a layered material so the surface plasmon is associated with the response to a momentum-transfer perpendicular to the c-axis (out-of-plane excitations) and to a momentum-transfer parallel to the c-axis (in-plane excitations). Two energy loss peaks are clearly seen at 6 eV (π plasmon) and 26 eV (σ plasmon). These plasmon peaks are shown in the inset in Figure 5.20. The 6 eV energy loss peak is a plasmon resonance associated with the response to a momentum-transfer perpendicular to the c-axis [108]. The 26 eV energy loss peak is represented by the collective oscillation of the σ bonded electrons of the graphite and it usually shows a broader peak. These energy loss peaks are identified by several authors [13, 108, 109]. The SEE peak can also be seen at the higher energy loss region. The SPELS spectra of graphite are presented in terms of kinetic energy relative to the vacuum level as shown in Figure 5.21(a). The sample–tip distance is fixed at 638 nm and SEE peaks are normalized to unity. The π and σ plasmon features are highlighted by a red and a blue dot respectively on a spectrum. When the tip bias voltage is increased, energy loss features are shifted to a higher kinetic energy region. However, the SEE features always have the same value of kinetic energy, which is independent of the tip bias voltage as shown in Figure 5.21(a). Figure 5.21(b) shows the detail of low kinetic energy of the graphite spectrum at a tip bias voltage of –180 V. The shoulder at 4.7 eV and the primary peak at 7 eV are observed. The interpretation of the SEE features will be discussed in detail in Section 5.3.4.

This spectrum is in very good agreement with previous SPELS spectra of graphite taken with a normal tungsten tip and thus demonstrates that the Au coated silicon tip was successfully applied to the SPELS.

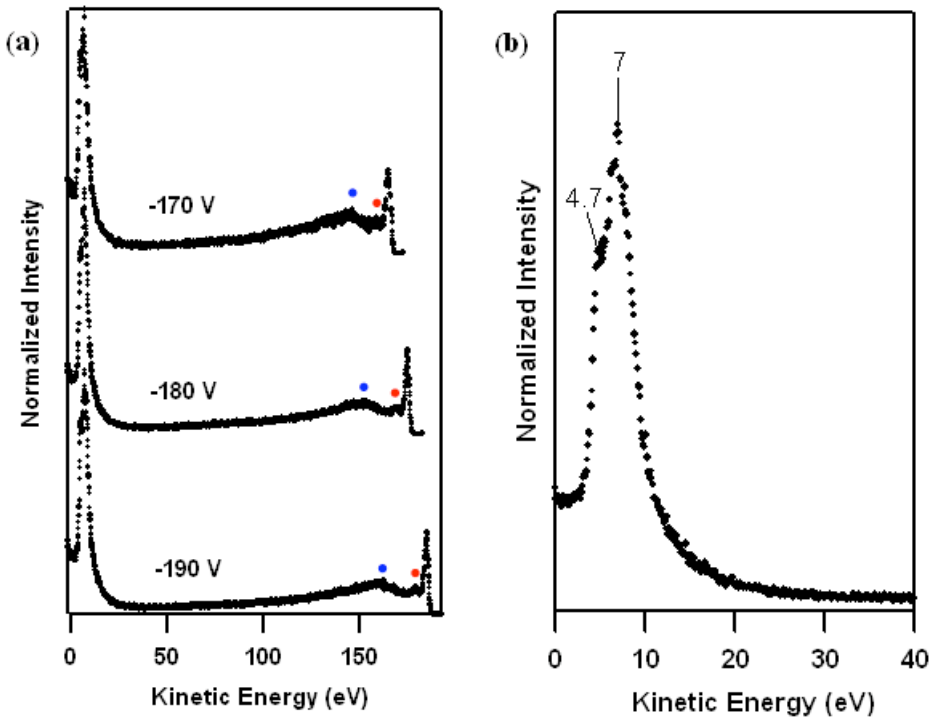

Figure 5.21: SPELS spectra of graphite taken with (a) different tip bias voltages of –170V, –180 V, and –190 V. The π and σ plasmons are highlighted by a red and a blue dot respectively. (b) Detail of the low kinetic energy of the graphite spectrum at a tip bias voltage of –180 V. The working distance is 638 nm. The lens is grounded. Spectra are presented in terms of kinetic energy relative to the vacuum level.

Here π and σ plasmon features are investigated depending on the tip bias voltage at a fixed tip–sample distance of 400 nm. The π and σ plasmons of graphite as a function of the tip bias voltage are shown in Figure 5.22. The π and σ plasmon peaks are represented at 6.2 ± 0.2 eV and 26.0 ± 0.5 eV respectively and energy loss features do not change when the tip bias voltage is increased. However, the intensity of the plasmon peaks is changed as shown in Figure 5.23. Figure 5.23(a) represents some of

the graphite spectra with a fixed tip–sample distance of 400 nm. Each spectrum is normalized to the intensity of its elastic peak. Tip bias voltages of –140 V, –170 V, and –200 V are shown corresponding to field emission currents of 8.3 μA, 34 μA, and 90 μA respectively. The intensity of π plasmon energy loss peaks is less affected by tip bias voltage because it originates from π electrons corresponding to longitudinal excitation perpendicular to the c axis [110, 111]. However, the intensity of the 26 eV (σ plasmon) energy loss peak increases with increasing tip bias voltage. It is dependent on the incident beam energy because it mostly collects the oscillation of the corresponding σ bond electrons parallel to the surface. Figure 5.23(b) shows the relative σ/π plasmon intensity as a function of tip bias voltage. At a tip bias voltage of –140V, the σ plasmon energy loss peak appears very weak. The maximum intensity of the π and σ plasmons has a similar ratio at –160 V, but at the tip bias voltage of –200 V the intensity of the σ plasmon energy loss peak is 1.3 times stronger than the π plasmon energy loss peak. This π and σ plasmon feature of graphite was also represented with different incident energies in EELS [110, 112].

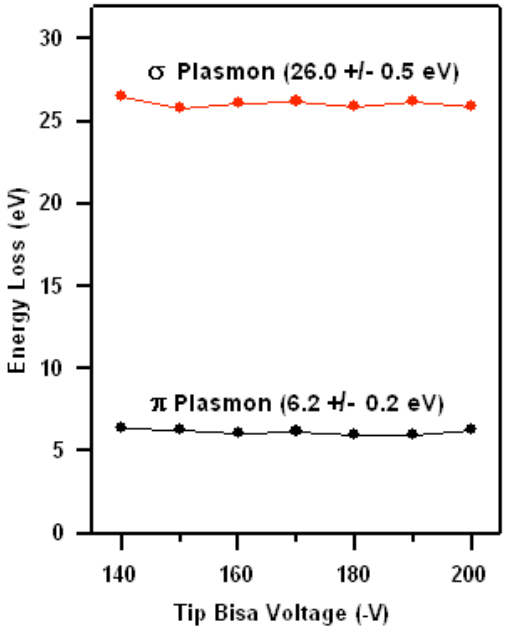

Tip bias voltage (-V)	π plasmon (eV)	σ plasmon (eV)
140	6.4	26.5
150	6.3	25.8
160	6.0	26.1
170	6.2	26.2
180	6.0	25.9
190	6.0	26.2
200	6.3	25.9

Figure 5.22: π plasmon and σ plasmon of graphite as a function of the tip bias voltage at a tip sample distance of 400 nm.

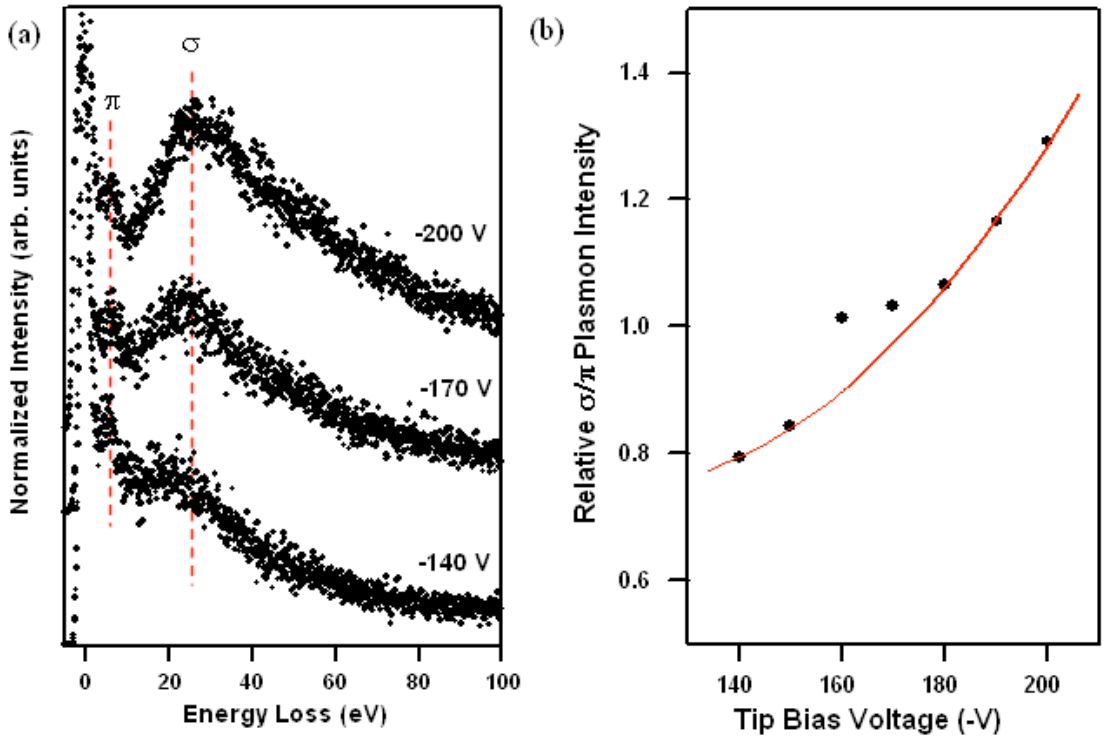

Figure 5.23: The variation of the graphite spectra taken with (a) different tip bias voltages and (b) relative $\frac{\sigma}{\pi}$ plasmon intensities as a function of tip bias voltage. The fixed working distance is 400 nm and the lens is grounded. Each spectrum is normalized to the intensity of its elastic peak.

5.3.2 SPELS Spectra of Graphite using an Au Cathode Co-axial Silicon Tip

In the previous section, the Au coated silicon tip which has no grounded element was used to obtain SPELS spectra successfully. The elastic peak, the plasmon peaks and SEE peaks can be seen clearly. The Au coated silicon tip is further developed to an Au cathode co-axial silicon tip (hereafter referred to as the co-axial silicon tip) for SPELS. The co-axial silicon tip consists of Si/Au/HfO_2/Au layers with the outer Au layer grounded to reduce the electric field between the tip and sample. A co-axial tip has been suggested in a SPELS and a primitive co-axial tungsten tip was also applied to the SPELS [113]. The hand painted etched tungsten tip and glass micropipette tip were proposed for the SPELS but these types of tips do not have a finely controlled co-axial tip structure. The shield layer covered only the sidewall of the tungsten wire and not the tip apex region. On the other hand, the co-axial silicon tips were fabricated here using well-controlled microfabrication techniques.

Here, SPELS spectra of graphite are studied using a co-axial silicon tip and an electrostatic lens effect of applied potential or grounding is also investigated in SPELS. Electrons are detected at the analyser via the electrostatic lens so the lens may affect the analyser angular acceptance. First, the positive potential was applied to the electrostatic lens labelled “Lens 1”. The positive potential is changed during the energy scan. For example, when the energy scan range operated from 0 eV to 200 eV, a positive potential was applied to the lenses that ranged from 0 V to 500 V, which was the optimized condition for obtaining a strong signal in our system.

A SPELS spectrum of graphite taken with a co-axial silicon tip is shown in Figure 5.24(a). The tip bias voltage is –200 V, the field emission current is 6 μA, and the tip–sample distance is 467 nm. The spectrum is very different from an unshielded Au coated silicon tip as shown in Figure 5.20.

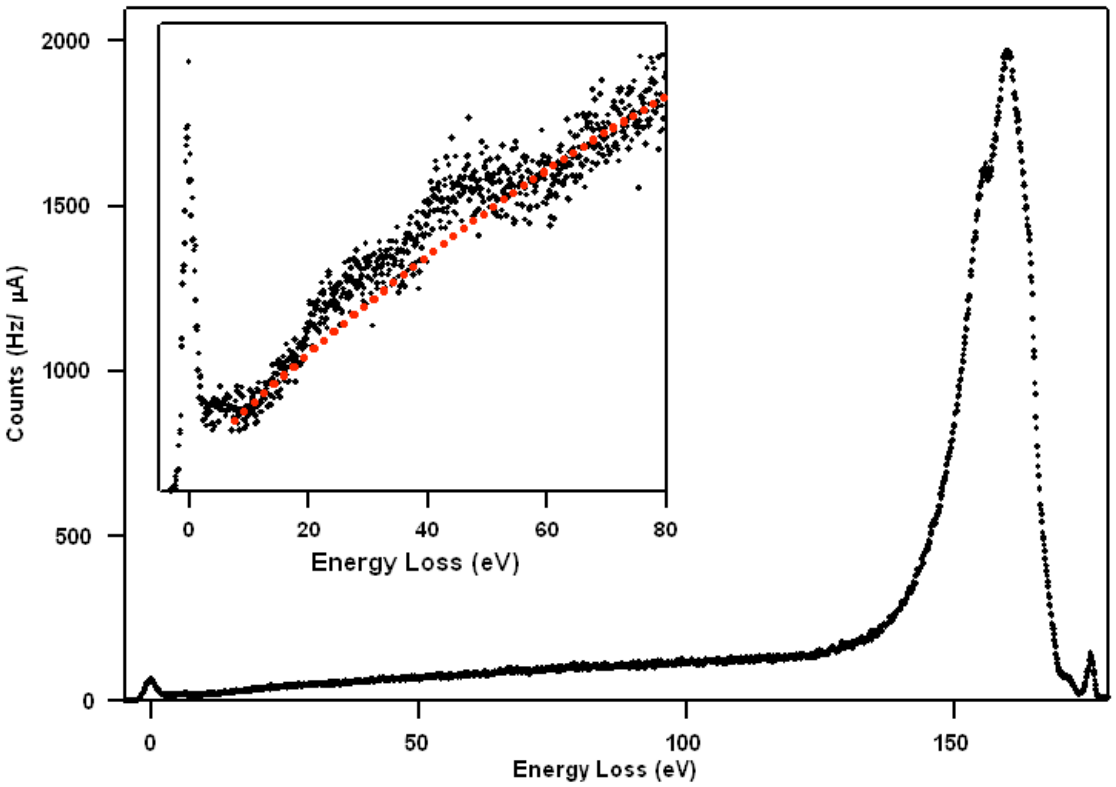

(a)

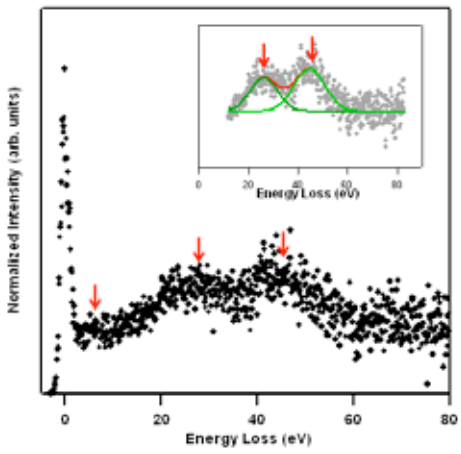

(b)

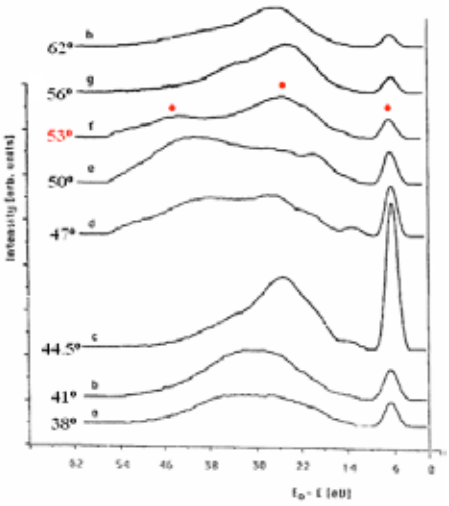

(c)

Figure 5.24: A SPELS spectrum of graphite taken with the co-axial silicon tip. A positive bias is applied to the electrostatic lens (Lens 1). The tip bias voltage is –200 V, the field emission current is 6 µA, and the tip–sample distance is 467 nm. (a) A full spectrum energy loss scan; the inset shows a highlight of the low energy loss region and the background is indicated by dotted lines, (b) after background subtraction including the two Gaussian functions at 26 eV and 44 eV. (c) Angle-resolved EELS spectra as a function of the angle of the energy analyser with respect to the sample normal. From [112].

The intensity of the SEE peak is very strong compared with those of the elastic peak and π and σ plasmon peaks. The inset shows a π plasmon peak (6 eV) and a σ plasmon peak (26 eV), and an unknown peak was observed at 44 eV. The background is also indicated by dotted lines. Figure 5.24(b) shows the spectrum after background subtraction including the two Gaussian functions at 26 eV and 44 eV. It is unusual to observe the 44 eV peak of graphite in SPELS. Diebold *et al.* reported on angle resolved EELS in reflection mode on a graphite surface [112]. The incident energy was fixed at 175 eV and the energy loss features were measured with respect to different normal angles. When the detecting angle was 53° (Figure 5.24(c)), the energy loss features of graphite were found at 6.4 eV, 26 eV, and 43 eV, which are similar to those observed in the SPELS spectrum of graphite. They explain that non-vertical interband transitions to high lying unoccupied states may be responsible for the ~ 43 eV peak [112]. However, the origin of the energy loss peak is still not known.

The angular distributions of backscattered electrons in a SPELS were reported previously by Eves *et al*. [13]. A normal tungsten tip is used for this work. The energy loss features of the Si (111)-7 × 7 and graphite surface were observed in angle resolved SPELS measurements with the strongest elastic peak signals detected when the analyser was located parallel to the surface plane. The reason is that the electric field from the negative biased tip bends the "specular" electrons to the surface. However, the co-axial tip can remove the majority of the electric field effect between the tip and the sample. In the reduced electric field, the analyser may detect conditions which are far from "specular" (energy loss peak), but secondary electrons are not constrained by the incident electrons. The hemispherical analyser was fixed parallel to the sample so that most of the energy loss peak could not arrive at the analyser. The analyser may thus be

collecting secondary electrons and it gives an SEE peak that is very strong compared with elastic or plasmon peaks.

The SPELS spectra of graphite are presented in terms of kinetic energy relative to the vacuum level, as shown in Figure 5.25. The sample–tip distance is fixed at 250 nm and SEE peaks are normalized to unity. All SPELS spectra taken from the co-axial silicon tip show strong SEE peaks at the low kinetic region and the SEE features always have the same value of kinetic energy (14.7 eV and 20.5 eV), which is independent of the tip bias voltage. The interpretation of the SEE features will be discussed in Section 5.3.4.

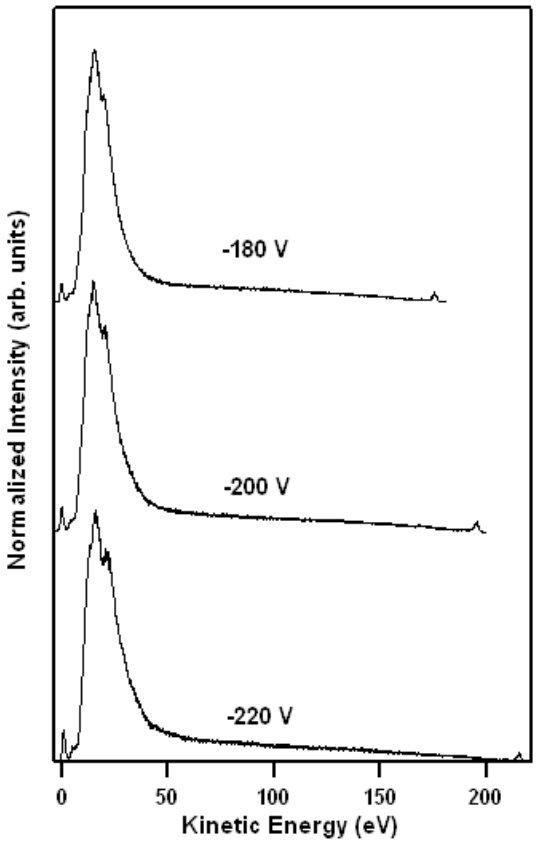

Figure 5.25: SPELS spectra of graphite taken with different tip bias voltage of –180 V, –200 V, and –220 V. The working distance is 250 nm. A positive bias is applied to the lens (Lens 1). Spectra are presented in terms of kinetic energy relative to the vacuum level.

The same data are presented in terms of energy loss are shown in Figure 5.26(a). The variation of the graphite spectra with changes in the tip bias voltage is presented. A second order polynomial background fit to the spectrum of graphite was subtracted as shown in Figure 5.26(b). Tip bias voltages are –180 V, –200 V and –220 V, corresponding to field emission currents of 5.5 μA, 12 μA, and 18 μA respectively. Elastic peaks have been normalized to unity. After background subtraction, as shown in Figure 5.26(b), the main two energy loss peaks, 6 eV (π plasmon) and 26 eV (σ plasmon), can be seen clearly. The intensities of π plasmon and σ plasmon peaks are not changed within these tip bias voltage ranges, as expected for two inelastic scattered peaks.

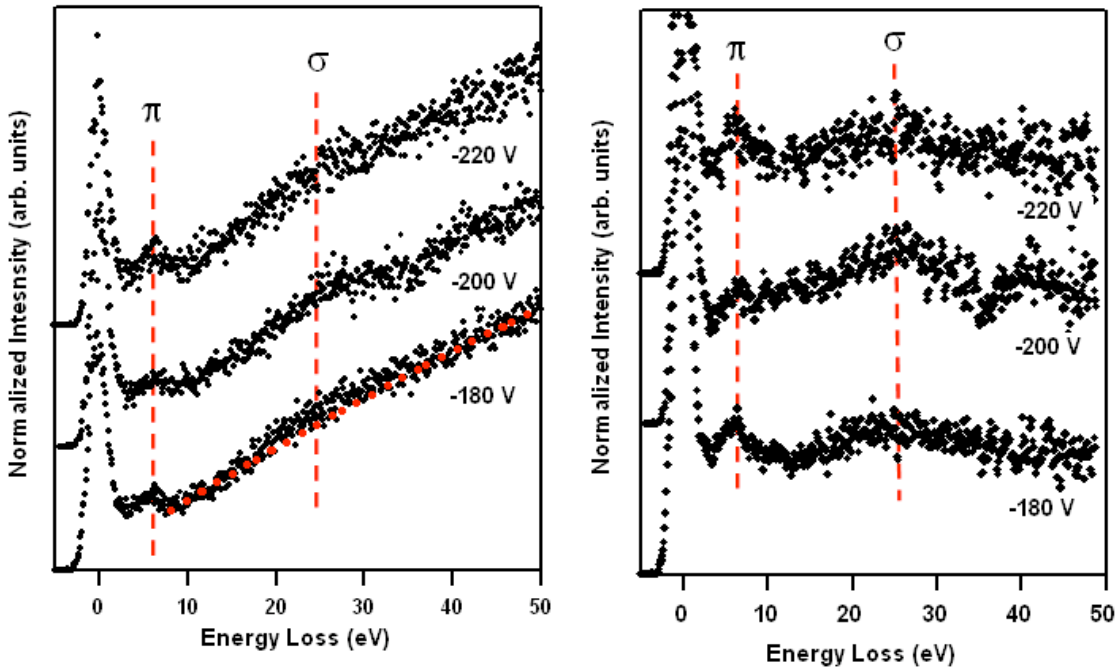

Figure 5.26: SPELS spectra of graphite taken with co-axial silicon tip. A positive bias was applied to the lens (Lens 1). (a) The tip–sample working distance was fixed at 250 nm. The tip bias voltages used were –180V, –200V, and –220V, and the corresponding field emission currents were 5.5 μA, 12 μA, and 18 μA, respectively. The background is indicated by red dotted lines at –180V. (b) After subtraction of the background.

Second, the grounded lenses are labelled "Lens 2". Figure 5.27 shows a SPELS full range spectrum of graphite taken with a co-axial silicon tip. The tip bias voltage is –250 V, the field emission current is 14 μA, and the tip-sample distance is 220 nm.

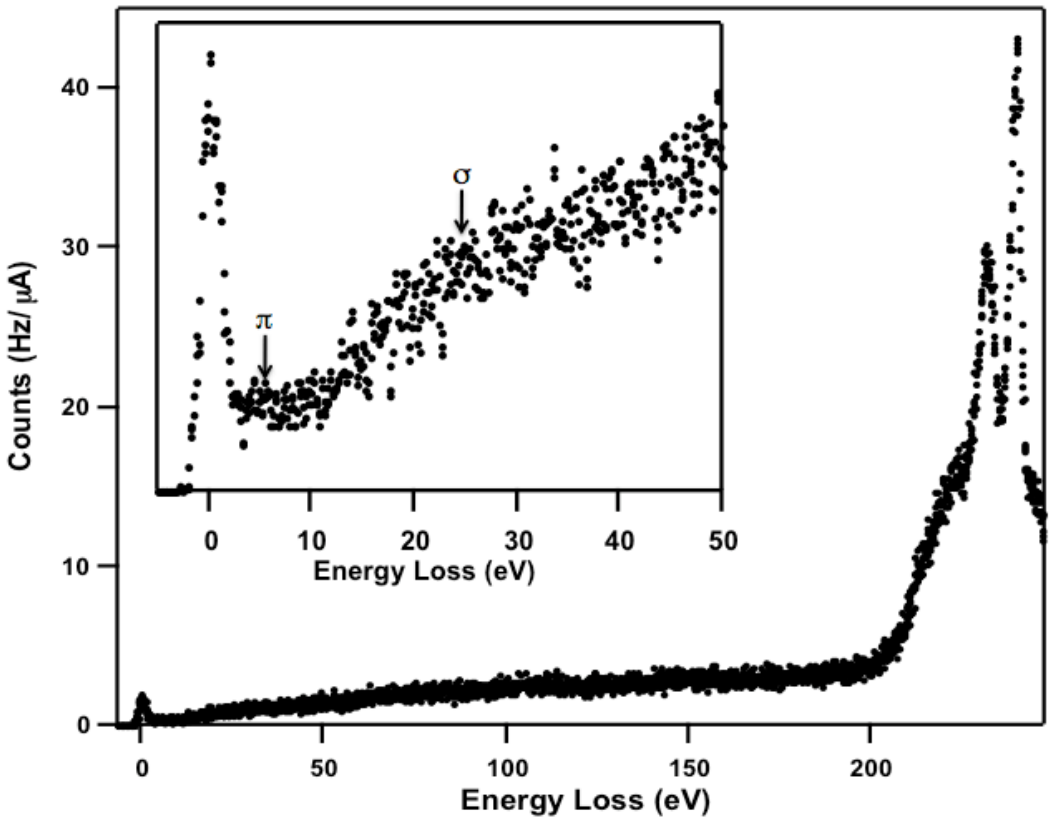

Figure 5.27: SPELS spectrum of graphite taken with a co-axial silicon tip. The tip bias voltage is –250 V, the field emission current is 14 μA, and the tip–sample distance is 220 nm. The lens is grounded (Lens 2). The inset shows a highlight of the low energy loss region.

This spectrum also has a relatively large SEE peak as well as a very small elastic peak and plasmon peaks similar to those shown in Figure 5.24. The inset shows that a π plasmon (6 eV) and a σ plasmon (26 eV) peak were observed. However, the SEE peaks shown clearly comprise three peaks compared to the spectrum (Lens 1, Figure 5.23(a)). Table 5.4 compares the intensity of spectra between Lens 1 and Lens 2. Both spectra were taken with the same co-axial silicon tip. The intensity of the SEE peak in Lens 2 is

over 45 times stronger than that of the SEE peak in Lens 1. The spectrum without the lens effect (Lens 2) shows a very low count rate, for example, the intensity of the elastic peak is 1.87 Hz/μA, so the lens in an analyser can be helpful to improve the intensity of the spectrum.

The detail of low kinetic energy of the graphite spectrum with Lens 1 and Lens 2 is shown in Figure 5.28. When positive potential is applied to the lens (Lens 1), electrons are more focused on the entrance slit in a hemispherical analyser. The analyser may detect wide angular distribution of secondary electrons (low kinetic energy region). It thus represents the broad SEE peaks. On the other hand, when the lens is grounded (Lens 2), electrons are not focused on the entrance slit so fewer electrons may pass through the entrance slit. The analyser thus detects a narrow angular distribution of secondary electrons. It represents sharp SEE peaks.

Table 5.4: Intensity of SPELS spectrum of graphite taken with a co-axial silicon tip

	Elastic peak (Hz/μA)	Secondary electron peak (Max.) (Hz/μA)
Lens 1 (Figure 5.22)	65	1967.8
Lens 2 (Figure 5.25)	1.87	42.85

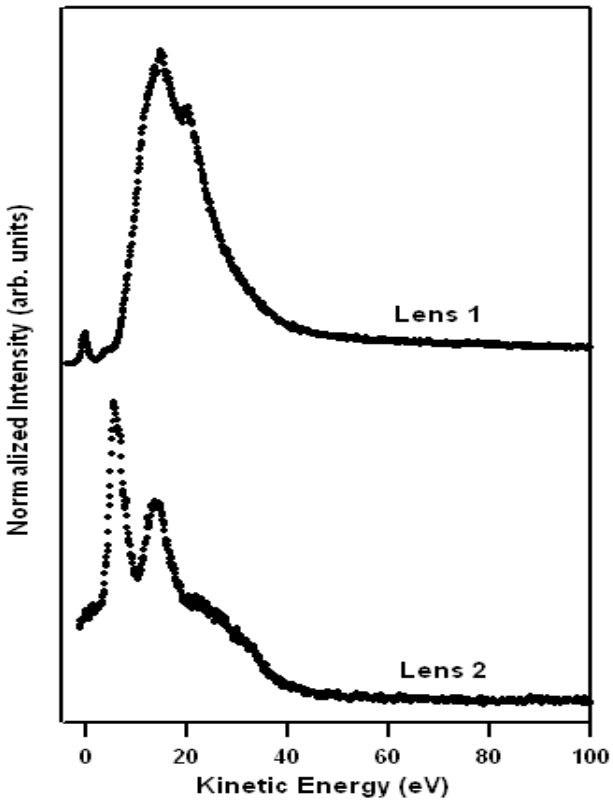

Figure 5.28: Detail of low kinetic energy of graphite spectrum taken with co-axial silicon tip. The tip bias voltage and tip–sample distance are, respectively, –200 V and 250 nm for Lens 1 and –250 V and 200 nm for Lens 2.

5.3.3 SPELS Spectra of Graphite using a Tungsten Tip

Normal chemically etched tungsten tips were also investigated for SPELS as a reference. The microfabricated silicon tip was tested for the first time in SPELS through this project so the SPELS spectra taken from silicon tips must be compared with a spectrum that is obtained from a standard tungsten tip. The electrostatic lenses (Lens 1 and Lens 2) are also investigated in the SPELS spectrum.

Figure 5.29(a) shows a typical SPELS spectrum of graphite taken with a tungsten tip and a positive potential applied to the lens (Lens 1). The tip bias voltage, field emission currents, and tip-sample distance are –130 V, 3 μA, and 600 nm respectively.

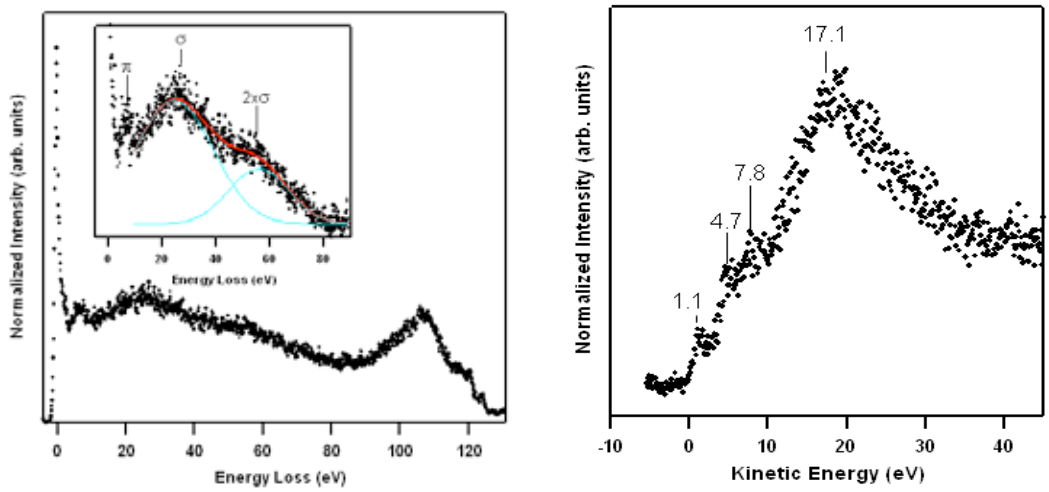

(a) (b)

Figure 5.29: SPELS spectrum of graphite taken with a tungsten tip. A positive bias was applied to the lens (Lens 1). The tip bias voltage is –130 V, the field emission current is 3 μA, and the tip–sample distance is 600 nm. (a) Full range spectrum; the inset shows a highlight of the low energy loss region. (b) Detail of the low kinetic energy region in Figure 5.29(a).

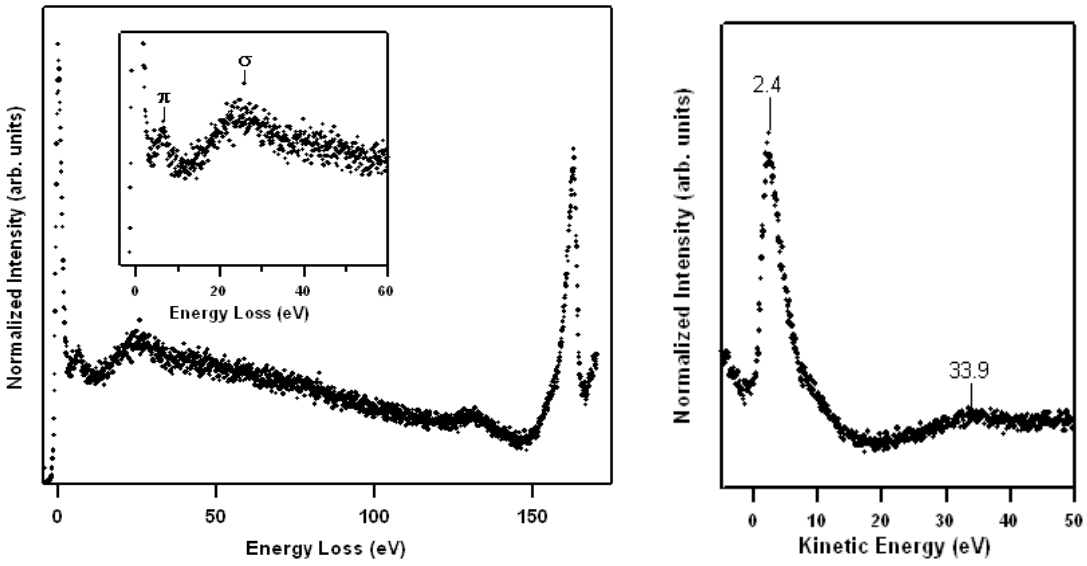

(a) (b)

Figure 5.30: SPELS spectra of graphite taken with a tungsten tip. The lens is grounded (Lens 2). The tip bias voltage is –170 V, the field emission current is 29 μA, and the tip–sample distance is 625 nm. (a) Full range spectrum; the inset shows a highlight of the low energy loss region. (b) Detail of the low kinetic energy region in Figure 5.30(a).

The spectrum shows an elastic peak with π (6 eV) and σ (26 eV) plasmon peaks , while double σ plasmon (52 eV) peaks and an SEE peak are observed. The 52 eV peak is reported in a previous SPELS spectrum of graphite and EELS [13, 114, 115] and is caused by a double σ plasmon loss. Figure 5.29(b) presents the SEE peak in a low kinetic energy region in Figure 5.29(a), and kinetic energy of 17.1 eV, 7.8 eV, 4.7 eV, and 1.1 eV are observed.

Figure 5.30(a) also presents the spectrum of graphite taken with a tungsten tip, but the lens is grounded (Lens 2). The tip bias voltage, field emission current, and tip–sample distance are –170 V, 29 μA, and 625 nm respectively. The spectrum shows an elastic peak, π (6 eV), σ plasmon peak (26 eV), and an SEE peak. Figure 5.30(b) shows the SEE peaks at 2.4 eV and 33.9 eV (in kinetic energy). The low kinetic energy region (2.4 eV) is known as the "cascade" peak, as it results from multiple processes of an incident electron beam interaction in the solid [110, 116].

Table 5.5 summarizes the SPELS spectrum of graphite with Lens 1 (Figure 5.29) and Lens 2 (Figure 5.30) systems. The count rate of the elastic peak in Lens 1 (Figure 5.29) is also three times higher than that in Lens 2 (Figure 5.30) as explained in Section 5.3.2. This is why we see the more detailed plasmon feature (e.g. 52 eV) in Lens 1. The SEE peaks are found to be very different, as we expected. In Lens 1, a broad SEE peak is seen, as shown in Figure 5.29(b), and it also gives an extra feature as it results from wide angular distribution in a lens. However, in Lens 2 (Figure 5.30(b)), the narrow SEE peak is seen, as shown in Figure 5.30(b), as it results from narrow angular distribution in a lens. The tungsten tip is not shielded so the SEE peaks are observed to be weaker than the elastic peak like that in the SPELS spectrum taken with the Au coated silicon tip. The negative biased tip bends the "specular" electrons to the

surface so the elastic peak and energy loss features are observed to have a relatively strong signal compared to the SEE peaks.

Table 5.5: Comparison of SPELS spectra of graphite taken with a tungsten tip

	Lens 1 (Figure 5.29)	Lens 2 (Figure 5.30)
Count rate (Hz) of an elastic peak	1014.72 Hz	320.56 Hz
Plasmon peak (Energy loss peak)	π, σ, $2 \times \sigma$	π, σ
SEE peak (Kinetic energy peak)	1.1 eV, 4.7 eV, 7.8 eV, and 17.1 eV	2.4 eV and 33.9 eV

Figure 5.31(a) shows SPELS spectra of graphite at a fixed working distance of 625 nm. Tip voltage biases of –110 V, –150 V, and –170 V are shown, corresponding to field emission currents of 7.9 μA, 14 μA, and 29 μA, respectively. The electrostatic lens is grounded (Lens 2) and elastic peaks have been normalized to unity. Increasing the tip bias voltage gives a stronger σ plasmon feature as shown in Figure 5.31(b). Figure 5.31(b) presents the relative σ/π plasmon intensity as a function of tip bias voltage and the intensities of the π and σ plasmons are almost equal at –160 V; this feature has similar behaviour to spectra taken with an Au coated silicon tip (Figure 5.23(b)).

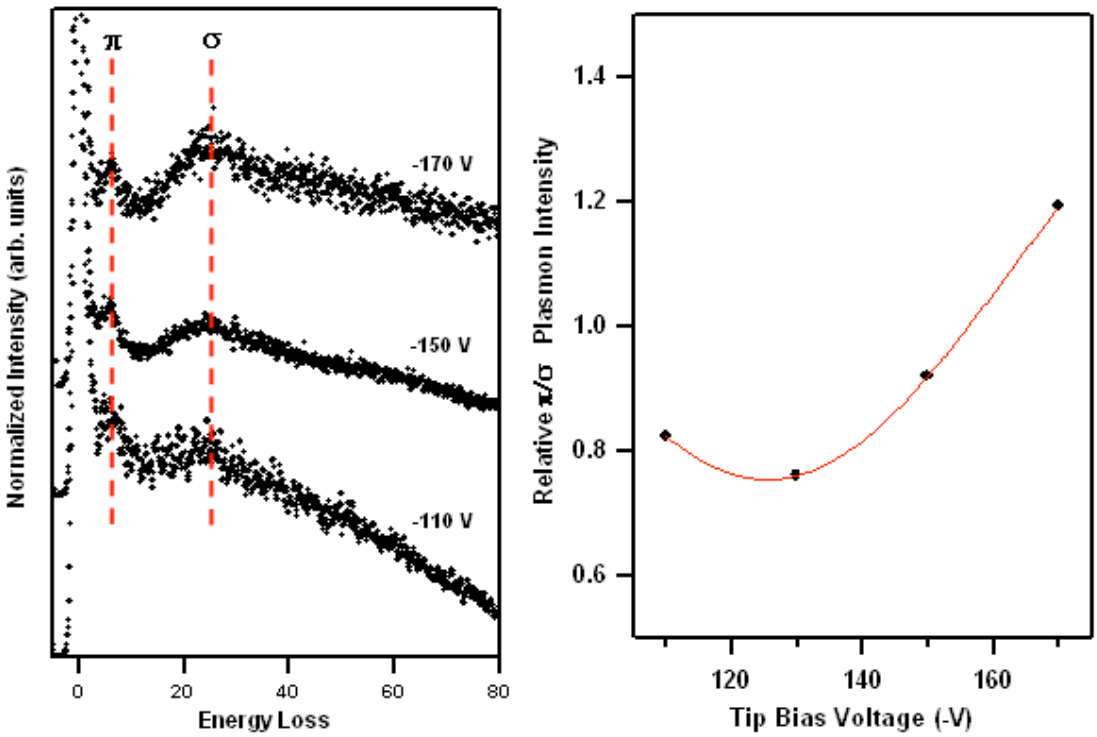

Figure 5.31: The variation in graphite spectra taken with (a) different tip bias voltages and (b) relative $\frac{\sigma}{\pi}$ plasmon intensity as a function of a tip bias voltage. The lens is grounded (Lens 2). The tip–sample working distance was fixed at 625 nm. Each spectrum is normalized to the intensity of its elastic peak.

5.3.4 Secondary Electron Emission

All SPELS spectra of graphite have shown different secondary electron emission (SEE) peaks and here we shall discuss the SEE peaks in the SPELS spectrum. The electronic band structure of unoccupied states of graphite was widely studied from SEE spectra [117]. Recently, Yin *et al.* obtained the SPELS-SEE spectra of graphite taken with a tungsten tip and 17.5 eV, 11.5 eV, 2 eV, and 6 eV kinetic energy peaks are assigned to the σ^* conduction band (Γ_4^-), σ^* conduction band (Γ_4^-, Γ_1^+), σ^* conduction band ($\Gamma_6^-, \Gamma_5^+, \Gamma_1^+$), and π^* conduction band (Γ_3^+, Γ_2^-) respectively [15]. Lawton *et al.* also presented local SPELS-SEE spectra of graphite at a tip–sample distance of only 50 nm [117].

The SEE spectra of graphite taken with microfabricated silicon tips are shown in Figure 5.32(a), (b), and (c); they are also taken from Figure 5.21(b), 5.24(a), and 5.27(a) in order to compare an Au coated silicon tip and a co-axial silicon tip. These peaks are normalized to the maximum SEE peak of each spectrum.

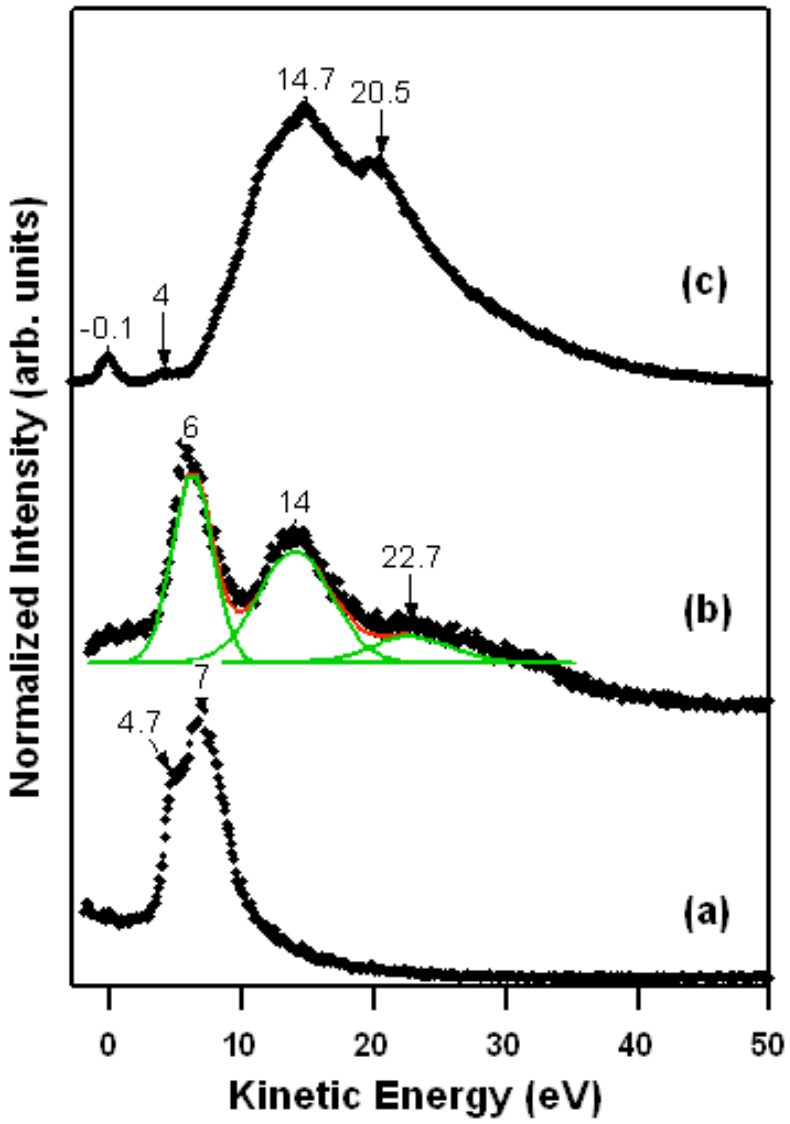

Figure 5.32: Secondary electron emission (SEE) SPELS spectra of graphite taken with different types of microfabricated silicon tips. The types of tips, incident energies, and working distances are, respectively, as follows: (a) Au coated silicon tip, –180 V, 638 nm (b) co-axial silicon tip (without lens), –250 V, 220 nm, and (c) co-axial silicon tip (with lens), –200 V, 250 nm. The maximum SEE peaks have been normalized to unity.

Figure 5.32(a) was taken from an Au coated silicon tip which is not grounded, and a strong peak at 7 eV and a small shoulder at 4.7 eV can be seen. SEE spectra taken with a co-axial silicon tip show peaks in different positions as seen in Figure 5.32(b) and (c). Figure 5.32(b) was taken with a co-axial silicon tip and the lens is grounded (Lens 2). SEE spectra clearly show three peaks at 6 eV, 14 eV, and 22.7 eV. On the other hand, SEE spectra taken with a co-axial silicon tip where positive potential was applied to the lens (Lens 1) show strong intensity of peak at 14.7 eV and weak shoulders at 20.5 eV. Table 5.6 summarizes the assignments of peaks observed in SPELS secondary electron emission spectra of graphite taken with microfabricated silicon tips as well as with a normal tungsten tip. The band structure of graphite has been studied by many authors and the band structure of graphite calculated by Holzwarth *et al.* [118] and Tatar *et al.* [119] is chosen to assign the SEE peaks in this work. Figure 5.33 shows the band structure of three-dimensional graphite calculated by Tatar *et al.* [119] and the Brillouin zone centre (Γ) and zone edge (M) of graphite are represented in Figure 5.33. Most of the SEE features seen are due to electrons coming from the centre of the Brillouin zone (Γ) as shown in previous SPELS results [15, 116]. Emitted SEE electrons from the zone centre (Γ) leave perpendicular to the surface and can be suppressed by the electric field so that the analyser detects the electrons. The SEE peaks in Figure 5.32(a) (Au coated silicon tip) also appear to come from the zone centre (Γ). The SEE peaks taken from the tungsten tip are also represented in Table 5.6. The main feature at 17 eV is the same as observed in previous work [15], but other peaks at 1.1 eV, 4.7 eV, and 7.8 eV are found to be different from those observed in previous work. In previous work, the hemispherical analyser was set 7^{o} from the surface but we collect the spectra parallel to the surface in this work. Those peaks also came from the zone centre (Γ) and all of these spectra were taken with non-shielded tips.

However, SPELS-SEE spectra of graphite taken with a co-axial silicon tip which has the outer layer grounded are presented in Figure 5.32(b) where positive potential is not applied to the lens and in Figure 5.31(c) with positive potential applied to the lens. The 14 eV peak appears to come from an unoccupied σ state at zone edge (M) as shown in Figure 5.33. This peak was not observed in SPELS-SEE spectra taken with a non-shielded tip but the 14 eV peak was observed by angle-resolved secondary electron emission [120].

Table 5.6: Assignments of peaks observed in a secondary electron emission of graphite

Band Assignment	Experimental (eV, in Figure 5.32)	Theory (eV)
Co-axial Si tip		
$\pi(\Gamma_3^+)^{a,b}/\sigma(M_5^+,M_6^-)^a$	6	5.8(Γ)[a]/6.3(M)[a]
$\sigma(M_3^-,M_4^+)^b$	14 14.7	14(M)[b]
$\sigma(\Gamma_1^+)^b/\pi(M_2^+)^b$	20.5	20.6(Γ)[b]/20.5(M)[b]
$\pi(\Gamma_2^-)^b/\pi(M_4^-)^b$	22.7	22(Γ)[b]/22.8(M)[b]
Au coated Si tip		
$\sigma(\Gamma_5^+,\Gamma_6^-)^a$	4.7	4.8[a]
$\pi(\Gamma_3^+)^b$	7	7.0[b]

Tungsten tip			
Band Assignment	Experimental (eV, in Figure 5.29)	Previous Work [15]	Theory (eV)
$\sigma(\Gamma_1^+)^a$	1.1		0.9[a]
$\sigma(\Gamma_5^+,\Gamma_6^-,\Gamma_1^+)^b$		2.0	3.0[b]
$\sigma(\Gamma_5^+,\Gamma_6^-)^a$	4.7		4.8[a]
$\pi(\Gamma_3^+)^{a,b}$		6.0	5.8[a]
$\pi(\Gamma_3^+)^b$	7.8		7.0[b]
π^c		11.5	NA
$\sigma(\Gamma_4^-)^b$	17.1	17.5	17.0[b]

(a) Reference [118]
(b) Reference [119]
(c) Reference [121]

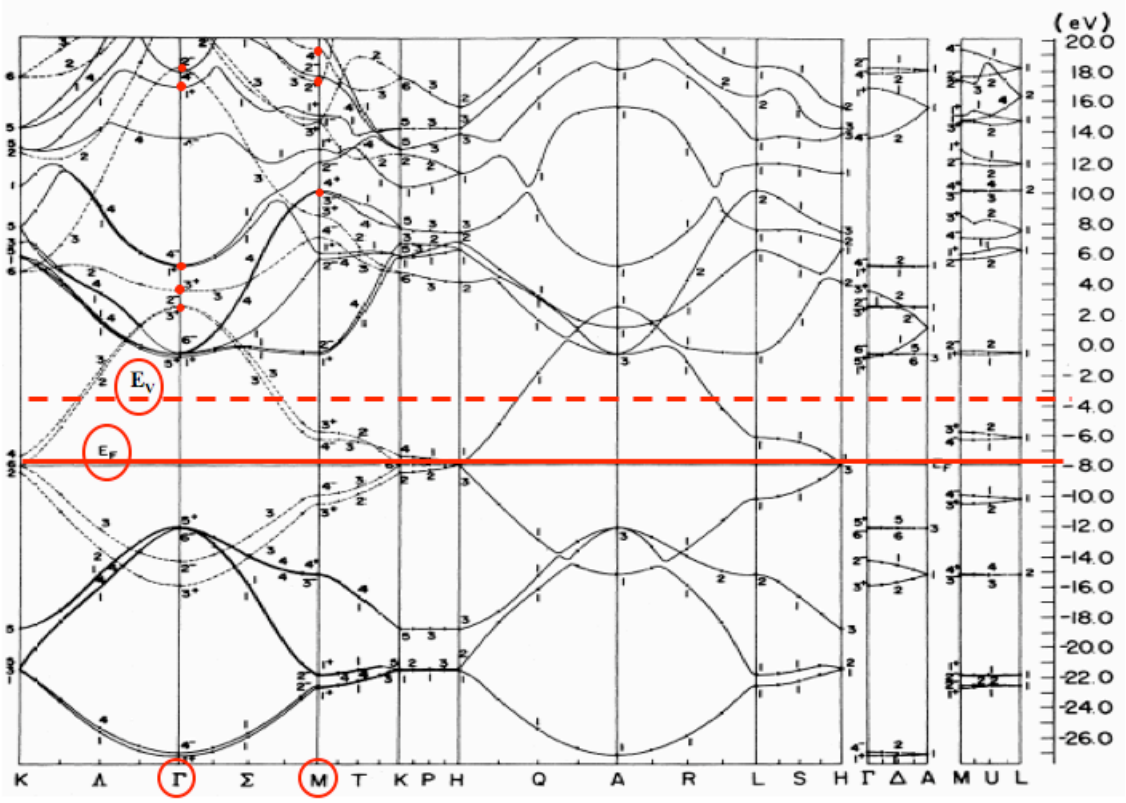

Figure 5.33: Band structure of three-dimensional graphite. From [120]. The red dots represent data collected from SPELS.

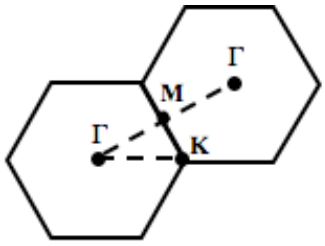

Figure 5.34: Brillouin zone (Γ, M) of graphite for a single layer. Γ is a zone centre and M is a zone edge.

Another interesting feature of spectra taken with a co-axial silicon tip is that strong SEE peaks are observed compared with elastic peaks. Figure 5.35 shows that the ratio between SEE peaks and elastic peaks depends on the tip bias voltage. Figure 5.35(a), (b), and (c) used an Au coated silicon tip, co-axial silicon tip without lens (Lens 2), and co-axial tip with lens (Lens 1) respectively. The ratios between SEE and elastic peaks in Figure 5.35(a), (b), and (c) are 3.2, 10.134, and 28.512 respectively at –200V. When positive potential is applied to the lens (Lens 1, Figure 5.35(a)), electrons are collected with a wide angular distribution as shown in Figure 5.28. The ratio (SEE/elastic) of a co-axial silicon tip (Figure 5.35(c), Lens 1) is found to be 2.5 times higher than that of a co-axial silicon tip (Figure 5.35(b), Lens 2). A co-axial silicon tip (Figure 5.35(c)) has also shown a more than nine-fold increase in the ratio (SEE/elastic peak) compared to the Au coated silicon tip (Figure 5.35(a)).

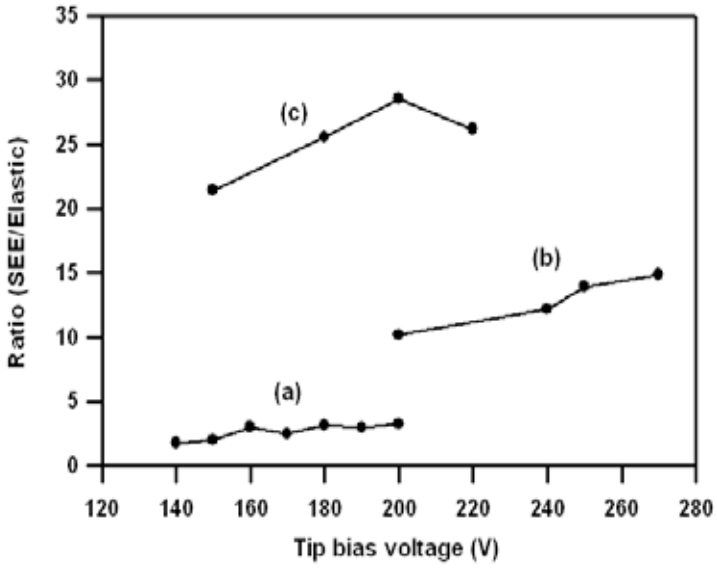

Figure 5.35: The ratio between SEE peaks and elastic peaks depends on tip bias voltage. The types of tips and tip–sample working distances are, respectively, as follows: (a) Au coated silicon tip, 400 nm (without lens, Lens 2), (b) co-axial silicon tip (without lens, Lens 2), 220 nm, and (c) co-axial silicon tip (with lens effect, Lens 1), 250 nm.

The proposed trajectories of SEEs are shown in Figure 5.36. Electrons are incident to the surface following the electric field line (Figure 5.36(a)). The incident electrons hit the surface and generate backscattered electrons (e.g. elastic and energy loss peaks) or secondary electrons. These electrons come out from the surface with the electric field (Figure 5.36(b)). Figure 5.36(c) shows the secondary electrons. SEEs are emitted from the Brillioun zone centre (Γ) and zone edge (M). The SEEs may emit the following local electric field, which is shown by a blue line in Figure 5.36(c). When a non-shielded tip is used, secondary electrons are emitted following a further long-range electric field. The long-range electric field can be affected by the electric field from the non-shielded tip. Secondary electrons from the zone edge (M) thus have more chance to bend to the surface and most secondary electrons from the zone centre (Γ) will collect at the analyser.

However, when a shielded tip (co-axial silicon tip) is used, the local electric field is still affected by the electric field in the tip region, but the long-range electric field is screened. Secondary electrons are thus able to escape from the tip region and collect the electrons from the zone centre (Γ) as well as the zone edge (M). This also gives relatively higher intensity of SEE/elastic as shown in Figure 5.35(b) and (c) compared with a non-shield tip (Figure 5.35(a)).

When we use the grounded tip in order to reduce the electric field effect between tip and surface, electrons can escape from the tip region. Therefore, the grounded tip (e.g. the co-axial silicon tip) will benefit from angular resolved SPELS because the long-range electric field is screened from the electric field.

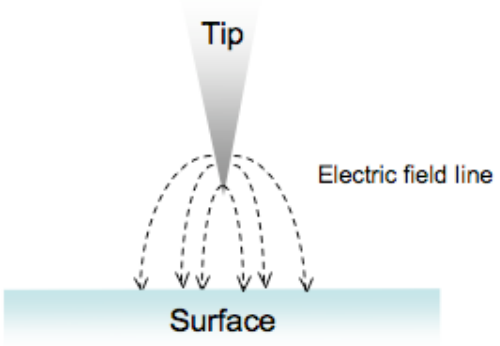

(a) Electrons are incident to the surface following the electric field line.

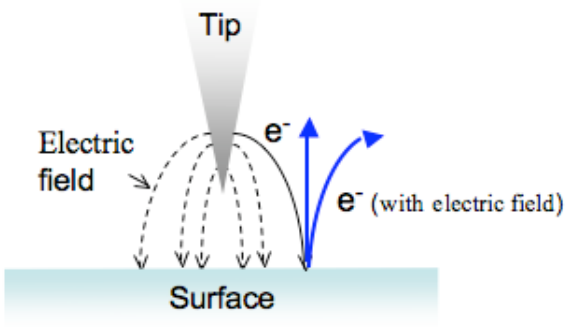

(b) Electrons are emitted and scattered with the electric field.

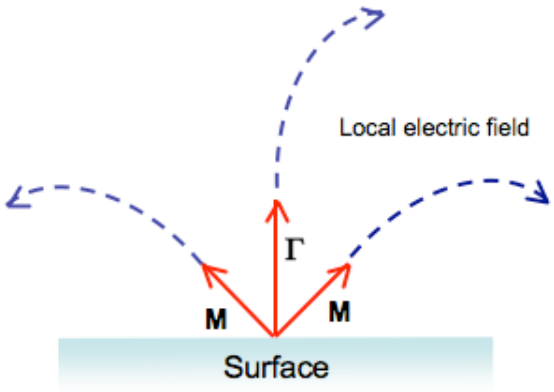

(c) Secondary electrons are emitted from the Brillouin zone centre (Γ) and zone edge (M). The local electric field is shown by blue lines.

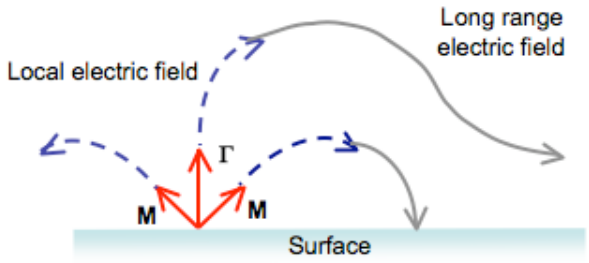

(d) Non-shielded tip. The local electric field and long range electric field are bent by the electric field line. Secondary electrons from the zone edge (M) have more chance to bend to the surface and most secondary electrons from the zone centre (Γ) will collect at the analyser.

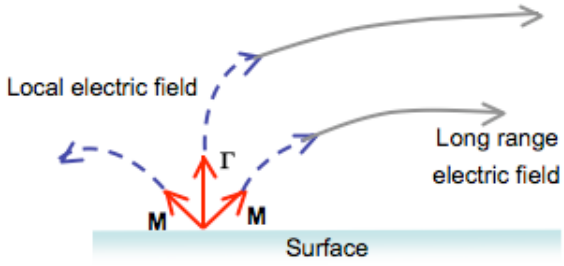

(e) Co-axial tip. The local electric field is affected by the electric field line but the long-range electric field is screened. Secondary electrons are able to escape from the tip region.

Figure 5.36: Schematic diagram of secondary electron trajectories.

5.3.5 Advantages of Microfabricated Co-axial Silicon Tip

In the field of scanning probe microscopy, the probe is usually the most important part; this is also the case with the SPELS instrument. The features of SPELS spectra can be affected greatly by the tips used. We have investigated tips for SPELS using microfabrication techniques and it was successfully demonstrated. Here are summarized advantages of microfabricated co-axial silicon tip for SPELS.

In our current SPELS system, the hemispherical analyser is fixed parallel to the surface. In the non-shielded tip case, the backscattered electrons are suppressed by the electric field so that the hemispherical analyser can collect most backscattered electrons.

The SPELS spectrum of graphite taken with non-shielded tip was thus clearly represented the σ (6 eV) and π (26 eV) plasmon peaks as shown in Figure 5.20. The SEE peaks of graphite was represented from the Brillouin zone center (Γ).

In the shielded tip (co-axial silicon tip) case; the majority electric fields are shielded so the backscattered electrons may scattered. The hemispherical analyser can collect some of backscattered electrons and it gave relatively low intensity of plasmon peaks. However, SPELS spectrum of graphite taken with a co-axial silicon tip was shown the σ (6 eV) and π (26 eV) plasmon peaks and 44 eV for non-vertical interband transition peak (Figure 5.24). SEE peaks of graphite taken with a co-axial silicon tip were also detected from the Brillouin zone center (Γ) as well as zone edge (M) (Table 5.6). Therefore, co-axial tip allows detecting more information of SPELS spectrum comparing SPELS spectrum taken with a non co-axial tip as shown the 44 eV of non-vertical interband transition peak and SEE peaks from the Brillouin zone edge (M). This shows also the potential of angular measurement in a SPELS and it may be allow k-resolved spectra.

Chapter Six

Summary and Future Work

The aim of this work is to produce specially designed microfabricated silicon tips for scanning probe microscopy (SPM). Several types of silicon-based tips were fabricated and these tips were successfully demonstrated in scanning tunnelling microscopy (STM) and scanning probe energy loss spectroscopy (SPELS). In SPELS especially, the co-axial silicon tip has successfully screened the electric field between tip and sample and SPELS spectra of graphite are compared for a shielded tip (co-axial silicon tip) and a non-shielded tip (Au coated silicon tip). In this chapter, the results are summarized and suggested routes for future development are discussed.

6.1 Summary

Three different types of silicon tips were produced using a microfabrication technique. First, Au coated silicon tips are applied to STM. In order to prevent inadvertent contact between the substrate bearing tip and the sample being probed, the tip is elevated on a mesa structure over 100 μm in height above the silicon substrate, and new fabrication schemes for producing silicon tips onto a higher mesa structure were introduced. A silicon tip apex of 10~20 nm has been found to be sharper than a chemically etched tungsten tip. Etching parameters were optimized to produce curved sidewalls of the mesa structure for additional metallization. The completed single structure of the Au coated silicon tip was demonstrated to have features that give it potential for use as an STM probe. An atomic resolution STM image of graphite has been obtained and the STM images of superlattice on graphite and clusters were also successfully obtained using an Au coated silicon tip. These results demonstrated that the silicon tip on a mesa structure has sufficiently good performance to be used as an STM probe.

Second, the Au cathode co-axial silicon tip was designed and fabricated for SPELS. The Au cathode co-axial silicon tip consists of a Si/Au/HfO_2/Au. The inner Au layer is used as a field emitting layer and the outer Au layer is grounded to reduce the electric field between tip and substrate. The enhanced field emission properties and more stable field emission current achieved in an Au cathode co-axial silicon tip are comparable to those of standard tungsten tips. This means that Au cathode co-axial silicon tips have the potential to be used as a probe in a SPELS. The SPELS spectra of graphite taken with an Au cathode co-axial silicon tip were successfully obtained for the first time. This grounded Au cathode co-axial silicon tip detected the weak intensity of an elastic peak, π (6 eV), σ (~ 26 eV) plasmon peaks, and a 43 eV plasmon peak, and the strong intensity of a secondary electron emission peak. The long-range electric field

is screened so more emitted secondary electrons arrive at the analyser. This may give a relatively higher intensity of secondary electrons, and SEE peaks are assigned to the Brillouin zone edge (M) as well as the zone centre (Γ).

The electrostatic lens effects are also studied. The electrons arrive at the hemispherical analyser via the lens. In this study, SPELS spectra of graphite are used with both a biased lens and a grounded lens. When positive potential is applied to the lens, wide angular distributed electrons are detected at the analyser so the SEE peaks are found to be broad peaks. On the other hand, when the lens is grounded, narrow angular distributed electrons arrive at the analyser, giving narrow and sharp peaks.

The SPELS spectra of graphite taken with a non-grounded Au coated silicon tip were also investigated, with a normal tungsten tip used as a reference. The elastic peak, π and σ plasmon peaks, and weak secondary electron emission peaks were observed. The long-range electric field may be suppressed by the electric field from the tip so the SEEs from the zone edge (M) have more chance to be suppressed at the surface. The SEE peaks are seen to be a relatively weak feature and the SEEs are thus coming from the Brillouin zone centre (Γ). Therefore, the Au cathode co-axial silicon tip significantly reduced the electric field effect successfully. This shows that SPELS will be able to allow *k*-resolved spectra in the future.

Third, the multilayered silicon tip was applied to the scanning probe electron analyser (SPEAR). SPEAR is a new type of electron analyser and it requires a multi-layered tip to detect the photoelectrons. The structure of the multilayered silicon tip consists of Si/thermally oxidized SiO_2/Au/sputtered SiO_2 /Au. The inner silicon layer and the third and fifth Au layers are used as an electron collector, a retarding field analyser, and a grounded layer respectively. Each layer has completed electrical connections, which comprise a total of three electrical connections in a SPEAR tip. This

well-structured complicated five layered silicon tip was successfully fabricated with three electrical connections onto a specially designed tip holder.

6.2 Future Work

The potential of silicon tips for STM has been investigated in this thesis. Microfabrication of silicon tips was also successfully demonstrated in a UHV STM as well as SPELS for the first time. Here further improvements for SPELS are suggested.

One of the most important issues is a field emission tip in a SPELS. In Chapter Five, an Au coating layer was shown to have a field emission current comparable to that of a normal tungsten tip. However, it still requires a tip bias voltage over –100 V to generate backscattered electrons. In order to improve the spatial resolution of SPELS, enhanced field emission currents at low incident energy are required. Carbon nanotube (CNT) has been suggested as a good field emitter due to its semiconducting as well as metallic properties. Well aligned CNTs are widely studied for these purposes [122]. However it is still difficult to grow single CNT on a substrate or the apex of a tip and it cannot make a co-axial structure. An alternative method is to choose a coating layer on the apex of the silicon tip. Undoped diamond might be a good material to use as a coating layer. Zhu *et al.* reported that undoped diamond has shown a strong and sustained electron emission and the emitters produce 10 mA/cm^2 (at the sample) at applied fields of 3 to 5 V/μm [123]. These values are the lowest fields for any field-emitting materials, which indicates that undoped diamond might be a potential candidate material to be used as a field-emitting layer for SPELS. A low applied field is also able to avoid breakdown of the tip. In a fabrication process, the undoped diamond layer was prepared by chemical vapour deposition and the surface was treated by hydrogen plasma. This process can easily control the properties of the emitting layer.

With regard to the geometry aspect, the size of the silicon substrate and the location of the silicon tip are important parameters in obtaining SPELS spectra because the silicon substrate can block the backscattered electrons. For this reason, the size of the silicon tip is 2 × 2 mm square, which is the minimum size cut by hand, and the silicon tip was located on the edge of the silicon substrate. However, further improvements to the structure need to be performed for commercial SPELS purposes. Figure 6.1 shows the silicon tip on a silicon substrate. The height of a silicon tip is approximately 230 μm and the width of the silicon substrate is around 500 μm. The dicing saw had to be used to fabricate the silicon tip without a wide silicon substrate. If silicon tips are fabricated without a wide silicon substrate around the tip as shown in Figure 6.1, the silicon substrate might not affect the backscattering electrons.

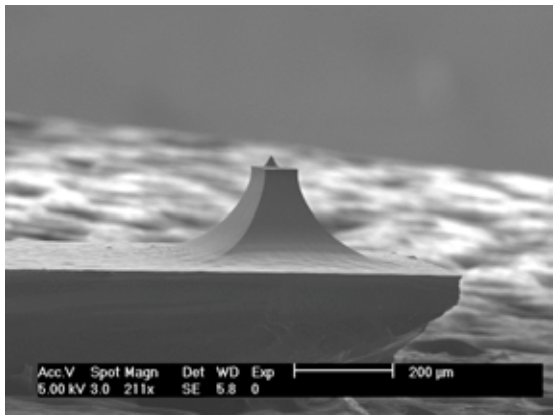

Figure 6.1: SEM image of a silicon tip. The height of the silicon tip is approximately 230 μm and the width of the silicon substrate is around 500 μm.

Co-axial tungsten tips also have potential applications in SPELS. A chemically etched tungsten tip is easy to etch and it is not necessary to use expensive equipments such as e-beam lithography, dry etching, and so on. A glass coated tungsten tip or hand painted tungsten tip has already been suggested to make a grounded layer but these do not properly shielded the electric fields. The suggested structure of a co-axial tungsten

tip is a tungsten/HfO_2/metal layer. The metal sputtering techniques can be used to produce a co-axial tungsten tip and the apex of the tip can then be etched using an etchant solution. The fabrication scheme of the co-axial tungsten tip is simple compared with that of an Au cathode co-axial silicon tip. The co-axial tungsten tip will also allow easy handling so this co-axial tungsten tip would be a good candidate for SPELS.

The SPELS instrument could be developed to improve electron collection. In current SPELS systems, the hemispherical analyser is used to collect backscattered electrons. The hemispherical analyser is not an ideal analyser to collect the electrons. The higher efficiency of an electron analyser should be considered. Zhou *et al.* reported the use of a toroidal electron energy spectrometer for surface analysis [69] as shown in Figure 6.2.

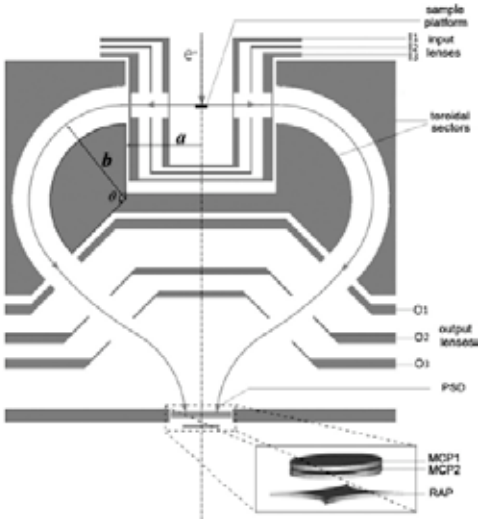

Figure 6.2: Cross-section of a toroidal electron energy analyser. The scattered electrons will be detected in microchannel plates. From [69]

This toroidal electron energy spectrometer can detect electrons in a wide azimuth angle range of 245°, so the electrons are collected with an azimuth angle from the surface. In a conventional electron analyser, electrons are detected in one way, indicating that the analyser might be losing most of the electrons. The electron count

rate obtained with a toroidal electron energy spectrometer was 50 times higher than that obtained by the conventional electrostatic analyser.

A multichannel detector can also improve the electron count rate. Electrons are detected by multichannel plates and this will also reduce the time taken to collect spectra. If the electron analyser can collect electrons more efficiently, a much reduced tip bias voltage is able to obtain SPELS spectra. The electric field on the tip apex can be reduced at the lower tip bias voltage while operating SPELS, so the apex will not be damaged within a distance of a few nanometres. This will contribute to an improvement of the spatial resolution as well as the scanning electron energy loss spectroscopy in a SPELS.

References

[1] A.L.M.Reddy, M.M.Shaijumon, S.R. Gowda and P.M. Ajayan, *Nano Lett.* **9** (2009) 1002.

[2] International Technology Roadmap for Semiconductors, http://www.itrs.net/

[3] M.M.Bailey and C.J.Berkland, *Med. Res. Rev.* **29** (2009) 196.

[4] P. Balaya, *Energy and Environ. Sci*. **1** (2008) 645.

[5] G. Binnig, H. Rohrer, Ch. Garber and E. Weibel, *Phys. Rev. Lett*. **49** (1982) 57.

[6] G. Binnig and H. Rohrer, *Helv. Phys. Acta* **55** (1982) 726.

[7] J. Loos, *Adv. Mater*. **17** (2005) 1821.

[8] J.V.Lauritsen and F. Besenbacher, *Adv. Catal.* **50** (2006) 97.

[9] D.M. Eigler and E.K. Schweizer, *Nature* **344** (1990) 524.

[10] R.E. Palmer, B.J. Eves, F. Festy and K. Svensson, *Surf. Sci.* **502** (2002) 224.

[11] F. Festy and R.E. Palmer, *Appl. Phys. Lett.* **85** (2004) 5034.

[12] F. Festy, K. Sevensson, P. Laitenberger and R.E. Palmer*, J. Phys. D* **34** (2001) 1849.

[13] B.J. Eves, F. Festy, K. Svensson and R.E. Palmer, *Appl. Phys. Lett*. **77** (2000) 4223.

[14] A. Pulisciano, S.J. Park and R.E. Palmer, *Appl. Phys. Lett.* **93** (2008) 213109.

[15] J. Yin, A. Pulisciano and R.E. Palmer, *Small* **2** (2006) 744.

[16] Nanoworld, http://www.nanoworld.com

[17] M. Bale and R.E. Palmer, *J. Vac. Sci. Technol. B* **20** (2002) 364.

[18] Y. Wang, C.A. Paulson, G. Ning and D.W. Weide, *IEEE* (2005) 2147.

[19] M.T. Azar and Y. Wang, *IEEE Trans. Microw. Theory Tech.* **52** (2004) 971.

[20] C. Mihalcea, S.S. Werner, S. Műnster, E. Oesterschulze and R.Kassing, *Appl. Phys. Lett.* **68** (1996) 3531.

[21] V. Lulevich and W.A. Ducker, *Appl. Phys. Lett*. **87** (2005) 214107.

[22] W. Noell, M. Abraham, W. Ehrfeld, M. Lacker and K. Mayer, *J. Micromech. Microeng.* **8** (1998) 111.

[23] C. Choi and C. Kim, *Nanotechnology* **17** (2006) 5326.

[24] N. Wike, C. Hibert, J. O'Brien and A. Morrissey, *Sens. Actuators A-Phys.* **123-124** (1005) 319.

[25] I. Honjo, Y. Endo and S. Goto, *J. Vac. Sci. Technol. B* **15** (1997) 2742.

[26] K. Uemura, S. Kanemaru and J. Itoh, *J. Micromech. Microeng.* **11** (2001) 81.

[27] P.R. Schwoebl and I. Brodie, *J. Vac. Sci. Technol. B* **13** (1995) 1391.

[28] Q. Wang, Z.L. Wang, J.J. Li, Y. Huang, Y.L. Li, C.Z. Gu and Z. Cui, *Appl. Phys. Lett*. **89** (2006) 063105.

[29] J. Liu, V.V. Wojak, C.G. Wojak, A.F. Myers, W.B. Choi, J.J. Hren, S.D. Wolter, M.T. McClure, B.R. Stoner and J.T. Glass, *Appl. Phys. Lett.* **65** (1994) 2842.

[30] I.W. Rangelow and St. Biehl, *J. Vac. Sci. Technol. B* **19** (2001)916.

[31] T. Sugino, S. Kawasaki, K. Tanioka and J. Shirafuji, *Appl. Phys. Lett*. **71** (1997) 2704.

[32] L. Chen and M.M. El-Gomati, *J. Vac. Sci. Technol. B* **17** (1999) 638.

[33] B. Günther, F. Kaldasch, G. Müller, S. Schmitt, T. Henning, R. Huber and M. Lacher, *J. Vac. Sci. Technol. B* **21** (2003) 427.

[34] J. Ishikawa, H. Tsuji, Y. Gotoh, T. Sasaki and T. Kaneko, *J. Vac. Sci. Technol. B* **11** (1993) 403.

[35] A. Dangwal, C.S. Pandey, G. Müller, S. Karim, T.W. Cornelius and C.Trautmann, *Appl. Phys. Lett.* **92** (2008) 063115.

[36] H. Chen, H. Zhang, L. Fu, Y. Chen, J.S. Williams, C. Yu and D. Yu, *Appl. Phys. Lett*. **92** (2008) 243105.

[37] R. Young, J. Ward and F. Scire, *Phys. Rev. Lett.* **27** (1971) 922.

[38] R. Young, J. Ward and F. Scire, *Rev. Sci. Inst.* **43** (1972) 999.

[39] A.D. Stefanis and A.A.G. Tomlinson, *Scanning Probe Microscopy: From Surface Structure to Nano-scale Engineering* (Trans tech publications ltd, Switzerland, 2001) Chapter 1.

[40] P.W. Atkins, *Physical Chemistry* (Oxford University Press, Oxford,1998) Chapter 12.

[41] P.A. Thiry, M. Liehr, J.J. Pireaux and R. Caudano, *Phys. Scr.* **35** (1987) 368.

[42] M. Rocca, *Surf. Sci. Rep.* **22** (1995) 1.

[43] M.P. Seah and W.A. Dench, *Surf. Interface Anal.* **1** (1979) 2.

[44] R.P.V. Duyne, *Science* **306** (2004) 985.

[45] W. Plummer, K.-D. Tsuei and B.-O. Kim, *Nucl. Instr. and Meth. in Phys. Res.* ***B*** 96 (1995) 448.

[46] P.A. Wolff, *Phys. Rev.* **95** (1954) 56.

[47] S.A. Komolov, *Total Current Spectroscopy of Surfaces* (Gordon and Breach Science Publishers, Philadelphia, 1992) Chapter 3.

[48] R.F. Wills and B. Feuerbacher, *Surf. Sci.* **53** (1975) 144.

[49] R.F. Wills and B. Fitton and G.S. Painter, *Phys. Rev. B* **9** (1974) 1926.

[50] L.S. Caputi, G. Chiarello, E. Colavita, A. Santaniello and L. Papagno, *Surf. Sci.* **152-153** (1985) 278.

[51] K. Oura, V.G. Lifshits, A.A. Saranin and A.V. Zotov, *Surface Science: An Introduction* (Springer, New York, 2003) Chapter 5.

[52] R.H. Fowler and L.W. Nordheim, *Proc. R. Soc. A* **119** (1928) 173.

[53] R. Gomer, *Field Emission and Field Ionization, Harvard Monographs in Applied Science* Vol. 9 (Harvard University Press, Cambridge, 1961) Chapter 2.

[54] A.-S. Lucier, H. Mortensen, Y. Sun and P. Grutter, *Phys. Rev. B* **72** (2005) 235420.

[55] C.J.D. Craigie, T. Sheehan, V.N. Johnson, S.L. Burkett, A.J. Moll and W.B. Knowlton, *J. Vac. Sci. Technol. B* **20** (2002) 2229.

[56] M. Nagao, *IEEJ Trans.* **1** (2006) 171.

[57] F. Festy, *Structural and Spectroscopic Studies of Surfaces on the Nanometer Scale.* PhD thesis, University of Birmingham (2000).

[58] L. Papagno, L.S. Caputi, M.D. Crescenzi, R. Rosei, *Phys. Rev. B* **26** (1982) 2320.

[59] S. Mizuno, *J. Vac. Sci. Technol. B* **19** (2001) 1874.

[60] S. Mizuno, J. Fukuda and H. Tochihara, *Surf. Sci.* **514** (2002) 291.

[61] S. Mizuno, J. Fukuda, M. Iwanaga and H. Tochihara, *Jpn. J. Appl. Phys.* **43** (2004) 5501.

[62] S. Mizuno, F. Rahman and M. Iwanaga, *Jpn. J. Appl. Phys.* **45** (2006) L178.

[63] Y. Miyatake, T. Nagamura, K. Hattori, Y. Kanemitsu and H. Daimon, *Jpn. J. Appl. Phys.* **42** (2003) 4848.

[64] Y. Miyatake, T. Nagamura, K. Hattori, Y. Kanemitsu and H. Daimon, *Jpn. J. Appl. Phys.* **41** (2002) 4943.

[65] M. Tomitori, H. Terai and T. Arai, *Appl. Surf. Sci.* **144** (1999) 123.

[66] M. Tomitori, M. Hirade, Y. Suganuma and T. Arai, *Surf. Sci*. **493** (2001) 49.

[67] M. Hirade, T. Arai and M. Tomitori, *Jpn. J. Appl. Phys.* **42** (2003) 4837.

[68] M. Hiade, T. Arai and M. Tomitori, *Jpn. J. Appl. Phys*. **45** (2006) 2278.

[69] X. Zhou, C. Xu, Z. Wei, W. Liu, J. Li, X. Chen, J.F. Williams and K. Xu, *J. Electron Spectrosc. Relat. Phenom.* **165** (2008) 15.

[70] G.F.A. van de Walle, H. Van Kempen, P. Wyder and P. Davidsson, *Appl. Phys. Lett*. **50** (1987) 22.

[71] S. Grafström, *J. Appl. Phys*. **91** (2002) 1717.

[72] D.A. Smith and R. W. Owens, *Appl. Phys. Lett*. **76** (2000) 3825.

[73] V. Gerstner, A. Thon and W. Pfeiffer, *J. Appl. Phys*. **87** (2000) 2574.

[74] A. Saito, J. Maruyama, K. Manabe, K. Kitamoto, K. Takahashi, K. Takami, M. Yabashi, Y. Tanaka, D. Miwa, M. Ishii, Y. Takagi, M. Akai-kasaya, S. Shin, T. Ishikawa, Y. Kuwahara and M. Aono, *J. Synchrotron Rad*. **13** (2006) 216.

[75] T. Eguchi, T. Okuda, T. Matsushima, A. Kataoka, A. Harasawa, K. Akiyama, T. Kinoshita and Y. Hasegawa, *Appl. Phys. Lett.* **89** (2006) 243119.

[76] K. Akiyama, T. Eguchi, T. An, Y. Hasegawa, T. Okuda, A. Harasawa and T. Kinoshita, *Rev. Sci. Instrum.* **76** (2005) 083711.

[77] P.K.Ghosh, *Introduction to Photoelectron Spectroscopy* (John Wiley & Sons, U.S.A. 1983) Chapter 1.

[78] R.G. Sharpe and R.E. Palmer, *Thin Solid Films* **288** (1996) 164.

[79] T. Ito and S. Okazakl, *Nature* **406** (2000) 1027.

[80] G.R. Brewer, *Electron-beam technology in microelectronic fabrication* (Academic Press, New York,1980) Chapter 2.

[81] C. Vieu, F. Carcenac, A. Pépin, Y. Chen, M. Mejias, A. Lebib, L. M-.Ferlazzo, L. Couraud and H. Launois, *Appl. Surf. Sci*. **164** (2000) 111.

[82] M. J. Madou, *Fundamentals of microfabrication, the science of miniaturization* (CRC Press, U.S., 2002), Chapter 2.

[83] F. Läermer and A. Schilp, German Patent No. DE-4241045C1 (23 June 1994), U.S. Patent No. 5,501,893 (21 March 1996).

[84] I.U. Abhulimen, S. Polamreddy, S. Burkett, L. Cai and L. Schaper, *J. Vac. Sci. Technol. B* **25** (2007) 1762.

[85] C.J.D. Craigie, T. Sheehan, V.N. Johnson, S.L. Burkett, A.J. Moll and W.B. Knowlton, *J. Vac. Sci. Technol. B* **20** (2002) 2229.

[86] I. Brodie and J. J. Muray, *The Physics of Microfabricaion* (Plenum Press, New York, 1982) Chapter 1.

[87] V. Agache, R. Ringot, P. Bigotte, V. Senez, B. Legrand, L. Buchaillot and D. Collard, *IEEE Trans. Nanotechnol.*, **4** (2005) 548.

[88] J. Robertson, *Rep. Prog. Phys.* **69** (2006) 327.

[89] A. Pulisciano, *Local Electron Energy Loss Spectra of Surfaces*, PhD thesis, The University of Birmingham 2007.

[90] E.M. Purcell, *Phys. Rev.* **54** (1938) 818.

[91] C.E. Kuyatt and J.A. Simpson, *Rev. Sci. Instrum.* **38** (1967) 103.

[92] R.B. Marcus, T.S. Ravi, T. Gmitter, K. Chin, D. Liu, W.J. Orvis, D.R. Ciario, C.E. Hunt and J. Trujillo, *Appl. Phys. Lett.* **56** (1990) 236.

[93] M. Kuwabara, D.R. Clarke and D.A. Smith, *Appl. Phys. Lett.* **56** (1990) 2396.

[94] J. Xhie, K. Sattler, M. Ge and N. Venkateswaran, *Phys. Rev. B* **47** (1993) 15835.

[95] W. Pong and C. Durkan, *J. Phys. D: Appl. Phys.* **38** (2005) R329.

[96] A.T. Bell, *Science* **299** (2003) 1688.

[97] C. Zhang, B. Yoon and U. Landman, *J. Am. Chem. Soc.* **129** (2007) 2228.

[98] C. Leung, C. Xirouchaki, N. Berovic and R.E. Palmer, *Adv. Mater.* **16** (2004) 223.

[99] R.E. Palmer, S. Pratontep and H.-G. Boyen, *Nat. Mater.* **2** (2003) 443.

[100] S.J. Carroll, *Deposition of Size-Selected Atomic Clusters on Surfaces*, PhD thesis, The University of Birmingham 1999.

[101] S.J. Carroll, S. Pratontep, M. Streun, R.E. Palmer, S. Hobday and R. Smith, *J. Chem. Phys*. **113** (2000) 7723.

[102] Courtesy of Dr. Hao

[103] H.-G. Boyen, G. Kästle, F. Weigl, B. Koslowski, C. Dietrich, P. Ziemann, J.P. Spatz, S. Riethműller, C. Hartmann, M. Möller, G. Schmid, M.G. Garnier and P. Oelhafen, *Science* **297** (2002) 1533.

[104] M. Nagao, D. Nicolaescu, T. Matsukawa, S. Kanemaru, J. Itoh, K. Koga, T. Kawase, K. Honda and T. Norikane, *J. Vac. Sci. Technol. B* **21** (2003) 1581.

[105] L. Chen and M.M. El-Gomati, *Ultramicroscopy* **79** (1999) 135.

[106] I. Ekvall, E. Wahlström, D. Claesson, H. Olin and E. Olsson, *Meas. Sci. Technol.* **10** (1999) 11.

[107] T.J.M. Zouros and E.P. Benis, *J. Electron Spectrosc. Relat. Phenom.* **125** (2002) 221.

[108] L. Papagno and L.S. Caputi, *Surf. Sci.* **125** (1983) 530.

[109] A.G. Marinopoulos, L. Reining, A. Rubio and V. Olevano, *Phys. Rev. B* **69** (2004) 245419.

[110] A. Hoffman, M. Elbaum and R. Brener, *Phys. Rev. B* **48** (1993) 16078.

[111] L.S. Caputi, G.Chiarello, A. Santaniello, E. Colavita and L. Papagno, *Phys. Rev. B* **34** (1986) 6080.

[112] U. Diebold, A. Preisinger, P. Schattshneider and P. Varga, *Surf. Sci.* **197** (1988) 430.

[113] B.J. Eves, *Scanning Probe Energy Loss Spectroscopy*, PhD thesis, The University of Birmingham 2002.

[114] E.J. Scheibner and L.N. Tharp, *Surf. Sci.* **8** (1967) 247.

[115] M. Dapor, L. Calliari and M. Filippi, *Nucl. Instrum. Methods Phys. Res. Sect. B-Beam Interact. Mater. Atoms* **255** (2007) 276.

[116] J.J. Lawton, A. Pulisciano and R.E. Palmer, *J. Phys.:Condens. Matter*, **21** (2009) 474206.

[117] R.F. Willis, B. Feuerbacher and B. Fitton, *Phys. Rev. B* **4** (1971) 2441.

[118] N.A.W. Holzwarth, S.G. Louie and S. Rabii, *Phys. Rev. B* **26** (1982) 5382.

[119] R.C. Tatar and S. Rabii, *Phys. Rev. B* **25** (1982) 4126.

[120] F. Maeda, T. Takahashi, H. Ohsawa, S. Suzuki and H. Suematsu, *Phys. Rev. B* **37** (1988) 4482.

[121] I. Schafer, M. Schluter and M. Skibowski, *Phys. Rev. B* **35** (1987) 7663.

[122] S. Fan, M.G. Chapline, N.R. Franklin, T.W. Tombler, A.M. Cassell and H. Dai, *Science* **283** (1999) 512.

[123] W. Zhu, G.P.Kochanski and S. Jin, *Science* **282** (1998) 1471.